Title

Tryptophan-aspartic acid-(WD)-repeat 72 (WDR72) as a regulator of endocytosis in the degradative pathway during the maturation stage of enamel formation

Author

Katsura, Kaitlin A

Publication Date

2019

Tryptophan-aspartic acid-(WD)-repeat 72 (WDR72) as a regulator of endocytosis in the degradative pathway during the maturation stage of enamel formation

by
Kaitlin A. Katsura

DISSERTATION
Submitted in partial satisfaction of the requirements for degree of
DOCTOR OF PHILOSOPHY

in

Oral and Craniofacial Sciences

in the

GRADUATE DIVISION
of the
UNIVERSITY OF CALIFORNIA, SAN FRANCISCO

Approved:

DocuSigned by:
Pamela Den Besten
0E9309D50C9D432...

Pamela Den Besten
Chair

DocuSigned by:
WU LI
DocuSigned by:
Andrew H. Jheon
F365EA7416024CA...

WU LI

Andrew H. Jheon

Committee Members

DEDICATION

To my husband, Matt, in gratitude for your unwavering encouragement and belief in me more than I do myself.

To my son, as a reminder to pursue your most ambitious goals.

To my mother and father, Jane and Neil, in gratitude for your unconditional love.

To my sister, Kelly Mika, in gratitude for the joy and laughter that you bring to my life.

To my grandparents, Chiye, Hatsue, John, Michio, and Wilfred, in recognition for your sacrifices to make education a priority.

To past and present researchers, in honor of your scientific contributions that helped me build upon your foundation.

To future researchers, to keep innovating, creating, and dreaming.

ACKNOWLEDGEMENTS

Thank you to past and present members of the Pamela Den Besten and Wu Li laboratories for your thoughtful insights, intellectual contributions, and efforts: Yukiko Nakano, DDS, PhD; Yan Zhang, MD, PhD; Li Zhu, MD, PhD; Thuan Le, DDS, PhD; Ling Zhan, DDS, PhD; Jonathan Stahl, DDS, PhD; Jeremy Horst, DDS, PhD; Dave Chandra, DDS, PhD; Dawud Abduweli, DDS, PhD; Michael Le, DDS, PhD; Ida Schaffer.

Thank you to Yoshiro Takano, DDS, PhD, for your beautiful science and your tutorials in HRP tracer experiments.

Thank you to members of the von Zastrow laboratory: Alison Leaf, PhD; Kate Varandas, PhD; Roshanak Irannejad, PhD for your vesicle uptake assay tutorials. Thank you also to members of the Marcucio laboratory.

Thank you to my qualifying exam and dissertation committee members Andrew Jheon, DDS, PhD; Wu Li, DDS, PhD; Diane Barber, PhD for your expertise, assistance in refining my research questions, and demanding the highest caliber of science of me.

Thank you to my committee chair, advisor, and scientific mentor, Pamela Den Besten, DDS, MS, for your support, advocacy, and demand of your students that they reach their highest potential.

Thank you to my clinical mentors, Thuan Le, DDS, PhD; and Sara Hahn, DDS; and my academic counselor, Caroline Shiboski, DDS, PhD, for your guidance, suggestions, and encouragement during my dual training.

Thank you to Ralph Marcucio, PhD; Pamela Den Besten, DDS, MS; Roger Mraz; and John Featherstone, PhD for your commitment to ensuring the existence of the integrated DDS/PhD program at UCSF.

Thank you to my Oral and Craniofacial Sciences (OCS) family, particularly: Shaun Abrams, PhD; Erin Ealba, DDS, PhD; Sean Ganther; Alice Goodwin, DDS, PhD; Andrew Jang, DDS, PhD; Alexis Lainoff, PhD; Jeremy Lin, DDS, PhD; Michael Le, DDS, PhD; Jon Stahl, DDS, PhD; Ida Shaffer, for your consults and commiserations, especially during the moments of uncertainty, adversity, conflict, and disappointment.

Thank you to my dental school clinic partners: Catherine Nguyen, DDS; Samuel Russom, DDS; Arya Saniee, DDS; and my Coaching Group: Whitney Bryant, DDS; Brianna Devito, DDS; Hamlet Khachatryan, DDS; Kayla Lebow, DDS; Raman Nazari, DDS; Kristy Potts, DDS; Jasmine Thomas, DDS; Jessica St. Martin Glauser, DDS; for your emotional support and encouragement during the completion of my dissertation work.

Without any of the aforementioned individuals, this work would not have been possible.

CONTRIBUTIONS

The text of Chapter 1 of this dissertation is a reprint of the manuscript as it appears in Matrix Biology. The co-authors listed in this publication directed and supervised the research.

Katsura, K., Horst, J., Chandra, D., Le, T., Nakano, Y., Zhang, Y., … DenBesten, P. K. (2014). WDR72 models of structure and function: A stage-specific regulator of enamel mineralization. Matrix Biology. https://doi.org/10.1016/j.matbio.2014.06.005

ABSTRACT

Tryptophan-aspartic acid-(WD)-repeat 72 (WDR72) as a regulator of endocytosis in the degradative pathway during the maturation stage of enamel formation

by

Kaitlin A. Katsura

Amelogenesis Imperfecta (AI) is a clinical diagnosis that encompasses a group of genetic mutations, each affecting processes involved in tooth enamel formation and thus, result in various enamel defects. The hypomaturation enamel phenotype has been described for mutations involved in the later stage of enamel formation, including *Klk4*, *Mmp20*, *C4orf26*, and *Wdr72*. Using a candidate gene approach, we discovered a novel *Wdr72* human mutation, resulting in a hypomaturation AI phenotype, to be a 5-base pair deletion (c.806_810delGGCAG; p.G255VfsX294). To gain insight into the function of WDR72, we used computer modeling of the full-length human WDR72 protein structure and found that the predicted N-terminal sequence forms two beta-propeller folds with an alpha-solenoid tail at the C-terminus. This domain iteration is characteristic of vesicle coat proteins, such as beta′-COP, suggesting a role for WDR72 in the formation of membrane deformation complexes to regulate intracellular trafficking. Our *Wdr72* knockout mouse model (*Wdr72*$^{-/-}$), containing a *LacZ* reporter knock-in, exhibited hypomineralized enamel similar to the AI phenotype observed in humans with *Wdr72* mutations. MicroCT scans of *Wdr72*$^{-/-}$ mandibles affirmed the hypomineralized enamel phenotype occurring at the onset of the maturation stage. H&E staining revealed that *Wdr72*$^{-/-}$ ameloblasts were shorter, and the enamel matrix was retained during maturation stage. H^+/Cl^- exchange transporter 5 (CLC5), an early endosome acidifier, was co-localized with WDR72 in maturation-stage ameloblasts and decreased in *Wdr72*$^{-/-}$ maturation-stage ameloblasts. Other markers along the endocytic degradative pathway were disrupted in *Wdr72*$^{-/-}$ mice, including clathrin, Dynamin II, and ANXA8. There were no obvious differences in RAB4A and LAMP1 immunostaining of *Wdr72*$^{-/-}$ mice as compared to wildtype and

heterozygous controls. Moreover, *Wdr72*$^{-/-}$ ameloblasts had reduced amelogenin immunoreactivity, suggesting defects in amelogenin fragment resorption from the matrix. *In vivo* and *in vitro* tracer studies with HRP and amelogenin showed delayed processing and loss of transport to lysosomes through the degradative pathway in *Wdr72*$^{-/-}$ ameloblast-like cell line generated using a CRISPR/Cas9 approach. These cells enabled live cell mechanistic studies targeting WDR72 function in vesicle acidification and microtubule recruitment, revealing a complex relationship with a major vesicle acidifying protein, vacuolar H+-ATPase (v-ATPase), and a link to microtubule recruitment. Ultrastructure of *Wdr72*$^{-/-}$ ameloblasts also showed faulty vesicle formation and ruffled border formation that coincided with pH and calcium matrix defects. These data demonstrate that WDR72 has a major role in enamel mineralization, most notably during the maturation stage, and suggest a function involving endocytic vesicle trafficking, possibly in the removal of amelogenin proteins by regulating microtubule assembly and membrane turnover in the degradative pathway.

TABLE OF CONTENTS

LIST OF FIGURES

LIST OF TABLES

INTRODUCTION

Enamel Formation

Teeth begin to develop *in utero*, initiated by a series of epithelial-mesenchymal interactions to undergo several stages of formation of the tooth bud and differentiation of the dental tissues. Odontoblasts are the mesenchymal cell type responsible for the formation of dentin, whereas the ameloblasts are the epithelial-derived cells that are responsible for the formation of the tooth enamel [1]. Tooth enamel is the hardest tissue in the body, and it is comprised of enamel rods made of carbonated hydroxyapatite that decussate to provide its strength and hardness [2].

The formation of enamel is a complex progression of ameloblast cells undergoing a series of differentiation stages, throughout which each ameloblast is responsible for the growth and development of a single enamel rod [1]. The first major stage of ameloblast differentiation is the secretory stage. During secretory stage, secretory ameloblasts elongate and form an apical process known as the Tomes' process. This cell stage is predominantly responsible for producing large quantities of enamel matrix proteins that will be secreted via the Tomes' process into the extracellular enamel space to form a scaffold for the future tooth enamel. Throughout the secretory stage, the extracellular matrix is laid down to form and determine the full thickness of the tooth enamel matrix and provides stability for the elongation of the long thin hydroxyapatite (HAP) crystals that span the width of the enamel matrix [3]. This stability is largely a result of the hydrophobic amelogenin proteins, comprising 90% of the organic volume in the secretory stage.

Once the final thickness of the tooth enamel has been produced, ameloblasts differentiate into maturation-stage ameloblasts [4]. During this change, ameloblasts undergo a dramatic shift in their morphological appearance, with a brief transition and the formation of ruffle-ended ameloblasts. The enamel matrix underlying the ruffle-ended ameloblasts (RA) is acidic (pH 5.8-

6.2) and is neutralized when the ameloblasts modulate to smooth-ended ameloblasts (SA) [5]. During the maturation stage, ameloblasts continue to modulate between ruffle- and smooth-ended cell types, resulting in hydrolysis and removal of the organic matrix, to allow the HAP crystals to grown in width to form the highly mineralized enamel matrix.

RA and SA ameloblasts are distinct in organellar organization and the presence of tight junctions. RA have tight junctions at the apical border, and an invaginated apical membrane, while SA have open cell junctions and smooth apical borders. This cellular modulation is essential for facilitating the cycling of $Ca2^{+}$, PO_4^{3-}, H_2O, and other small molecules through and between the cells, and removal of matrix proteins to allow crystal growth.

Amelogenesis imperfecta

Enamel formation is a highly regulated and complex process, and genetic mutations that alter the formation of the enamel matrix are referred to as amelogenesis imperfecta (AI). The genes that have been associated with AI include those encoding enamel matrix proteins, namely *Ambn* (MIM 601259) [6,7], *AmelX* (MIM 300391), *Amtn* (MIM 610912), *Enam* (MIM 606585), and associated matrix proteinases Klk4 (MIM 603767), and *Mmp20* (MIM 604629) [8,9]). Genes related to a full range of functions that are not specific to ameloblasts, including ion transport, vesicle transport, pH sensing, and cell-cell adhesions have also been identified: *Slc24a4* (MIM 609840) [10], *Fam83h* (MIM 611927) [11,12], *Itgb6* (MIM 14755) [13–15], and *Lamb3* (MIM 150310) [16–18]; as well as molecules of unknown function including *Fam20a* (MIM 611062) [19,20], *C4orf26* (MIM 614829) [21], *Wdr72* (MIM 613214) [22,23], and *Gpr68* (MIM 601404) [24].

And while AI was traditionally thought to be a non-syndromic disease affecting only tooth enamel, more recently, several genes have been linked to syndromes in addition to AI: *Tp63* (OMIM 604292) [25] with ectodermal dysplasia, *Slc13a5* with Kohlschütter-Tönz syndrome [26],

Lama3 (MIM 600805) with epidermolysis bullosa [27], and *Wdr72* [28,29] with bone development and distal renal tubular acidosis. A more complete list has been reviewed by Wright and co-workers [30].

WDR72 defects related to amelogenesis imperfecta

The human *Wdr72* gene has a total of 20 exons that contribute to several different transcript variants (ENST00000360509) [31] the longest and most common of which encodes a protein 1,102 amino acids in length (CCDS 10151.1). *Wdr72* was first found to be a candidate for autosomal recessive amelogenesis imperfecta (AI) in individuals affected with a pigmented and hypomaturation enamel phenotype (AI2A3; MIM 613211) through the use of a single nucleotide polymorphism (SNP) microarray [32]. Since this discovery, a total of ten *Wdr72* mutations have been reported as causal links to AI, including the 5-base pair deletion that we identified in exon 8 (c.806_810delGGCAG) (see **Fig. 1.1**). Previously reported mutations located farther downstream, spanning exons 10 through 17, are also predicted to disrupt the unique C-terminal domain (exons 15 to 20) by introducing premature stop codons that lead to truncated proteins [9,22,23,28,32]. While it is unclear whether any of these mutated *Wdr72* variants are indeed translated as defective proteins or degraded by nonsense-mediated decay, all mutations lead to similar hypomaturation enamel phenotypes.

My interest in AI, related to mutations of the *Wdr72* gene, arose when I identified a novel mutation of the WDR72 gene as the cause for a hypomaturation AI phenotype in a family seen in the UCSF pediatric dental clinic. I identified this mutation through a candidate gene approach to compare DNA sequences of affected individuals and their immediate family members (**Fig. 1.1A**) (**Table 1**). Chromatograms of affected, unaffected, and carrier individuals at exon 8 of the human *Wdr72* gene (NM_182758.2) revealed a 5-base pair deletion (c.806_810delGGCAG) that followed an autosomal recessive inheritance pattern of the AI phenotype (**Fig. 1G**). This

exon 8 deletion mutation resulted in a frameshift and premature stop codon (c.806_810delGGCAG; p.G255VfsX294). In addition, single nucleotide polymorphisms (SNPs) were also found to segregate with the deletion mutation, occurring in exon 14 as a silent mutation (c.1865G > A, p.613 V > V; rs74018741) and in the intron between exons 12 and 13 (g.53994305A > G; rs74018741) (Table 2). All other variations in sequenced candidate genes (*Amtn, Ambn, Enam, Mmp20, and Klk4*) of this family did not follow the disease inheritance (**Tables 1 & 2**).

This was the 7th reported mutation in *Wdr72* to be associated with an autosomal recessive pattern of inheritance to result in AI (**Fig. 1.1A**). Among the affected individuals, the 10.5-year-old proband (V3) illustrated the most severe phenotype, exhibiting yellow-brown staining and hypomature enamel in the permanent dentition (**Fig. 1.1B**). His panoramic radiograph revealed unerupted tooth enamel with an apparently normal thickness and an indistinguishable radiopacity to dentin, which is typically less radiopaque than enamel and indicates hypomineralization (**Fig. 1.1C**). Primary teeth of the affected identical twin sisters (V4 & V5) at 4-years-old displayed less severe phenotypes, although enamel was largely absent on the occlusal third of all primary teeth (**Fig. 1.1D**). Their radiographic images showed erosion of erupted primary molar enamel with similar radiopacities to dentin (**Fig. 1.1E & F**). All affected children were highly sensitive to thermal and chemical stimuli. These enamel phenotypes are similar to those described in previous reports of patients with mutated copies of the *Wdr72* gene [9,23,28,32], all of which predict early stop codons (**Fig. 1H**). In addition to a tooth enamel defect, the proband had congenitally missing 3 out of 4 six-year-old permanent molars (teeth #3, 19 and 30) and exhibited delayed eruption of his mandibular primary canines and molars, indicating a 1-year delay in dental development (**Fig. 1C**). Similar tooth development phenotypes have been reported in association with only one other *Wdr72* mutation, the second-most upstream

mutation occurring at exon 10 (**Fig. 1H**) [28], possibly linking early *Wdr72* mutations to additional tooth-related defects.

WDR72 is interesting because while its mutation results in a severe enamel phenotype, effects on other cells and tissues in the body range from relatively mild to a severe syndromic effect. One variant was reported to be associated with developmental problems in height, speech, respiration, and vision [28], while another is causal to distal renal tubular acidosis [29]. In addition, several *Wdr72* single nucleotide polymorphisms (SNPs) have been associated with kidney, heart, pancreatic, and neural diseases [33–38].

The hypomaturation enamel defect suggests that WDR72 function occurs during the maturation stage of enamel formation where enamel maturation and mineralization is completed. Indeed, a previous study showed WDR72 to be expressed in murine ameloblasts with an increased expression during maturation stage [22]; and our studies confirm this [39]. Of the ten mutations in the *Wdr72* gene that have been identified in humans affected with AI, all display hypomineralized enamel phenotypes in which the unerupted tooth enamel forms a matrix of normal thickness, but is radiolucent and abrades easily from the underlying dentin upon tooth eruption [9,22,23,28,32,39,40]. The known *Wdr72* mutations occur throughout the lengthy gene, possibly leading to alternative splice variants or non-sense mediated decay. Based on protein structure analysis, understanding where these mutations are occurring may possibly indicate the structural role of WDR72.

In the following chapters, my studies aim to identify the function of WDR72 as described. Chapter 1 begins with our published findings of the development and characterization of our *Wdr72*$^{-/-}$ mouse model. This mouse showed a clear role in the maturation stage and mineralization of tooth enamel and provided a hypomineralized tooth model similar to what is

observed in humans with *Wdr72*-associated AI. Chapter 2 then focuses on identifying WDR72's role in endocytosis, and Chapter 3 further delves into the mechanism by which WDR72 regulates the degradative pathway of endocytosis through the process of endosome maturation.

CHAPTER 1: WDR72 is a stage-specific regulator of enamel mineralization

RESULTS

To begin to understand how WDR72 alters enamel formation, I generated a *Wdr72* knockout (*Wdr72*$^{-/-}$) mouse model using the resources of the Knockout Mouse Project (KOMP). This functional *Wdr72* knockout mouse strain (*Wdr72*$^{-/-}$), along with littermate controls (*Wdr72*$^{+/+}$ and *Wdr72*$^{+/-}$), was made by breeding heterozygous mice (*Wdr72*$^{+/-}$) obtained from the KOMP Repository and the Mouse Biology Program at the University of California, Davis. In these mice, the *Wdr72* mutant allele (*Wdr72*$^{-}$) was generated using a 'knockout first conditional ready' approach using previously published methods [41] to splice in a *LacZ* gene reporter cassette prior to the critical *Wdr72* exon 3 (**Fig. 1.2A**). Exon 3 is present in all identified alternatively spliced *Wdr72* transcripts. PCR analysis confirmed that with this approach and verified a functional WDR72 knockout in the mice (**Fig. 1.2B & D**).

Mandibular molars and incisors of 6-week-old male *Wdr72*$^{+/+}$ and *Wdr72*$^{-/-}$ mice were evaluated for gross morphological differences (**Fig. 1.2C**) and exhibited an enamel phenotype similar to that observed in our affected AI patients (**Fig. 1.1B & D**). *Wdr72*$^{-/-}$ mice showed opaque and darkly stained enamel relative to the translucent appearing enamel observed in *Wdr72*$^{+/+}$ mice (**Fig. 1.2C**). *Wdr72*$^{-/-}$ enamel was of normal thickness at the base of incisors and molar crowns but was lost at occlusal surfaces, while the exposed dentin remained relatively intact. Heterozygous mice (*Wdr72*$^{+/-}$) appeared to have normal enamel akin to *Wdr72*$^{+/+}$ mice (data not shown), which mimics the autosomal recessive inheritance pattern seen in AI.

No other obvious tooth phenotypes or differences in major organs known to express *Wdr72* (ie. kidney and brain) were observed in *Wdr72*$^{-/-}$ mice (data not shown). Whole body weights of *Wdr72*$^{-/-}$ mice were significantly reduced ($P < 0.05$), beginning at postnatal day 21 (P21) in males and P24 in females compared to their *Wdr72*$^{+/+}$ controls (**Fig. 1.3**). Tooth eruption in mice

occurs between ages P10 and P14, while weaning age is P21, indicating that these body weight differences were due to difficulties with chewing hard foods rather than systemic effects caused by a loss of *Wdr72*.

Quantitative real-time PCR (qPCR) of micro-dissected secretory and maturation-stage ameloblasts showed significantly reduced *Wdr72* mRNA expression in *Wdr72*$^{-/-}$ secretory and maturation-stage ameloblasts to 4.4% and 1.7%, respectively, as compared to *Wdr72*$^{+/+}$ controls ($P < 0.05$). Such relatively low levels of *Wdr72* transcript observed in our mouse model is consistent with leaky expression levels observed for gene trapping methodologies and indicate successful *Wdr72* knockout (**Fig. 1.2D**) [42]. In addition, relative amounts of *Wdr72* transcript were significantly up-regulated from secretory to maturation stage in *Wdr72*$^{+/+}$ ameloblasts ($P < 0.05$), suggesting a major function during enamel maturation (**Fig. 1.2D**).

To confirm that WDR72 protein synthesis was altered, we made an antibody to the CETGTLERHETGERA peptide sequence of the WDR72 protein (amino acids 587–600 plus an extra cysteine residue). Verification of our WDR72 antibody, which was made against the same peptide sequence as the one previously synthesized [32], was performed on *Wdr72*$^{+/+}$ and *Wdr72*$^{-/-}$ kidneys by western blot (**Fig. 1.4**).

Immunostaining illustrated little to no WDR72 present in *Wdr72*$^{-/-}$ ameloblasts (**Fig. 1.5B, D, & F**). In *Wdr72*$^{+/+}$ mice, ameloblasts showed increased WDR72 immunoreactivity from secretory to maturation stage (**Fig. 1.5A, C, & E**). Using the continuously growing mouse incisor to visualize WDR72 expression on a time-scaled spectrum of ameloblast differentiation stages required for enamel formation, we further observed a specific increase at the onset of maturation stage and subcellular localization to distinct vesicle-like puncta at apical and basal regions of the cell (**Fig.**

1.5C & E), whereas, immunoreactivity in secretory ameloblasts appeared light and diffuse (**Fig. 1.5A**).

Wdr72$^{-/-}$ mice had enamel phenotypes consistent with functional defects at the maturation stage

Murine mandibles from 6-week-old male *Wdr72$^{+/+}$* (n = 3) and *Wdr72$^{-/-}$* mice (n = 3) were scanned by micro-computed tomography (microCT) and analyzed for differences in relative intensities of the major mineralized tissue types (enamel, dentin, and alveolar bone). The process of normal enamel mineralization was observed in the continuously growing mouse incisor of *Wdr72$^{+/+}$* mice, which showed an increasing enamel radiopacity that coincided with the transition zone of differentiating ameloblasts from secretory to maturation-stage morphologies (**Fig. 1.6A**, arrow). In contrast, radiopacity of enamel, beginning at the maturation stage of *Wdr72$^{-/-}$* molars and incisors, was significantly reduced compared to that of the *Wdr72$^{+/+}$*mice (**Fig. 1.6A & B**). These observations were quantified in cross-sections of the mandibular incisor, taken at secretory and maturation stages, and averaged for gray scale values within a selected region of interest (**Fig. 1.6C–F**). We found enamel radiopacities of *Wdr72$^{+/+}$* and *Wdr72$^{-/-}$* mice were not significantly different at secretory stage ($P = 0.92$) but were significantly reduced at maturation stage in *Wdr72$^{-/-}$* mice ($P < 0.05$) (**Fig. 1.6E**). Interestingly, *Wdr72$^{-/-}$* enamel from secretory to maturation stages showed significant differences ($P < 0.05$), suggesting that partial mineralization of the enamel matrix still occurred in the absence of *Wdr72*. *Wdr72$^{-/-}$* dentin ($P = 0.26$) and alveolar bone ($P = 0.22$) did not significantly differ in gray scale values compared to *Wdr72$^{+/+}$* controls (**Fig. 1.6E**).

Hematoxylin and eosin (H&E) stains of *Wdr72$^{+/+}$* and *Wdr72$^{-/-}$* mouse mandibles at P10 showed morphologically normal secretory ameloblasts in *Wdr72$^{-/-}$* mice and shortened maturation-stage ameloblasts, (**Fig. 1.7**). In addition, *Wdr72$^{-/-}$* mice exhibited retained non-mineralized, organic

material in the enamel matrix during maturation stage (Fig. 1.7, yellow arrows), whereas the lack of this proteinaceous staining in *Wdr72*$^{+/+}$ enamel matrices indicated a more mineralized enamel matrix (**Fig. 1.7A & B**).

Loss of Wdr72 resulted in decreased intracellular amelogenin proteins with no effect on transcript levels

We next investigated the possibility that *Wdr72* was needed for reuptake of amelogenin proteins from the matrix, since our *Wdr72*$^{-/-}$ mice showed retained proteinaceous material in the enamel matrix, and amelogenin is the predominant extracellular matrix protein secreted and hydrolyzed into fragments during enamel formation. Amelogenin immunoreactivity was slightly reduced in secretory stage ameloblasts at the Tomes' processes in *Wdr72*$^{-/-}$ mice (**Fig. 1.8B**) and was more obviously reduced at the apical border and the cytoplasm in *Wdr72*$^{-/-}$ ameloblasts at early maturation stage (**Fig. 1.8D**) as compared to ameloblasts from *Wdr72*$^{+/+}$ mice (**Fig. 1.8A & C**, respectively). By mid-maturation, intracellular amelogenin staining was absent in both *Wdr72*$^{+/+}$ and *Wdr72*$^{-/-}$ ameloblasts (**Fig. 1.8E & F**).

To verify that the decreased intracellular amelogenins in *Wdr72*$^{-/-}$ mice was not due to a decrease in amelogenin mRNA production, we quantified amelogenin transcripts from microdissected enamel epithelia at secretory and maturation stages. Analyses by qPCR showed no significant differences between *Wdr72*$^{+/+}$ and *Wdr72*$^{-/-}$ ameloblasts at either stage (n = 3; $P = 0.81$ secretory, $P = 0.53$ maturation) (**Fig. 1.8G**).

Wdr72$^{-/-}$ *mice showed reduced immunostaining of the endosome protein CLC5 during the maturation stage compared to other vesicle markers*

Consecutive sections of *Wdr72*$^{+/+}$ maturation-stage ameloblasts showed WDR72 and CLC5 immunolocalization to the same supernuclear (basal) areas, as well as to apical regions slightly distal to the enamel matrix border (arrowheads, **Fig. 1.9G & H**). In addition, CLC5 was less immunoreactive in *Wdr72*$^{-/-}$ maturation-stage ameloblasts, as compared to *Wdr72*$^{+/+}$ mice (**Fig. 1.9B, D, & F**). Unlike CLC5, immunostaining for RAB4A (a marker for endosome sorting and recycling) and LAMP1 (a marker for lysosomes) did not show obvious differences between *Wdr72*$^{+/+}$ and *Wdr72*$^{-/-}$ maturation-stage ameloblasts (**Fig. 1.9I–L**).

WDR72 structure modeling predicted a configuration unique to proteins found in membrane-deformation complexes with homology to the crystallized β'-COP structure

These characterizations of the *Wdr72* knockout mouse model, including reduced CLC5 and retained enamel matrix, suggest the possibility of an endosome related phenotype, possibly resulting in an endocytosis defect. To gain further insights into the function of *Wdr72* in enamel formation, I used a molecular modeling approach, described in this section.

The human full-length WDR72 protein is 1102 amino acids in length and predicts two clusters of WD40 repeat domains at the N-terminus and a unique C-terminus with no identifiable homology domains (**Fig.1.10A**; ENSG00000166415). To provide further insight into WDR72 function, we generated all-atom models of the human full-length WDR72 protein (**Fig.1.10A**) and mutated variants (**Fig. 1.11**). These models were generated using sequence similarity to annotated proteins using two comparative protein structure prediction pipelines: (1) I-TASSER [43,44] and (2) HHsearch ported into MODELLER [43,45]. Among all known protein structures in the Protein Data Bank (PDB), both modeling pipelines showed full-length WDR72 with greatest structural homology to the known crystal structure of *Saccharomyces cerevisiae* β′-COP (Fig.1.10B), an essential subunit in eukaryotic COPI vesicle coat assemblies (PDB identifier: 3mkq) and was thus was used as the primary template for constructing the WDR72 models. All statistically

reliable models of full-length WDR72 (zDOPE < − 1) showed a series of β-sheets folded into two β-propellers, followed by a succession of parallel α-helices twisting into a compact tail, referred to as an α-solenoid (**Fig.1.10C**). This structural iteration of 1 or 2 β-propellers followed by an α-solenoid is unique to membrane-deformation complexes [46,47], which include vesicle coatomers (i.e. clathrin, COPII, COPI) and the nuclear pore complex (i.e. Nup).

To evaluate the number of blades present in each β-propeller, we applied the hidden Markov random field algorithm SMURF [48], built specifically to detect combinations of 6-, 7-, and 8-bladed double β-propellers. We found that full-length WDR72 was most likely composed of two 7-bladed β-propellers ($P < 0.0001$) rather than any other combinations of one or two 6-, 7- or 8-bladed β-propellers ($P > 0.05$), which is consistent with other membrane-deformation complex proteins. The 1st β-propeller blades were predicted as the following residues: 22–59, 67–104, 119–150, 168–198, 215–251, 260–292, and 301–353; and for the 2nd β-propeller: 359–400, 407–442, 466–494, 521–554, 562–627, 633–659, and 665–686; with α-helices thereafter (**Fig. 1.2C**). Therefore, the constructed model of WDR72 showed two β-propeller domains and a curved α-solenoid tail.

We observed that both exon 8 and exon 10 mutations occurred between two predicted WD40-repeat domain clusters (**Fig. 1.10A**; ENSG00000166415). Multiple splice variants have been identified for the human *Wdr72* gene, whose encoding is regulated by several different 5′UTRs and 3′UTRs (AceView) [31]. This may suggest evasion of RNA decay in *Wdr72* mutations observed in individuals with AI. Under this possibility, we modeled all putative WDR72 truncations resulting from AI-related mutations and found that these two most up-stream mutations formed a single β-propeller containing only 6 blades ($P < 0.01$), rather than 7, which suggests instability of the protein fold (**Fig. 1.11**).

DISCUSSION

Previously, publications hypothesized that the function of WDR72 was vesicle-related, based on the known vesicle trafficking functions of WDR72's closest human homologue, WDR7 (El-Sayed et al., 2009; Lee et al., 2010). To further define the function of WDR72, we generated a knockout mouse (*Wdr72*$^{-/-}$), which exhibited a hypomaturation enamel phenotype similar to that observed in humans with *Wdr72*-associated AI [9,22,28]. Quantitative RT-PCR (qPCR) of *Wdr72*$^{-/-}$ secretory and maturation-stage ameloblasts showed low mRNA *Wdr72* transcript levels in both tissue groups relative to the observed up-regulation from secretory to maturation stage in *Wdr72*$^{+/+}$ control mice. Similarly, anti-WDR72 immunostaining of *Wdr72*$^{-/-}$ ameloblasts exhibited non-specific background staining at all stages of enamel formation, whereas *Wdr72*$^{+/+}$ controls were intensely immunoreactive shortly after entering the maturation stage. Western blots of *Wdr72*$^{+/+}$ and *Wdr72*$^{-}$/$^{-}$ kidney samples paralleled these findings with low WDR72 protein levels in *Wdr72*$^{-/-}$ mice.

Whole body weights of both female and male *Wdr72*$^{-/-}$ mice were decreased compared to *Wdr72*$^{+/+}$ mice, however, this was observed only after weaning age (P21), suggesting that this difference was due to the tooth-related defect as opposed to other systemic effects. Overall, the *Wdr72*$^{-/-}$ mice paralleled the descriptions of individuals with *Wdr72*-related AI. Taken together, these initial characterization studies illustrate that *Wdr72* is functionally knocked out in our *Wdr72*$^{-/-}$ mouse model, providing an excellent system for studying *Wdr72*-associated AI to elucidate its role in tooth development.

Similar to the radiolucent enamel phenotypes described for human *Wdr72* mutations, our microCT imaging of *Wdr72*$^{-/-}$ mandibles showed stage-specific and tissue-specific hypomineralized defects in the tooth enamel. At secretory stage, relative intensities

of *Wdr72*$^{-/-}$ enamel radiopacities were comparable to those of *Wdr72*$^{+/+}$ controls but did not increase in radiopacity to the same extent as *Wdr72*$^{+/+}$ enamel once the maturation stage began. *Wdr72* loss also appeared to have tissue-specific effects, showing dentin and alveolar bone to be unchanged in *Wdr72*$^{-/-}$ mice.

Additional evidence in support of the stage-specificity of WDR72 during enamel maturation were our findings that *Wdr72*$^{-/-}$ ameloblasts appeared shorter in height only after differentiating into the maturation-stage cell type, and the *Wdr72*$^{-/-}$ enamel matrix differed only during the maturation stage, showing retained organic matter. These comparisons were made along the continuously growing mouse incisor, which presents the entire spectrum of enamel formation [49], thus providing time-scale insight into WDR72 function. The observed cell and matrix phenotypes further support a stage-specific role for WDR72 in regulating enamel mineralization and suggests a function in one of the major cell processes in maturation-stage ameloblasts.

A major function of maturation-stage ameloblasts that is often disrupted in AI hypomaturation phenotypes is the processing of amelogenin proteins, which constitute the majority of the organic extracellular matrix [50–52]. Our observation that organic material was retained in *Wdr72*$^{-/-}$ enamel matrices during maturation suggests that WDR72 has a role in either the secretion of proteases into the mineralizing matrix or in removal of hydrolyzed protein fragments from the matrix to allow final matrix mineralization to occur. Amelogenins are secreted during early matrix formation and are subsequently hydrolyzed and removed from the enamel matrix during the maturation stage to allow thickening of the hydroxyapatite crystals that comprise the tooth enamel [8,53,54]. Removal of hydrolyzed matrix proteins, including amelogenins, may be due to either a passive diffusion between the open junctions of smooth-ended ameloblasts or an active transport mechanism through the cells [55]. As amelogenins are removed, Ca^{2+} is

transported through ameloblasts and deposited along with phosphate to form the mineralized enamel matrix [56].

We found that *Wdr72*$^{-/-}$ maturation-stage ameloblasts had less intracellular amelogenin protein with no change in the relative synthesis as compared to *Wdr72*$^{+/+}$ controls, suggesting that WDR72 influences the active uptake of amelogenin fragments into the cell, presumably by regulating endocytosis. Interestingly, we also observed decreased amelogenin immunoreactivity at the Tomes' processes in *Wdr72*$^{-/-}$ secretory ameloblasts with no effect on transcript levels. This was surprising, given that *Wdr72* loss had so far manifested as a maturation stage phenotype; however, it is still consistent with the fact that *Wdr72*$^{+/+}$ secretory ameloblasts express WDR72, albeit at low levels [22]. Tomes' processes, though largely functioning in the exocytosis of amelogenins, also have endosomes that contain hydrolyzed amelogenins [53,57,58]. It is also possible that WDR72 has more subtle roles at earlier stages of tooth development that involve intracellular amelogenin transport, which is supported by the tooth agenesis and delayed eruption observed in some AI individuals.

To further investigate a possible vesicle trafficking function of WDR72, we immunostained *Wdr72*$^{+/+}$ and *Wdr72*$^{-/-}$ maturation-stage ameloblasts with anti-CLC5 as a marker of early endosomes, anti-RAB4A as a marker of early and recycling endosomes, and anti-LAMP1 as a marker of lysosomes. Our immunostainings of WDR72 and CLC5 on consecutive sections of *Wdr72*$^{+/+}$ maturation-stage ameloblasts are consistent with the possibility that WDR72 localizes to endosomes. This is further supported by similar immunolocalizations observed for RAB4A and the endocytic coat protein, AP2 [59], but not the more basal immunolocalization of LAMP1 to lysosomes.

In *Wdr72*$^{-/-}$ maturation-stage ameloblasts, CLC5 showed decreased immunoreactivity relative to *Wdr72*$^{+/+}$ controls, while RAB4A and LAMP1 appeared to be unaffected. CLC5 and RAB4A are both early endosome markers and are frequently associated with one another [60], although RAB4A also specifically functions in recycling endosomes. This suggests a unique function for WDR72 in mediating a specific subpopulation of endosomes, possibly related to other known functions of CLC5, such as exocytosis of ion channel antiporters [61], Ca^{2+} transport [62], or pH regulation [32,63,64] that are integral to major processes carried out by maturation-stage ameloblasts. While it is also possible that CLC5 decreases observed in *Wdr72*$^{-/-}$ ameloblasts were attributed to secondary effects on the cell, these decreases coincided with the timing of normal WDR72 expression.

Following the initial uptake into cells, endocytic vesicles are transported to lysosomes, which are often characterized by LAMP1 labeling. LAMP1 has been associated with amelogenin uptake into ameloblasts, and extracellular increases in amelogenin *in vitro* has been shown to upregulate LAMP1 [65,66]. Therefore, we would expect that if amelogenin uptake into the cell was decreased, LAMP1 immunostaining would also be relatively decreased in *Wdr72*$^{-/-}$ mice. The lack of any change in LAMP1 may suggest that WDR72 does not mediate amelogenin uptake into the cell, but rather is involved in degradation of amelogenins in the extracellular matrix, possibly through the secretion of enamel matrix proteinases. Reduced proteinase secretion at the maturation stage could inhibit the uptake of amelogenin protein fragments into the cell. Further analysis of matrix proteinases in *Wdr72*$^{-/-}$ as compared to *Wdr72*$^{+/+}$ will further clarify the possible roles of WDR72 in amelogenin degradation and endocytosis.

To evaluate the potential functions of WDR72, we used bioinformatics to model a predicted protein structure of WDR72 by mapping the full-length human amino acid sequence onto all known structures within the Protein Data Bank (PDB). Our WDR72 structure model predicted a

membrane-coating architecture composed of two 7-bladed β-propeller heads, followed by an α-solenoid fold, which are respectively encoded by two N-terminal WD40-repeat domain clusters and a unique C-terminus (residues #687–1102). This particular domain combination (1 or 2 β-propellers, then α-solenoid) is a highly conserved architecture among proteins that form membrane coat complexes, dating back to the early eukaryotic endomembrane system [47,67]. In addition, this group of membrane-coating complexed proteins has remained somewhat exclusive to (a) the scaffold-layer proteins of the nuclear pore complex (Nups) that stabilize the inner and outer nuclear envelope membranes at the nuclear pore edges and (b) the vesicle coatomers (COPI, COPII, and clathrin) that assemble in cage-like lattices to initiate the budding step of vesicle formation [67]. Structure domains of these membrane-coating proteins typically utilize their WD40 β-propeller folds to serve as docking sites for multiple protein–protein interactions [68–70] and their α-solenoids, formed from anti-parallel stacked α-helices, to stabilize and induce membrane curvature [47,67]. Modeling WDR72 as a structure containing these domains, specifically in the β–β–α order, suggests it as a member of this membrane-coating group.

We found that when WDR72 was compared to all solved protein structures, the highest *structural* homology was to β′-COP (PDB identifier: 3mkq), an essential subunit in the COPI vesicle coatomer complex. This homology further suggests that WDR72 functions as a vesicle coat protein, and together these bioinformatic analyses are consistent with the previously proposed role for WDR72 in vesicle trafficking [22,23]. This previously proposed function for WDR72 was based on the high *sequence* homology to WDR7, a known regulator of Rab3A GTPase in Ca^{2+}-dependent exocytosis at neural synapses [71,72]. Interestingly, WDR7 (under the alias “Rabconnectin-3β”) has another function in regulating vesicles, rather, in the endocytic pathway by directly monitoring vacuolar H^+-ATPase (v-ATPase) activity in *Drosophila* [73,74], suggesting the possibility that WDR72 may too function in both exocytosis and endocytosis.

Further evidence pointing to an endocytic vesicle coat function for WDR72 are the *in vivo* immunolocalization of AP2 (cargo-specifying adaptor component of clathrin coatomers) found by Lacruz and co-workers [59]. Together, these findings support a role for WDR72 in mediating vesicle formation, potentially as an endocytic and/or exocytic coat protein to help regulate transport between cell and matrix.

It is also worth noting that WDR72 and WDR7 diverge at residue #845 (exon 15) [23], and the remaining 60% of WDR72's C-terminus is unique. The C-terminus is predicted to form the α-solenoid region, and α-solenoids of canonical vesicle coatomers are structurally conserved but exhibit little similarity to one another at the sequence level [47]. These differences are thought to contribute to the diversity of lattice size and shape, which invariably dictate cargo specificities and vesicle type, suggesting that the unique C-terminal sequence of WDR72 specifies its function to enamel formation and its vesicle cargo. The importance of this α-solenoid is emphasized by our modeling of all putative WDR72 proteins containing mutations relevant to hypomaturation enamel AI phenotypes, all of which showed a shortened or absent α-solenoid tail (**Fig. 1.11**).

Both WDR72 and WDR7 are members of the WD40-repeat domain super family. Proteins in the WD40-repeat domain superfamily are defined by 4–8 repeating units of approximately 44–60 amino acids ending in tryptophan (W) and aspartic acid (D). WD40 proteins typically contain several repeat domains that encode a series of anti-parallel β-sheet blades that configure into a well-stabilized, non-catalytic propeller, called a “β-propeller”, for multi-unit complex docking [68,70]. Proteins containing these β-propellers are observed in a broad range of cell processes, including signal transduction, cell cycle regulation, and vesicular trafficking; as such, they often contain other domain types that dictate specificities of function and pathway [69]. Our molecular modeling of WDR72 predicted a vesicle coat function, based on its conserved iteration of sub-

structural domains and structural homology to β′-COP, a known protein structure that is a necessary component of the COPI vesicle coatomer.

In summary, these studies have reported the use of structural modeling to support a function of WDR72 in vesicle trafficking. The generation and initial analyses of the *Wdr72*$^{-/-}$ mouse confirmed the importance of WDR72 in enamel formation and illustrated a direct link between mutated WDR72 to hypomineralized enamel. We found reduced intracellular amelogenin in the *Wdr72*$^{-/-}$ ameloblasts with a similar reduction in the endosome marker protein ClC5, suggesting a role for WDR72 in the removal of amelogenins during enamel maturation. Further understanding of WDR72's function in amelogenesis will allow us to better understand this unique biomineralization process and how other tissues potentially regulate mineralization. These studies are also important in determining other yet unknown risk factors for AI patients affected with mutated *Wdr72*.

In the next chapter, we investigate how WDR72 can facilitate amelogenin removal by regulating vesicle transport.

CHAPTER 2: WDR72 is required for endocytosis

Our studies of the *Wdr72* knockout mouse model indicate a role for *Wdr72* in removal of proteins from the extracellular enamel matrix. In addition, our molecular modeling suggests a role in vesicle formation. During enamel formation, both exocytic and endocytic functions in vesicle transport are possible roles for WDR72, however, little is known about how ameloblasts regulate these transport pathways to drive enamel mineralization. Therefore, a majority of our clues for WDR72 function rely on its evolutionary homology to other known vesicle regulators. As previously mentioned, WDR72's closest human homolog is WDR7, a known regulator of Rab3A GTPase in Ca^{2+}-dependent exocytosis at neural synapses [71,72] and a direct interactor of vacuolar H^+-ATPase (v-ATPase) activity in the endocytic pathway [73,74], indicating that WDR72 may too function in both exocytosis and endocytosis. In addition, our protein structural modeling of WDR72 to β′-COP further supports WDR72's role in vesicle transport, but specifically points to a structural role in vesicle formation.

Additional clues pointing to the involvement of WDR72 in both exocytosis and endocytosis during enamel maturation have been primarily speculation up to this point. KLK4 is the dominant secreted protease during the maturation stage to hydrolyze extracellular matrix proteins, and *Klk4*$^{-/-}$ mice have shown similar hypomaturation defects to those observed in our *Wdr72*$^{-/-}$ mice [75–77]. During the maturation stage, two major functions of ameloblasts are endocytosis and ion transport, and a link between the endosome acidifying protein, H^+/Cl^- exchange transporter 5 (CLC5) and WDR72 have been established [39], suggesting that WDR72 may mediate a specific subpopulation of endosomes.

Together, our studies of the *Wdr72*$^{-/-}$ mouse model indicated a role for WDR72 in removal of proteins from the extracellular enamel matrix, and our molecular modeling of the WDR72 protein suggests a role of WDR72 in vesicle transport. Therefore, in this chapter, we focus on

identifying WDR72's function in protein removal by looking into its role in vesicle transport via exocytosis and endocytosis.

RESULTS

KLK4 protease activity in the enamel matrix and mRNA expression are unchanged in Wdr72$^{-/-}$ mice

To test whether WDR72 was involved in exocytosis of maturation-stage, we investigated the activity of KLK4, a known proteolytic enzyme that is produced and secreted during the maturation stage. KLK4 is secreted into the enamel matrix during the maturation stage in order to hydrolyze enamel matrix proteins, which are then removed by ameloblasts to allow final matrix mineralization [50,75,76]. Inhibition of KLK4 synthesis or activity results in the retention of enamel matrix proteins, making altered KLK4 exocytosis a candidate pathway to result in the retention of amelogenins in the *Wdr72*$^{-/-}$ mouse enamel matrix. To investigate the possibility that increased matrix proteins in the WDR72 matrix are due to altered KLK4 activity, we measured both KLK4 expression in maturation-stage ameloblasts and the hydrolytic activity in the enamel matrix of *Wdr72*$^{+/+}$, *Wdr72*$^{+/-}$, and *Wdr72*$^{-/-}$ mice.

We found no significant differences in either incisors or molars of protease activity among *Wdr72*$^{+/+}$, *Wdr72*$^{+/-}$, and *Wdr72*$^{-/-}$ mouse enamel (**Fig. 2.1**). These studies were done by adding a quencher peptide with a specific KLK4 cleavage site was added to isolated enamel matrices of whole mandibular incisors or first molars. Between 90 and 120 minutes, KLK4 activity in *Wdr72*$^{+/+}$, *Wdr72*$^{+/-}$, and *Wdr72*$^{-/-}$ mice showed complete hydrolysis of available quenched peptide, which was similar to previous studies showing maximum hydrolysis after 2 hours [78].

To confirm that our protease findings were not affected by alterations in *Klk4* transcript levels, we used qPCR to measure *Klk4* mRNA levels in maturation-stage ameloblasts. We found no significant differences among *Wdr72*$^{+/+}$, *Wdr72*$^{+/-}$, and *Wdr72*$^{-/-}$ mouse ameloblasts.

Finally, to determine whether loss of KLK4 would alter synthesis of WDR72, we immunostained *Klk4*$^{-/-}$ mouse incisors for WDR72 and found no differences in immunostaining of the *Klk4*$^{-/-}$ as compared to *Klk4*$^{+/+}$ mice. (**Fig. 2.2**). This finding suggests that KLK4 does not affect WDR72 expression or localization. When considered with our results from **Fig. 2.1,** these data indicate that matrix retention observed in *Wdr72*$^{-/-}$ mice is likely unrelated to KLK4 and that WDR72 and KLK4 hold truly independent functions of one another in enamel formation.

WDR72 is a regulator of the endocytic pathway during the maturation-stage of enamel formation

We next examined whether the *Wdr72*$^{-/-}$ enamel phenotype was due to defects in the endocytic pathway. Although little is known regarding endocytosis in maturation-stage ameloblasts, the presence of a diversity of endocytic vesicles have been identified [1,79–81]. Additionally, it has been shown that an exogenous tracer molecule, horseradish peroxidase (HRP), can be endocytosed by maturation-stage ameloblasts [58,82,83].

HRP is a well-studied marker of fluid-phase endocytosis, and it has been found to mix with organic matrix during the endocytic process in a nonselective manner [58]. HRP readily passes through open cell junctions (presumably of smooth-ended ameloblasts) to reach the enamel matrix surface, where it is then constitutively endocytosed and digested by cells through the degradative pathway in the endolysosomal system [58,82,83]. One study suggested that amelogenins are likely to be reabsorbed by this fluid-phase endocytosis or micropinocytosis, a process of “cell drinking”, or sampling, of the external environment [58]. To determine whether

WDR72 modulates endocytosis of matrix proteins by ameloblasts, we injected HRP into *Wdr72*$^{-/-}$, *Wdr72*$^{+/-}$, and *Wdr72*$^{+/+}$ mice and recorded its uptake into the ameloblasts.

Fluorescein labeled HRP was injected into *Wdr72*$^{+/+}$, *Wdr72*$^{+/-}$, and *Wdr72*$^{-/-}$ mice at 15, 30, and 60 minute intervals. Following HRP injections, dissected mandibular and maxillary incisors were cryosectioned and immunostained for lysosomal-associated membrane protein 1 (LAMP1), a common marker of lysosomes. Sections were then visualized under confocal microscopy. For a more detailed description of the methods, please see Methods Section.

Similar to previous studies that tracked HRP in rats and hamster ameloblasts [83], our control mice showed classic HRP uptake patterns. At the onset of maturation stage, HRP that had reached the enamel matrix was taken up at the apical border of ameloblasts after 15 minutes but had not quite reached LAMP1-positive vesicles (**Fig. 2.3A-D**). At 30 minutes post-injection, control mice showed some HRP co-localizing with LAMP1 and much of the apical HRP was absent (**Fig. 2.3I-L**). By 60 minutes, HRP was mostly absent in *Wdr72*$^{+/+}$ and *Wdr72*$^{+/-}$ ameloblasts (**Fig. 2.3Q-T**). This progression of HRP through the ameloblasts was distinctly different in *Wdr72*$^{-/-}$ mice. Initially, *Wdr72*$^{-/-}$ mice showed similar intracellular HRP uptake patterns as the controls (**Fig. 2.3E-H**). However, at the 30-minute time point, HRP remained largely localized to the apical border (**Fig. 2.3M-P**). Even after 60 minutes, *Wdr72*$^{-/-}$ ameloblasts showed high levels of HRP at the apical border, while only some HRP localized to LAMP1 positive vesicles (**Fig. 2.3U-X**).

WDR72 affects markers within the endocytic system that are involved in vesicle formation along the degradative pathway

Several endocytic vesicles exist in maturation-stage ameloblasts, and, as in all cells, this diversity of endosomes interact within a complex web of pathways. Since our *Wdr72*$^{-/-}$ mice

showed a delay in intracellular processing of HRP, we immunostained targeted proteins known to participate at different stages along the degradative pathway of endocytosis. The following spatial and temporal analyses illustrate WDR72 as a regulator of endocytosis, supporting a role in the degradative pathway.

To assess the first stage in the endocytic pathway, we immunostained *Wdr72*$^{+/+}$ and *Wdr72*$^{-/-}$ mice for clathrin, as it is one of the first players involved in the initial uptake of exogenous material, and clathrin has structural homology with WDR72 as another β-propeller/α-solenoid protein (see Chapter 1) [39]. Immunolocalization of clathrin heavy chain in *Wdr72*$^{+/+}$, *Wdr72*$^{+/-}$, and *Wdr72*$^{-/-}$ mice showed positive reactions in control mice that appeared to coincide with the typical cycling pattern of maturation-stage ameloblasts (SA0/RA0, RA1, SA1, RA2, etc.) (**Fig. 2.3A**). After transition stage, control mice showed clathrin in punctate aggregates at the apical border (RA1), then briefly became diffused (SA1), and then returned to the aggregates in the apical region of the cells (RA2) (**Fig. 2.3**). In *Wdr72*$^{-/-}$ mice, similar aggregate staining appeared along the apical border (RA1), however, once becoming diffuse, clathrin aggregates remained diffuse and did not appear to cycle back along the apical border.

Loss of Wdr72 increases Dynamin II, a vesicle scission protein

The disruption of clathrin immunolocalization observed in *Wdr72*$^{-/-}$ mice occurred after WDR72's initial expression at the beginning of maturation stage (**Fig. 1.5B**), suggesting the possibility that WDR72 regulates clathrin coated vesicles. However, clathrin is present in multiple endocytic vesicles within the cell, such as the early endosome, secretory granules, and the trans-Golgi network [84], and it is therefore possible that WDR72 may affect only certain clathrin-coated vesicles. We therefore investigated whether the effect observed in clathrin was linked specifically to clathrin-mediated endocytosis by looking at a specific marker to clathrin at the plasma membrane.

Dynamin II is well-known to interactor with clathrin to regulate vesicle scission, most notably at the plasma membrane. Interestingly, when we immunolocalized dynamin in *Wdr72*$^{-/-}$ mice, we saw a stark increase in reactivity (**Fig. 2.4**). In control mice, immunoreactivity of dynamin II showed apical staining after transition stage, then became very lightly diffuse, almost absent even, and then returned to apical staining (**Fig. 2.4**), coinciding with the ruffle border cycles. In *Wdr72*$^{-/-}$ mice, however, staining along the apical border initially occurred but became diffusely stained with retained immunoreactivity throughout the remainder of the maturation stage. An increase in dynamin suggests an increase in vesicle scission at the apical border, indicating that perhaps WDR72 is an important inhibitor to regulate the timing of vesicle formation to ensure proper transport of cargo.

WDR72 affects localization of annexin A8 (ANXA8), a known regulator of late endosomes / multivesicular bodies

After endocytosis is initiated by uptake into early endosomes (EE), cargo is either routed to (1) recycling endosomes back to the plasma membrane or (2) to late endosomes (LE), also known as multivesicular bodies (MVB) to fuse with lysosomes. Our previously published work showed no difference in the recycling endosome marker, RAB4A [39], whereas our HRP tracer studies showed delayed processing to the lysosomes (see above, **Fig. 2.3**). Therefore, we wanted to test whether proteins involved in the stages between the EE and the lysosome would also be affected.

In the degradative pathway of endocytosis, LE/MVBs are intermediate vesicles between the EE and the lysosome. LE/MVBs are characterized by their low pH compared to other endosomes, since they progress and mature along the degradative pathway by forming intralumenal vesicles (ILVs), acidifying their lumens, and incorporating lysosomal hydrolases to digest material. Once

matured, these LE/MVBs fuse with lysosomes to become an endolysosome hybrid, which is the last step prior to merging with lysosomes.

In a microarray of secretory and maturation-stage ameloblasts, we found annexin-A8 (ANXA8) to have a 2.9 fold increased expression in maturation-stage ameloblasts as compared to secretory ameloblasts [85]. ANXA8 has a role in LE/MVB formation [86], possibly by organizing the membrane and cytoskeleton thought to be through interactions with direct binding to $PtdIns_{(4,5)}P_2$ and recruitment of F-actin [87,88].

When immunostaining ameloblasts for ANXA8, *Wdr72*$^{+/+}$ early maturation-stage ameloblasts showed little to no staining, which then became apparent much later in maturation. However, whereas *Wdr72*$^{-/-}$ mice showed an immediate increase in ANXA8 immunostaining shortly after the onset of maturation stage (**Fig. 2.7**). Together with our previous HRP data showing delayed transport to the lysosomes in *Wdr72*$^{-/-}$ mice (**Fig. 2.3**), these data may suggest an accumulation of LE/MVBs in *Wdr72*$^{-/-}$ maturation-stage ameloblasts that result in a similar delay in fusion to the lysosome.

An additional surprising observation was that ANXA8 localized to the nuclei of *Wdr72*$^{-/-}$ ameloblasts, whereas control mice showed only cytosolic immunoreactivity (**Fig. 2.7**). Because of ANXA8's previously identified interaction with the cytoskeleton [87], our finding may further indicate a possible function for WDR72 involved in cytoskeletal dynamics that facilitate the progression of MVBs or the rearrangement of cytoskeletal components for directing vesicle transport or ameloblast morphology cycling between RA and SA phenotypes. More data suggesting a role for WDR72 involved in cytoskeletal dynamics will be discussed in the following chapter.

DISCUSSION

During enamel mineralization, maturation-stage ameloblasts are known to remove the hydrolyzed matrix proteins from the extracellular developing enamel into intracellular vesicles along the degradation pathway [58]. In Chapter 1, we found that *Wdr72*$^{-/-}$ ameloblasts had decreased intracellular amelogenins, whereas the enamel matrices retained significant amounts of organic material. The work described in this chapter demonstrates a clear functional role for WDR72 in vesicle transport through the endocytic pathway.

Although endocytosis is present in all cell types and maturation-stage ameloblasts have an active endocytic role during enamel formation, little is currently known about the mechanisms of internalized material during the maturation stage. Endocytosis is a general term that describes the internalization and cycling of fluid, solutes, macromolecules, plasma membrane components, and particles. Huotari and Helenius described the classical endocytosis model as having two main circuits: (1) a recycling circuit that transports material back to the plasma membrane, and (2) a degradative circuit that moves macromolecules in conjunction with the trans-Golgi network (TGN) to be digested by lysosomes [89]. The recycling pathway helps to move endocytosed cargo and can join with the secretory pathway involved in exocytosis. Within the degradative pathway, there exists a unidirectional feeder pathway mediated by late endosomes (LE) or multivesicular bodies (MVB). LE/MVBs interact closely with the trans-Golgi network (TGN) to regulate transport of lysosomal components prior to fusing with lysosomes. This allows maintenance, diversification, and expansion of the degradative system.

We found that in ameloblasts lacking *Wdr72*, although HRP was initially taken up into maturation-stage ameloblasts, transport was delayed, indicating that WDR72 modulates the endocytic pathway. Our finding that clathrin localization was dysregulated points to the possibility that WDR72 mediates the transition of clathrin-coated vesicles. Clathrin is the major

coat protein of both (1) coated pits of endocytic vesicles prior to fusion with early endosomes, and (2) vesicles transporting lysosomal hydrolases to acidic vesicles along the degradation pathway (ie. late endosomes, multivesicular bodies, and lysosomes). These results support a previously published finding that WDR72 interacts with adaptor protein AP2, which recruits clathrin to the membrane to initiate vesicle formation [90].

However, an argument against a direct interaction between WDR72 and clathrin is our finding that that the timing of the clathrin dysregulation in *Wdr72*$^{-/-}$ mice was observed later than the onset of maturation. To further investigate this, we specifically determined WDR72 involvement in clathrin-mediated endocytosis by immunostaining for the clathrin-interacting protein, dynamin II.

Dynamin II is Ca^{2+}-dependent interactor with clathrin and the cytoskeleton to facilitate the scission of the budding membrane to create a completed vesicle, specifically during clathrin-mediated endocytosis, one of the initial uptake steps in the endocytic pathway [91–94]. It is unclear why we saw a retention of dynamin in maturation-stage ameloblasts, but it is possible that this is also related to the dysregulation of clathrin with increased intracellular localization and an apparent reduced recruitment back to the plasma membrane coinciding with the RA and SA cycling.

Towards the end of the degradation pathway, LE/MVBs are the last vesicle type before reaching the lysosome. Because annexin-A8 (ANXA8) was the only LE/MVB marker found to be up-regulated in maturation-stage ameloblasts [85], we immunostained for it in our *Wdr72*$^{-/-}$ mice. When *Wdr72* is deleted, ANXA8 also showed a dysregulated localization, including localized to the nuclei of *Wdr72*$^{-/-}$ ameloblasts (**Fig. 2.7**).

Taken together these results show a clear role for WDR72 at multiple stages of the endocytic pathway, particularly in the processing and degradation of extracellular proteins. The absence of WDR72 has the ultimate outcome of delayed endocytosis and an apparent disruption to the localization of multiple endocytic vesicles and their functions. In the final chapter, we investigate the possible mechanisms by which WDR72 functions endocytosis by focusing on the mechanisms that direct the degradative pathway and further elucidate its role in RA and SA cycling.

CHAPTER 3: Investigating WDR72's role in the degradative pathway

In the previous chapter, we demonstrated that WDR72 is a necessary contributor to the complex and dynamic endocytic system by identifying the progression of tracers and key vesicle markers. Endocytic vesicles, however, have a variety of destinations once inside the cell and are routed within a complex and dynamic system to enable cargo to be returned to the plasma membrane, exchanged with the Golgi apparatus, or destined for lysosomes to be degraded. While our data thus far point to the possibility of WDR72's function involved in the degradative pathway, the following chapter aims to narrow the function towards WDR72 as a key regulator of LE/MVB maturation within the degradative pathway.

The endocytic system is a series of intracellular pathways comprised of vesicle transport steps that enable the external environment to be removed, recycled, and digested in order to process, transport, and destroy cargo. A more detailed overview of this system was described in Chapter 2, as well as in reviews by Huotari and Helenius [89]. Briefly, however, two major circuits exist after material is internalized into the cell: (1) recycling of cargo back to the plasma membrane, and (2) degradation of cargo into lysosomes. The latter circuit is largely regulated by late endosomes (LE), or multivesicular bodies (MVB), which interact closely with the trans-Golgi network (TGN) and lysosomes to mediate the transport of lysosomal components between them. This degradative pathway begins with the conversion of early endosomes (EE) into LE/MVBs and ends with the fusion of LE/MVBs with lysosomes.

A major function of the degradative pathway is the maturation of LE/MVBs. Once formed, they undergo several changes in order to fully mature, which involve five major processes: (1) input from Rab GTPase switches [95,96], (2) acidification of the lumen to a pH of 6.0-4.9 via H^+, Ca^{2+}, Na^+, and K^+ exchange [97–100], (3) formation of intralumenal vesicles (ILV) to sort cargo for degradation in lysosomes [101], (4) association with Arf1/COPI [102], and (5) movement from the

peripheral cytoplasm to the perinuclear region of the cell, where they fuse with lysosomes and endolysosome hybrid organelles [103]. Almost all of these processes contributing to LE/MVB maturation have been linked to WDR72. For example, the closest human homolog to WDR72, WDR7, is a known interactor with Rab GTPase effectors [104]; WDR72 has the highest structural homology with COPI (Chapter 1) [39]; and loss of WDR72 leads to both premature LE/MVB marker localization to the nucleus (**Fig. 2.6**) and significant delays in HRP transport to the perinuclear region of the cell to co-localize with lysosomes (**Fig. 2.3**).

The focus of this final chapter is to provide further evidence of WDR72's role in the degradative pathway and to specifically elucidate its role in LE/MVB maturation as a mechanism for enamel mineralization. Understanding of WDR72's precise function will not only enhance our current knowledge of endocytic processing in maturation-stage ameloblasts, but also how the degradative pathway interacts with other well-studied functions during enamel maturation, such as ion transport and modulation.

RESULTS

Ameloblast-like cells (ALC) without WDR72 are able to uptake hydrolyzed amelogenin fragments but cannot process these amelogenins to lysosomes

While our previous *in vivo* studies provided an excellent model for tracing the processing of HRP in endocytosis, to further examine WDR72 function in either the recycling or degradative circuit, we developed an *in vitro* model. To do this, we deleted the *Wdr72* gene in the ameloblast-like cell line (ALC) [105,106], by targeted CRISPR/Cas9 technology. For control cells, we targeted crRNA as recommended by manufacturer's instructions, and for the knockout cell lines, we targeted the 10 base pairs deleted in our identified human mutation. DNA sequencing results showed a successful 10 base pair deletion in two different cell clones (E8 & G4) with the same deletion mutation at exon 12, causing a frameshift in the reading frame (**Fig. 3.1**).

Immunocytochemistry was used to assess relative amounts of WDR72 protein and showed dramatically reduced WDR72 in the knockout cell lines (**Fig. 3.1**).

These cell lines enabled us to test *in vivo* whether the lack of *Wdr72* led to a defect in LE/MVB maturation and also track amelogenins through the degradation pathway. A previous study demonstrated that in *Wdr72*$^{-/-}$ mice, hydrolyzed amelogenin fragments of size 20kD were retained in the matrix [107], therefore, we decided to simulate *in vivo* processing of extracellular amelogenins by adding recombinant amelogenin of size 20kD to our cells. To trace amelogenins through the degradative pathway of ameloblasts, we incubated control and *Wdr72*-deficient ALCs with LysoTracker and fluorescently tagged recombinant amelogenin 20kD (rAMG20). LysoTracker is a fluorescent marker of vesicles and is commonly used to specifically label lysosomes, but has also been found to detect LE/MVBs as well due to their low acidity at more mature stages [108].

We found that rAMG20 was internalized by both control and *Wdr72*$^{-/-}$ cells. However, while control cells demonstrated co-localized rAMG20 with large LysoTracker-positive vesicles, cells without *Wdr72* lacked co-localization of rAMG20 with LysoTracker, and these LysoTracker-positive vesicles were much smaller in size compared to controls (**Fig. 3.2**). These findings are consistent with our HRP *in vivo* studies showing lack of localization to acidic vesicles (**Fig. 2.3**) and further support our finding that WDR72 functions in the transport of exogenous material through the degradation pathway to lysosomes. Specifically, the general presence of small acidic vesicles in the *Wdr72*$^{-/-}$ cell lines and lack of movement of rAMG20 to larger perinuclear vesicles as observed in *Wdr72*$^{-/-}$ cells (*in vitro*) suggest that WDR72 is required for maturation of LE/MVBs to lysosomes (see discussion section below).

Ultrastructure reveals disrupted ameloblast ruffled border and small vesicles in Wdr72$^{-/-}$ mouse ameloblasts

Our *in vitro* experiments showed greater detail of vesicles and endocytosis in *Wdr72*$^{-/-}$ cells, illustrating smaller vesicles present in *Wdr72*$^{-/-}$ cells (**Fig. 3.2**). The presence of smaller vesicles in these cells may point to a disruption in the formation of intralumenal vesicles (ILV), which is an essential process for LE/MVB maturation. As LE/MVBs mature, they become larger and an increase in these ILVs are formed. When fewer ILVs form, cargo accumulates in endosomes with abnormal morphology [109]. The inefficient transport of HRP *in vivo* and amelogenins *in vitro*, as well as the presence of smaller vesicles in the *Wdr72*$^{-/-}$ cell lines (**Fig. 2.3 & 3.2**), suggest that the loss of WDR72 prevented formation of these acidic vesicle types.

To further explore the possibility that WDR72 is associated with vesicle formation, we examined maturation-stage ameloblasts at the ultrastructural level using transmission electron microscopy (TEM). TEM is an excellent tool for visualizing organelles to detect more subtle phenotypes involved in a cell's structure. Consistent with our *in vitro* findings, we found that *Wdr72*$^{-/-}$ ameloblasts showed smaller vesicles compared to the *Wdr72*$^{+/+}$ ameloblasts (**Fig. 3.3**).

Additionally, our TEM results illustrated that large components of the membrane were disorganized, particularly at the ruffled border and the endoplasmic reticulum (**Fig. 3.3C & D**). This indicates that WDR72's role in the degradation pathway may be linked to membrane structure or turnover, specifically at the apical border. *Wdr72*$^{-/-}$ mice revealed a blunted and disorganized ruffled border, which is the site of an abundant vesicle presence, and thus membrane turnover, during enamel maturation. *Wdr72*$^{-/-}$ ameloblasts also showed an increase in the endoplasmic reticulum (**Fig. 3.3**), which is a major interacting organelle (along with the trans-Golgi network) throughout the degradative pathway during LE/MVB maturation to provide a membrane reserve [89]. Finally, *Wdr72*$^{-/-}$ mitochondria also appeared deficient.

Ameloblast modulation and enamel matrix pH are disrupted in Wdr72$^{-/-}$ mice

As previously discussed in the introduction and chapter 2, ameloblasts undergo large morphological changes during the maturation stage involving membrane turnover, both with its intracellular organelle rearrangements, as well as the apical border cycling between ruffle-ended and smooth-ended border phenotypes. In a variety of cell types, vesicle transport has been shown to be a key contributor to membrane turnover [110]. Additionally, lysosomal storage diseases associated with endocytic perturbance illustrate downstream effects on other cell organelles, such as defects in mitochondria, ER, Golgi, etc. [111]. It is possible, then, that WDR72 has a functional role in LE/MVB maturation integrated with membrane turnover that leads to faulty regulation of ion transporters and ameloblast modulation. In fact, previous work showed that *Wdr72*$^{-/-}$ mice mislocalized ion channel NCKX4 that spans the cell membrane [107].

To determine whether the membrane changes observed in *Wdr72*-deficient models were linked to modulation, we used matrix pH and calcium (Ca^{2+}) staining to indirectly compare ameloblast modulation in *Wdr72*$^{+/+}$ to *Wdr72*$^{-/-}$ mice. A typical feature of ruffle-ended ameloblasts (RA) and smooth-ended ameloblasts (SA) is their matrix pH, where RA show an acidity of 5.5, whereas SA show an acidity of 7.0 [1]. The Ca^{2+} sensing dye, glyoxal bis (2-hydroxyanil) (GBHA) [112], which stains at neutral pH, has also been shown to be a reliable marker to identify modulations between SAs and RAs, with the matrix under SAs staining red and the matrix under RAs having no stain [113].

We found that both *Wdr72*$^{+/+}$ and *Wdr72*$^{+/-}$ incisors demonstrated typical GBHA banding patterns observed during SA modulation cycles, whereas *Wdr72*$^{-/-}$ matrices showed a lack of banding pattern altogether and stained the entire matrix (**Fig. 3.4**). We separately stained these enamel matrices with Universal pH indicator dye, which showed a loss of matrix acidification in the

Wdr72$^{-/-}$ mice, consistent with both the downregulation of ion transporters and with disrupted ameloblast modulation [114]. As expected, *Wdr72*$^{+/+}$ and *Wdr72*$^{+/-}$ mice had a neutral pH (≈7) at the secretory stage matrix, which was followed by a brief acidified section at the transition stage and beginning of enamel maturation (**Fig. 3.4**). During the maturation stage in control mice, the enamel matrix cycled between acidic and neutral pHs. In contrast, the enamel of *Wdr72*$^{-/-}$ mice remained neutral pH throughout secretory and maturation stage (**Fig. 3.4**).

Not only do the lack of banding patterns now link WDR72 function with ameloblast modulation, but also given that both Ca^{2+} and H^+ transport to the matrix was disrupted in *Wdr72*$^{-/-}$ enamel, it is clearer that WDR72's role in the endocytic pathway is also linked to vesicle trafficking of ion transporters also essential for proper enamel formation. Numerous papers have found links between vesicle formation and ion transport, and this interaction is largely associated with the degradative pathway during which LE/MVBs mature through regulation of H^+ and Cl^- influx, and efflux of Ca^{2+}, Na^+ and K^+ [98–100]. It has long been known that the regulation of Ca^{2+} and H^+ transport is critical for enamel mineralization [56,112,115,116].

The formation of RAs has also been shown to be associated with vacuolar H^+-ATPase (v-ATPase) at the apical border, which coincides with GBHA staining [117,118]. We immunolocalized v-ATPase and found that similar to previously described work in normal ameloblasts, immediately after transition stage, *Wdr72*$^{+/+}$ ameloblasts showed v-ATPase along the apical border of ruffle-ended ameloblasts, followed by a more diffuse staining in the smooth-ended ameloblasts (**Fig. 3.5**). In the *Wdr72*$^{-/-}$ mice, similar to the timing observed for clathrin (**Fig. 2.4**), v-ATPase remained diffusely stained throughout the ameloblast, rather than returning to an apical aggregate like the control mice. This suggests a dysregulation of v-ATPase for acidifying vesicles in *Wdr72*$^{-/-}$ ameloblasts and that vesicles are inhibited from returning to the plasma membrane.

Loss of Wdr72 affects v-ATPase in ameloblasts, but not through a dependent mechanism

We next investigated whether WDR72 regulation of v-ATPase leads to alterations in vesicle acidification. V-ATPase function largely contributes to vesicle acidification in LE/MVBs and lysosomes, aiding in their progressive acidification as LE/MVBs mature and progress through the degradative pathway. V-ATPase has also been shown to be regulated by the closest human homolog to WDR72, WDR7. WDR7 (under the alias "Rabconnectin-3β") has a function in regulating the endocytic pathway by directly monitoring v-ATPase activity in *Drosophila* [73,74], and was more recently discovered to inhibit lysosome acidification in M-1 mouse cortical collecting duct cells by inhibiting v-ATPase activity [119]. Bafilomycin is a reversible drug that specifically inhibits the activity of v-ATPase. Therefore, to further tease apart the role of WDR72 in LE/MVB maturation and vesicle acidification, we explored whether loss of WDR72 resulted in the ability for vesicles to re-acidify following a bafilomycin challenge.

Using the newly developed *Wdr72*$^{-/-}$ cell lines (described above), we tested whether WDR72 regulated lysosome acidification via v-ATPase in a similar manner to experiments of WDR7 [119]. Control and both knockout clones were first treated with the v-ATPase inhibitor, bafilomycin, followed by a 3-hour washout recovery period, and labeled with LysoTracker, a fluorescent pH indicator dye of vesicles with low pH (ie. LE/MVBs and lysosomes). Because LysoTracker is a membrane-permeant dye, after 3-5 minutes, cells were washed and lysed to release the LysoTracker fluorescence, which was measured using a bioassay reader.

We found that prior to bafilomycin treatment, *Wdr72*$^{-/-}$ clones demonstrated similar fluorescence labeling with LysoTracker as compared to controls (**Fig. 3.6**). All cell groups significantly decreased in fluorescence in the presence of bafilomycin, and both *Wdr72*$^{-/-}$ clones were able to re-acidify lysosomes after challenge with the v-ATPase inhibitor similar to cells with the control

vector. When considered with the v-ATPase immunostaining results (**Fig. 3.5**), these data suggest that WDR72's role in LE/MVB maturation is independent of vesicle acidification.

WDR72 may direct vesicle formation and membrane turnover by recruiting the cytoskeleton

Because our v-ATPase results did not link WDR72 function with vesicle acidification involved in the degradative pathway, we investigated a final process necessary for LE/MVB maturation to occur. An important influencing factor on the degradative pathway is LE/MVB motility towards lysosomes, where microtubules are required for processing of LE/MVBs [120]. In addition, cytoskeletal components have been found to affect membrane turnover [121], pointing to a possible link to the modulation defects observed in the *Wdr72*$^{-/-}$ *mice*. Therefore, we investigated whether *Wdr72* deletion leads to defects in cytoskeletal structure. Here, we focused on two main cytoskeletal components involved in the degradative pathway of endocytosis: alpha-tubulin and F-actin.

We immunostained control and *Wdr72*$^{-/-}$ ALC lines for alpha-tubulin and F-actin. In control cells, alpha-tubulin was organized into the canonical web-like structures with assembled focal points along the cell border (**Fig. 3.7**). However, in the *Wdr72*$^{-/-}$ cells, tubulin was largely disorganized at the border, and unlike the control cells, did not appear to extend to the cell membrane border. This staining pattern in the *Wdr72*$^{-/-}$ cells suggests defects in microtubule assembly and organization. Tubulin staining in the nucleus of *Wdr72*$^{-/-}$ cells (**Fig. 3.7**) further suggests defects in microtubule recruitment to the apical border.

Immunostaining for F-actin showed that there was no difference between control and *Wdr72*$^{-/-}$ cells. Although both actin and microtubules are essential components of the cell's cytoskeletal architectures, actin is thought to provide contractile forces for movement, whereas microtubules build a polarized network that facilitate organelle and protein movement within the cell. When

considered with the lack of organization at the ruffle-ended border and the endoplasmic reticulum (**Fig. 3.3**), and lack of progression of endocytosed material throughout the degradative pathway in *Wdr72*$^{-/-}$ ameloblasts (**Fig. 2.3**), these results point to a role of WDR72 in microtubule assembly. Microtubules have a key function in the transport and maturation of LE/MVB vesicles, and their disruption would lead to reduced efficiency of the endocytic degradative pathway, as we have shown both *in vivo* and *in vitro* with the absence of WDR72. Therefore, taken together, data presented in this chapter have pointed to the possibility that WDR72 facilitates the degradative pathway through the regulation of LE/MVB maturation via microtubule assembly or recruitment.

DISCUSSION

In this chapter, we described *in vivo* ultrastructural and *in vitro* mechanistic studies that show reductions in vesicle formation that point to a role of WDR72 in regulating the degradative pathway of endocytosis and in ameloblast modulation, possibly via membrane turnover. During endocytosis, membrane turnover can range from 50-180% return to the plasma membrane every hour [110], and maturation-stage ameloblasts undergo significant membrane changes at the apical border by fluctuating between ruffle-ended (RA) and smooth-ended (SA) phenotypes. Our findings show that unlike WDR7, WDR72 does not have a direct role in vesicle acidification, but rather WDR72 has a general role in vesicle maturation during the LE/MVB stages and in membrane remodeling.

The cytoskeleton is a major contributor to the degradative pathway, specifically in facilitating the maturation of LE/MVBs, and is an important component to the cell's structure. Vesicle fission, fusion, and maturation through this pathway rely heavily on the cell's cytoskeleton as a structural framework and network to stabilize the forming vesicle and to serve as a track for transportation [89,122], specifically in the regulation of cargo transport from EE to LE [123]. As

LE/MVBs are transported along microtubules via motor proteins, the net movement is always towards microtubule organizing centers that are located in the perinuclear region of the cell, where most lysosomes localize [120]. Interestingly, WD40-repeat proteins have been shown to have microtubule assembly functions, likely due to their structural configuration of beta-propeller sheets that serve as sites for protein docking (ie. multiple protein-protein interactions) that can serve as stabilizers for the dynamic movement. Specifically, WDR47 and WDR62 have both been identified as integral microtubule-associated proteins in neurodevelopment [124,125].

In maturation-stage ameloblasts, little is known about the cytoskeleton's relationship with the degradative pathway, however one report has demonstrated that microtubule inhibitors affect vesicle size in secretory ameloblasts [126]. An additional indication that WDR72 may have a role in cytoskeletal dynamics is our observation under TEM that the size of the ER is increased in *Wdr72*$^{-/-}$ maturation-stage ameloblasts as compared to controls (**Fig. 3.3**). The ER structure and shape have been shown to be stabilized by proteins that interact with microtubules [127]. An effect of WDR72 on microtubule formation, therefore, is a potential mechanism that would likely affect vesicle formation, ER structure, and formation of the ruffled border in maturation-stage ameloblasts.

The smaller vesicles appearing both *in vivo* and *in vitro Wdr72*$^{-/-}$ models (**Fig. 3.2 & 3.3**) further support the function for WDR72 in microtubule formation. *Wdr72*$^{-/-}$ mice and cells both showed lack of formation of larger vesicles that not only localized in the cell periphery (**Fig. 3.2**) but also did not enlarge (**Fig. 3.3**). Transport of LE/MVBs along microtubules is thought to be essential for LE/MVB maturation, as small LE/MVBs located close to the plasma membrane progress to be larger and closer to the nucleus [128]. LE/MVBs differ in size, ranging in diameter from 250nm to 1000nm, and they progressively enlarge as they mature [89]. As maturation occurs, LE/MVBs

move from the peripheral cytoplasm to the perinuclear region of the cell, where they fuse with lysosomes and endolysosome hybrid organelles to digest the internalized cargo [103].

In summary, the data presented in this chapter have pointed to the exciting possibility that WDR72 may have a role in facilitating the transport of LE/MVBs to enable their maturation of these vesicles. Our findings show that WDR72's function is not only regulating maturation in the degradative pathway, but also possibly via cytoskeleton recruitment. This means, then, that deficiency of vesicle transport to facilitate removal of proteins from the enamel matrix through the cell for digestion is a cause for hypomineralized enamel formation in AI due to mutations in the *Wdr72* gene. Further studies to investigate the possible effect that this function of WDR72 has in other cells and tissues (ie. brain, heart, intestine, kidney) will allow us to not only enhance our understanding of enamel formation but also will allow us to further understand the dynamics of intracellular transport and the role of WDR72 in these systemic processes.

FIGURES

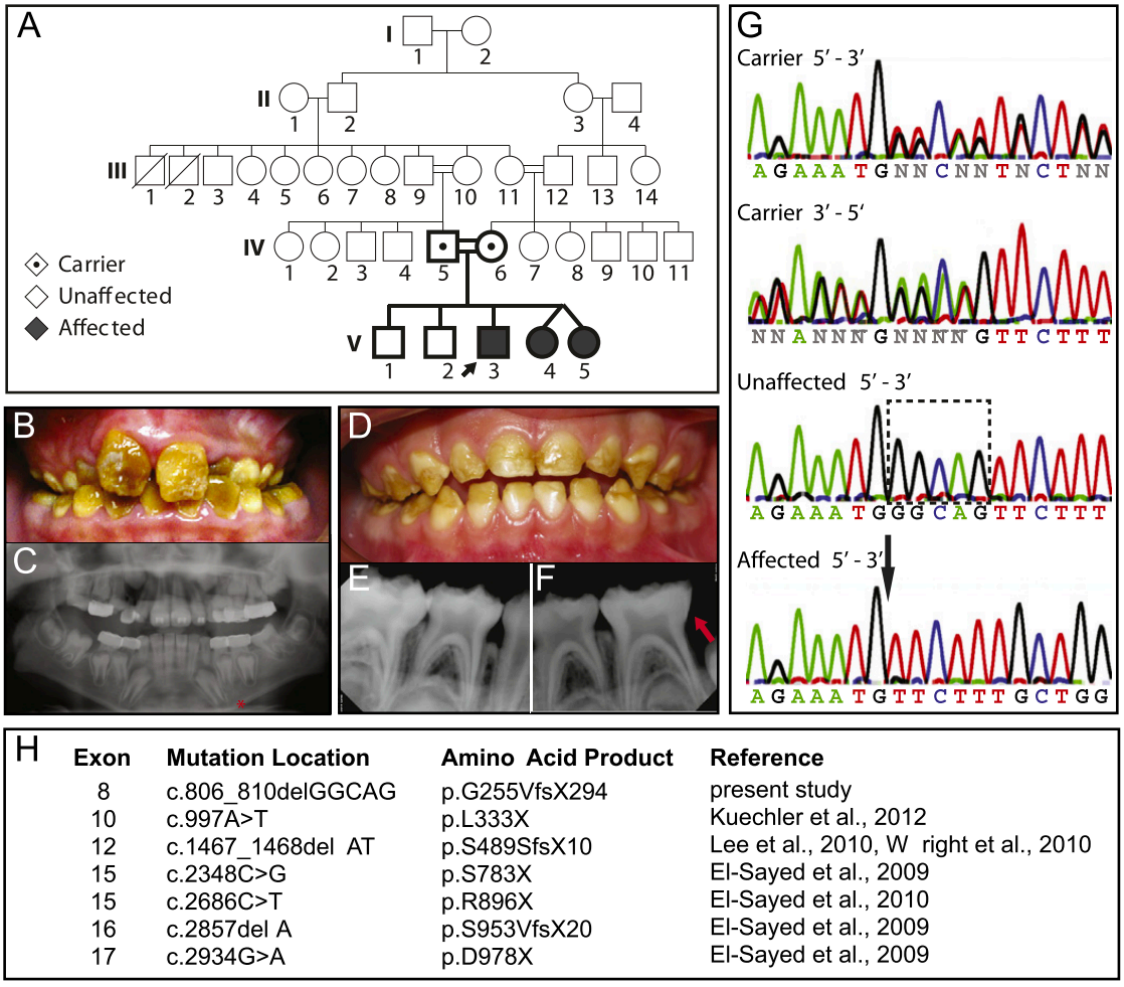

H

Exon	Mutation Location	Amino Acid Product	Reference
8	c.806_810delGGCAG	p.G255VfsX294	present study
10	c.997A>T	p.L333X	Kuechler et al., 2012
12	c.1467_1468del AT	p.S489SfsX10	Lee et al., 2010, W right et al., 2010
15	c.2348C>G	p.S783X	El-Sayed et al., 2009
15	c.2686C>T	p.R896X	El-Sayed et al., 2010
16	c.2857del A	p.S953VfsX20	El-Sayed et al., 2009
17	c.2934G>A	p.D978X	El-Sayed et al., 2009

Figure 1.1. Identification of a novel 5-base pair deletion in exon 8 of the Wdr72 gene in patients affected with autosomal recessive AI of a pigmented and hypomaturation phenotype
(A) Family pedigree with autosomal recessive inheritance of Amelogenesis imperfecta (AI). Double lines (=) symbolize consanguineous unions, black arrow denotes the proband, emboldened shapes identify family members analyzed for DNA sequencing. (B) Permanent dentition of the male proband (V3; 10.5 y.o.) was pigmented yellowish-brown with a loss of tooth enamel at the surface. (C) The proband's panoramic radiograph revealed hypomineralized enamel in unerupted teeth, missing first permanent molars (teeth #3, 19 and 30), and delayed eruption sequences in primary canines and molars (red asterisk). (D) Representative photograph of one affected twin sister (V4; 4 y.o.) showing primary dentition also exhibiting a hypomaturation enamel phenotype on the occlusal surfaces of erupted teeth. (E, F) Lower PAs also showed a loss of enamel in erupted teeth with similar radiopacity to dentin, indicating hypomineralization (red arrow). (G) Comparisons of representative chromatograms for carrier, unaffected, and affected individuals revealed a 5-base pair deletion in affected patients, which localized to exon 8 of the *Wdr72* gene and matched with the AI phenotype. The dotted box encompasses the nucleotides absent in affected patients with a black arrow pointing to the deletion site. (H) List of reported *Wdr72* mutations in association with AI.

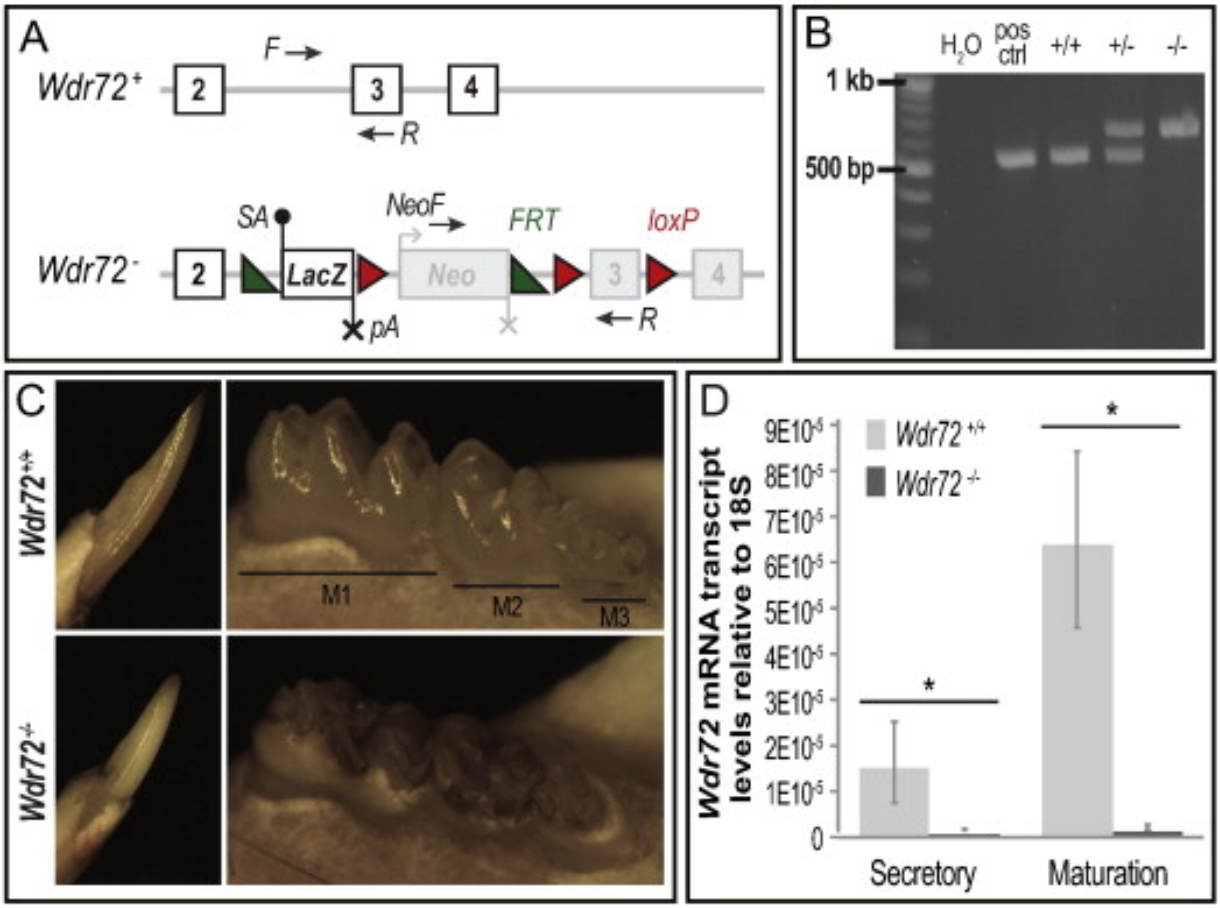

Figure 1.2. Successful Wdr72−/− mouse model exhibits hypomaturation enamel phenotypes
(A) *Wdr72* wildtype ($^{+}$) and mutant (−) allelic variants. The *Wdr72* mutant allele (*Wdr72* $^{-}$) is a functional knockout through splicing in a LacZ gene reporter containing a high affinity splice acceptor (SA, black dot) and termination sequence (pA, black X) prior to the critical exon 3. The encoded mutant transcript is a truncated *Wdr72* at exon 2 fused to *LacZ*. Neomycin (*Neo*) is independently regulated, containing its own promotor (gray bent arrow) and termination sequence (gray X). Numbered white boxes represent coded exons under the *Wdr72* promotor, whereas numbered gray boxes represent exons not encoded under the *Wdr72* promotor. Black arrows denote primer locations used for genotyping. Green triangles, *frt* sites; Red triangles, *loxP* sites; (B) PCR genotyping of isolated mouse DNA from *Wdr72*$^{+/+}$, *Wdr72*$^{+/-}$, and *Wdr72*$^{-/-}$ tail biopsies. Amplicon sizes of *Wdr72*$^{+}$ allele, 520 bp; and *Wdr72*$^{-}$ allele, 633 bp. (C) Representative photographs of 6-week-old male mandibular incisors (left panels, buccal view) and molars (right panels, lingual view) after soft tissue removal. *Wdr72*$^{-/-}$ enamel was lost from the intact dentin surface when teeth erupted into the oral cavity. *Wdr72*$^{-/-}$ enamel also appeared opaque and stained as compared to the translucent *Wdr72*$^{+/+}$ enamel. (D) Quantitative real-time PCR (qPCR) of micro-dissected secretory and maturation-stage ameloblasts. *Wdr72* transcript is successfully knocked out in *Wdr72*$^{-/-}$ mice and is significantly up-regulated from secretory to maturation stages in *Wdr72*$^{+/+}$ ameloblasts (n = 3, $P < 0.05$). Error bars represent ± SD of the mean.

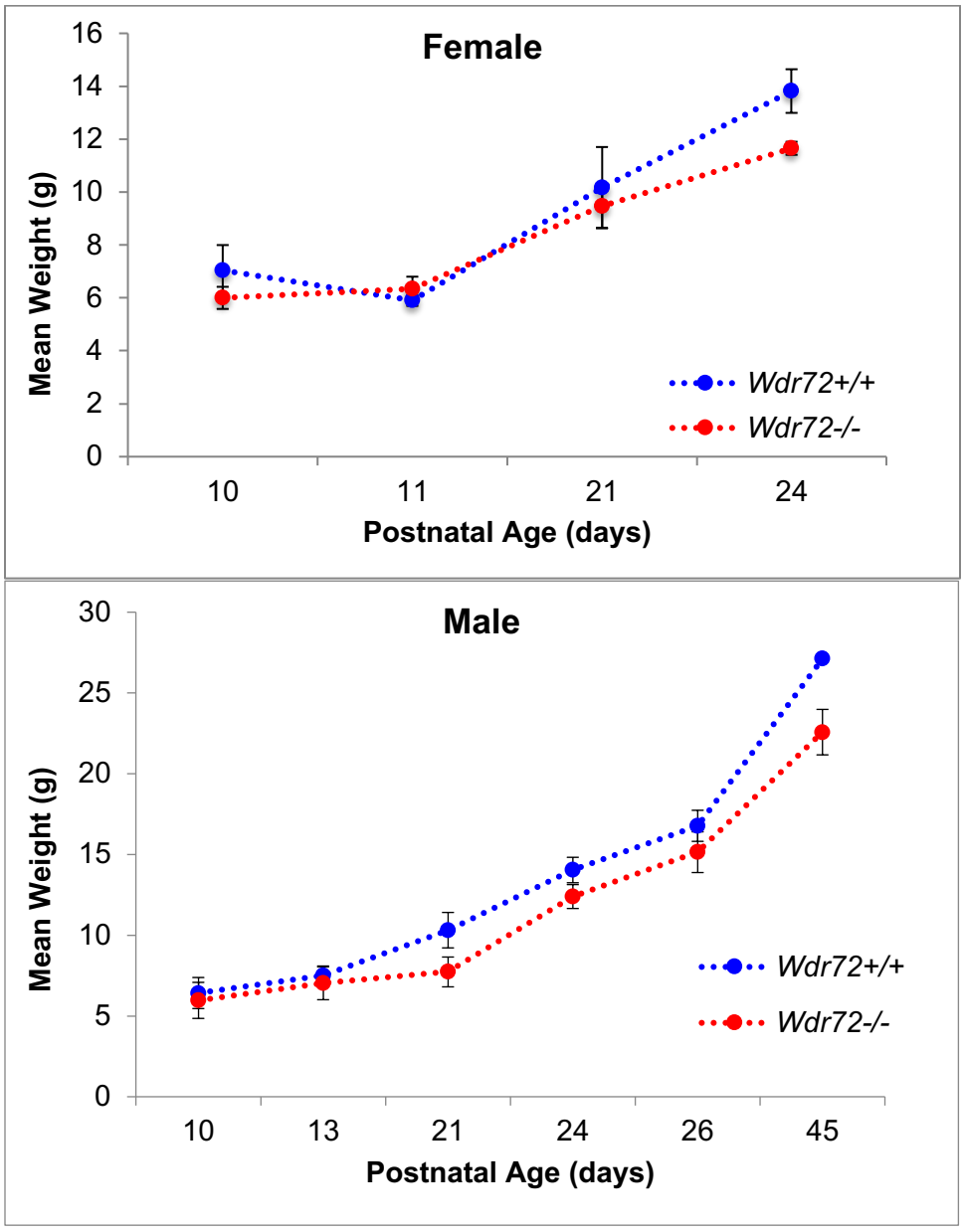

Figure 1.3. Average weights of Wdr72$^{+/+}$ and Wdr72$^{-/-}$ mice at various postnatal ages. *Wdr72$^{-/-}$* female mice show significantly decreased weights at P24, and *Wdr72-/-* males are significantly decreased at from P21 to P45 relative to *Wdr72$^{+/+}$* controls (n≥3; P>0.05). Murine teeth erupt at P14, and weaning age is P21. Differences in weights between *Wdr72$^{+/+}$* and *Wdr72$^{-/-}$* mice occurring at these ages suggest difficulty in chewing a hard-food diet. Error bars represent ±SD of the mean.

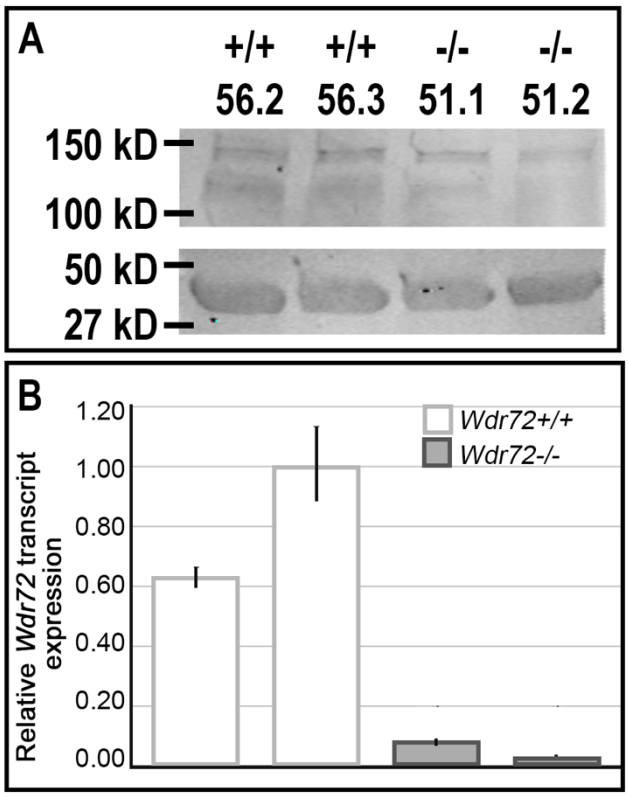

Figure 1.4. Wdr72$^{+/+}$ and Wdr72$^{-/-}$ kidneys showing knockout of WDR72 protein and mRNA. (A) Western blot of *Wdr72*$^{+/+}$ and *Wdr72*$^{-/-}$ kidneys of male mice at postnatal day 24 using WDR72 (top) and beta-actin (bottom) antibodies for detection. Expected weight for WDR72 protein is 123 kD (middle band), and top band shows non-specific protein. Beta-actin (45 kD) was used as a loading control for total protein (bottom band). *(B)* Quantitative RT-PCR (qPCR) of the same *Wdr72*$^{+/+}$ and *Wdr72*$^{-/-}$ kidneys used for western blot and normalized to 18S. *Wdr72*$^{-/-}$ mice have significantly decreased transcript relative to *Wdr72*$^{+/+}$ controls.

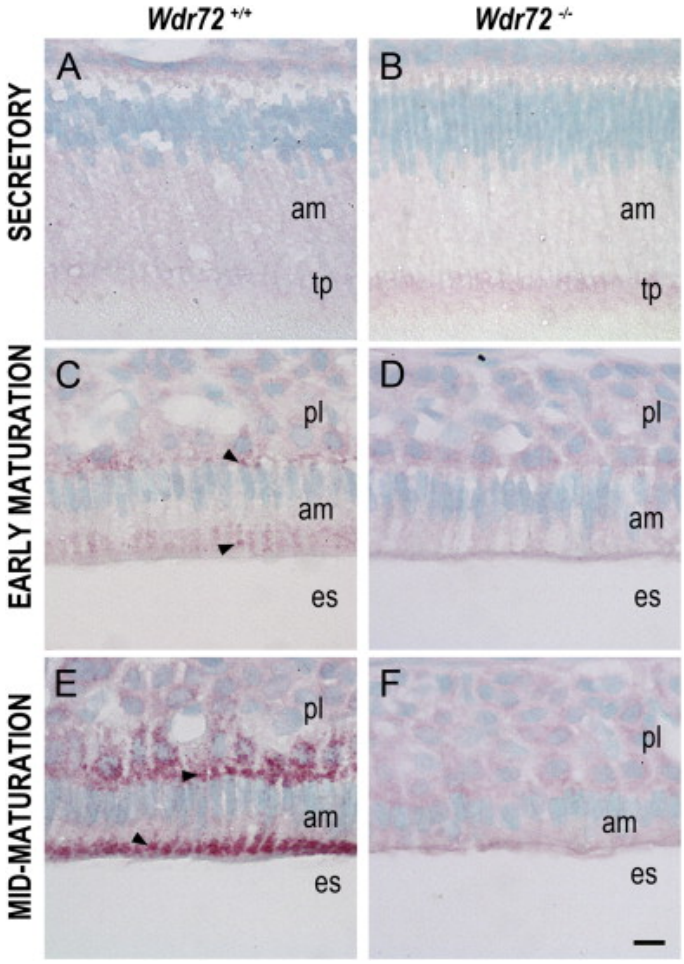

Figure 1.5. WDR72 immunolocalizes to vesicle-like puncta in Wdr72$^{+/+}$ maturation-stage ameloblasts and shows protein-level knockout in Wdr72$^{-/-}$ mice.
Representative sagittal sections of P10 male *Wdr72*$^{+/+}$ and *Wdr72*$^{-/-}$ mandibles immunostained with a polyclonal rabbit antibody to WDR72 peptide. (A) In *Wdr72*$^{+/+}$ mice, immunoreactivity (red) was diffusely positive in secretory ameloblasts and increased upon entry into the maturation stage (C, E), immunolocalizing to vesicle-like structures at the basal and apical ends (arrowheads). (B, D, F) Slight non-specific background immunoreactivity was present in *Wdr72*$^{-/-}$ ameloblasts. am, ameloblast; es, enamel space; pl, papillary layer; tp, Tomes' process. Scale bar, 10 μm.

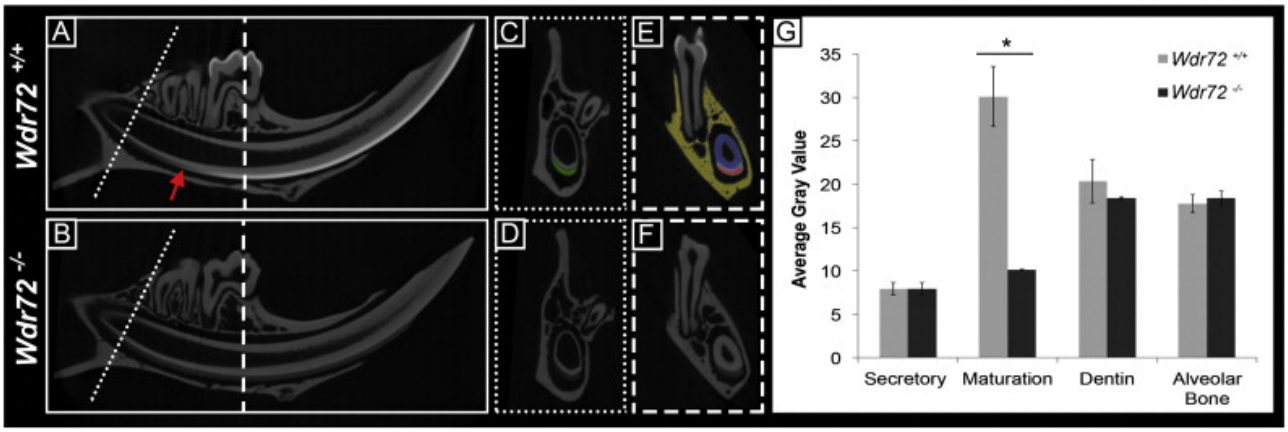

Figure 1.6. Hypomineralized enamel phenotype in Wdr72$^{-/-}$ mice occurs at the onset of maturation stage.
Representative sagittal (A, B) and cross sectional (C–F) microCT images of *Wdr72*$^{+/+}$ and *Wdr72*$^{-/-}$ 6-week-old male mandibles. In the continuously growing incisor, *Wdr72*$^{+/+}$ enamel mineralization increased at the onset of maturation stage to form an enamel layer of increasing relative intensity (A), which remained radiolucent in the *Wdr72*$^{-/-}$ mice (B). Red arrow marks transition stage. Similar relative intensity comparisons between the *Wdr72*$^{+/+}$ and *Wdr72*$^{-/-}$ enamel were observed in fully formed molars (E, F). Dotted and dashed lines mark the sites along the continuously growing incisor where coronal planes were taken at secretory stage (C, D) and maturation (E, F) stages of enamel, respectively. Dentin and alveolar bone showed no differences (A–D). Green, red, blue, and yellow shading overlays on the *Wdr72*$^{+/+}$ cross-section panels (C & E) represent the regions of interest that were used to quantify the average gray values seen in the bar graph; green, incisor enamel at secretory stage; red, incisor enamel at maturation stage; blue, dentin; yellow, alveolar bone. Quantification of these observations is depicted in the graph to the right (G). Error bars represent ± SD of the mean (n = 3). Paired student *t*-tests between *Wdr72*$^{+/+}$ and *Wdr72*$^{-/-}$ average gray scale values with a threshold for *P*-values at < 0.05.

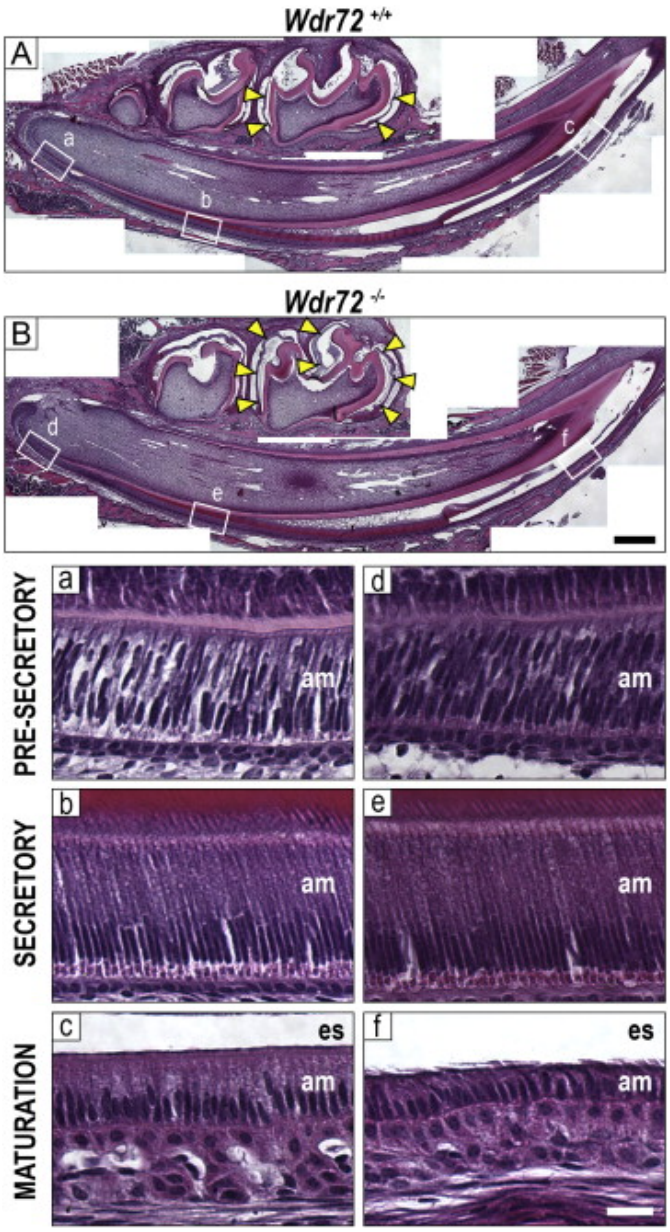

Figure 1.7. Enamel matrix and ameloblasts display maturation-stage specific phenotypes in Wdr72$^{-/-}$ mice.
Representative sagittal sections of *Wdr72*$^{+/+}$ (A) and *Wdr72*$^{-/-}$ (B) P10 male mandibles stained with hematoxylin and eosin. Unerupted first molars are at maturation stage, showing a lack of organic material (yellow arrows) in the enamel space of the *Wdr72*$^{+/+}$ mice but retention in the *Wdr72*$^{-/-}$. Lettered white boxes correspond to enlarged images below. Black scale bar, 400 μm. Bottom panels show *Wdr72*$^{+/+}$ (a–c) and *Wdr72*$^{-/-}$ (d–f) ameloblasts at different stages of differentiation, showing the spectrum of enamel development along the continuously growing incisor. During maturation stage, *Wdr72*$^{-/-}$ ameloblasts (f) are shorter in height compared to those of *Wdr72*$^{+/+}$ mice (c), while earlier stages appear to have morphologically normal ameloblasts. am, ameloblasts; es, enamel space. White scale bar, 20 μm.

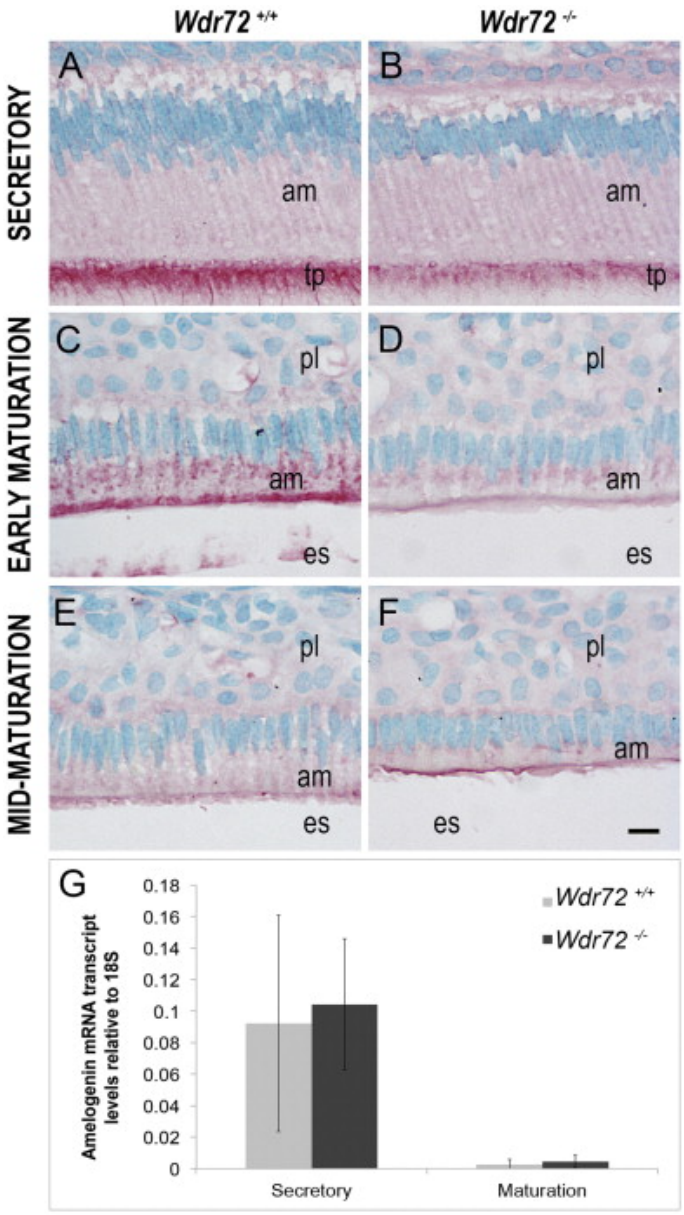

Figure 1.8. Wdr72$^{-/-}$ ameloblast cells have decreased intracellular amelogenin proteins at the early maturation-stage of enamel formation, with no change in transcript levels. Representative images of ameloblasts from P10 male *Wdr72*$^{+/+}$ and *Wdr72*$^{-/-}$ mice immunostained with amelogenin antibody (red) and counterstained with methyl green. Amelogenin is immunoreactive in secretory ameloblasts at the Tomes' processes (A, B) and in early maturation-stage ameloblasts at the center and apical regions in small puncta (C, D), but was more reactive in *Wdr72*$^{+/+}$ than *Wdr72*$^{-/-}$ mice. As enamel formation progressed to mid-maturation, intracellular amelogenin immunostaining was absent in both *Wdr72*$^{+/+}$ (E*)* and *Wdr72*$^{-/-}$ (F) ameloblasts. am, ameloblast; es, enamel space; pl, papillary layer. Scale bar, 10 μm. (G) Relative amelogenin mRNA expression in microdissected enamel epithelia from 6-week-old male mice at secretory and maturation stages, showing no significant differences between *Wdr72*$^{+/+}$ and *Wdr72*$^{-/-}$ mice at either secretory (P = 0.81) or maturation stages (P = 0.53). Gene copy numbers are relative to 18S. Error bars represent ± SD of the mean (n = 3).

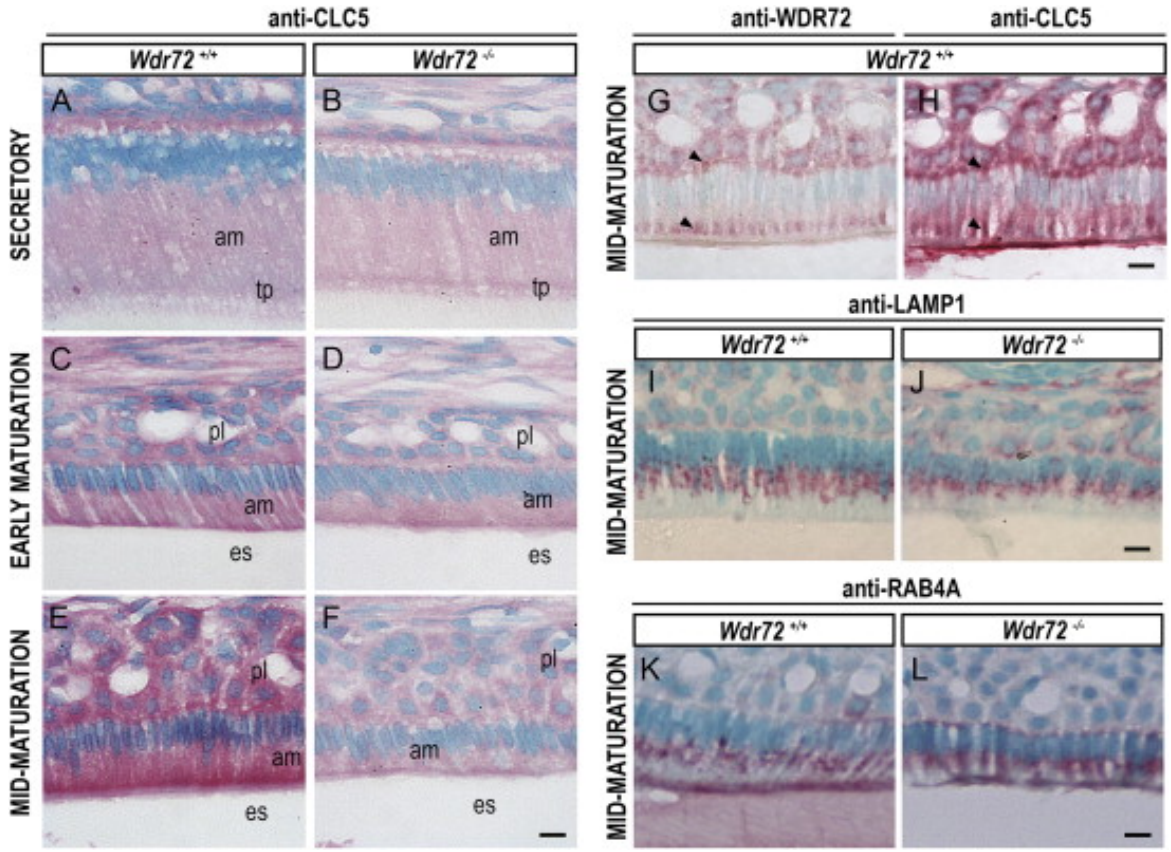

Figure 1.9. Immunolocalization of vesicle markers in Wdr72$^{+/+}$ and Wdr72$^{-/-}$ ameloblasts. Immunostaining of CLC5 in *Wdr72*$^{+/+}$ and *Wdr72*$^{-/-}$ ameloblasts (A–F) showed that CLC5 is decreased in maturation-stage ameloblasts of *Wdr72*$^{-/-}$ mice as compared to *Wdr72*$^{+/+}$. Serial sections of *Wdr72*$^{+/+}$ enamel organs at maturation stage showed WDR72 and CLC5 both immunolocalizing in similar patterns at apical and basal regions of the ameloblasts, as well as the papillary layer (G & H, arrowheads). Further immunostaining of LAMP1 (I, J) and RAB4A (K, L) showed no differences between *Wdr72*$^{+/+}$ and *Wdr72*$^{-/-}$ maturation-stage ameloblasts. am, ameloblast; es, enamel space; pl, papillary layer; tp, Tomes' process. Scale bars, 10 μm.

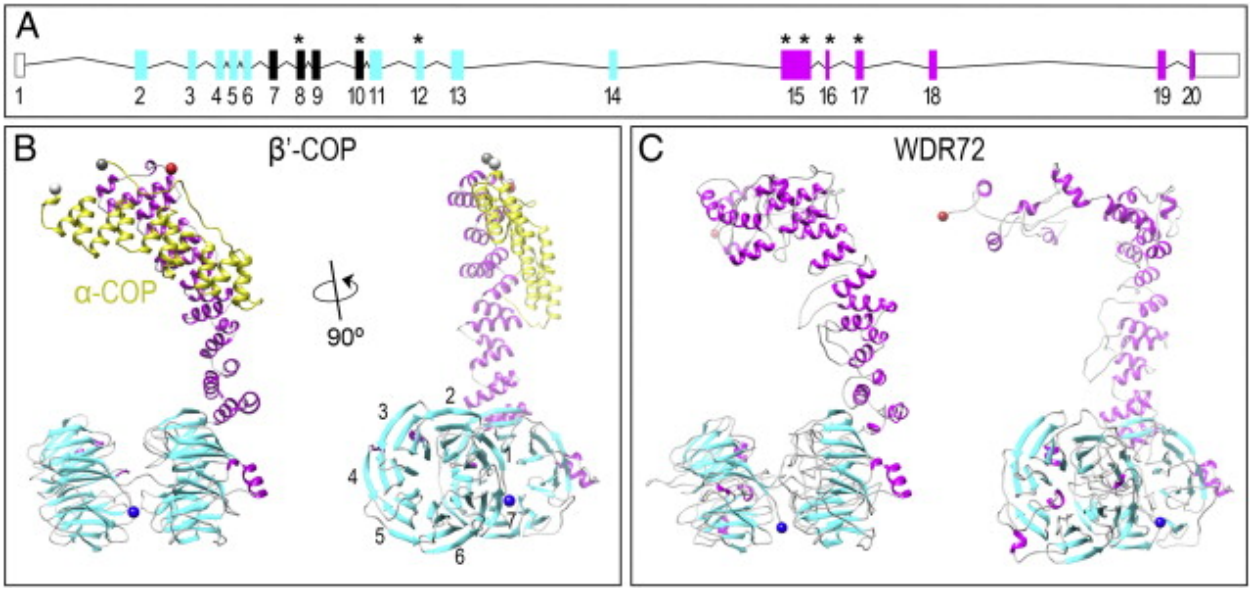

Figure 1.10. WDR72 adopts the β-propeller and α-solenoid fold configuration characteristic of membrane-deformation complexes.
(A) The human *Wdr72* gene with predicted WD40 domains (cyan boxes) and sequence homology divergence to all other human genes (magenta boxes). Reported mutations associated with Amelogenesis Imperfecta are denoted with an asterisk (*), showing our identified exon 8 mutation in between two clusters of WD40 repeat domains (ENST00000360509). Mutation positions based on CCDC 10151.1; numbered box, *Wdr72* exon; line, intron; empty box, untranslated region (UTR). (B) Monomeric structure of β′-COP protein interacting with the C-terminus of α-COP (yellow), another subunit of the crystallized Saccharomyces cerevisiae COPI triskelion vesicle coat complex (PDB identifier: 3mkq). The side view of β′-COP (right) depicts what is referred to as a β-propeller structure (cyan) and an α-solenoid tail (magenta) unique to proteins that interact with curved lipid bilayers. This β′-COP structure was used as a template for model building, as it showed the greatest similarity to WDR72 compared to any other solved protein structures. Numbers represent blades #1–7 that comprise a single β-propeller. (C) constructed model of WDR72 showing two β-propeller domains and a curved α-solenoid tail. The side view of full-length WDR72 (right) depicts two β-propellers, each with 7 blades (cyan), and a series of α-helices (magenta) forming an α-solenoid tail. Blue sphere, N-terminus; red sphere, C-terminus.

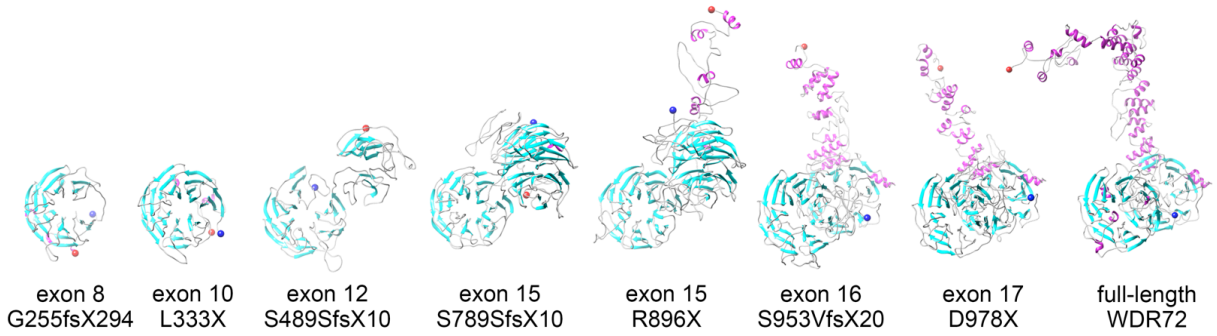

Figure 1.11. Human WDR72 variants expressing known mutations associated with AI.
The spectrum of truncated WDR72 protein models showing differences among reported *Wdr72* mutations and their affected domain configurations. The full-length WDR72 (right) contains two 7-bladed β-propellers (cyan) with an α-solenoid tail (magenta). Our identified exon 8 mutation and the previously reported exon 10 mutation showed the most dramatic fold predictions of WDR72, with a single beta-propeller containing only 6 beta-sheet blades. These are the only two mutations in WDR72 to report additional effects in AI patients, aside from enamel hypomaturation phenotypes and may explain specific sub-structure functions of WDR72. All other predicted structures show a disrupted α-solenoid domain, suggesting this region to be necessary region for proper enamel formation. Blue sphere, N-terminus; Red sphere, C-terminus.

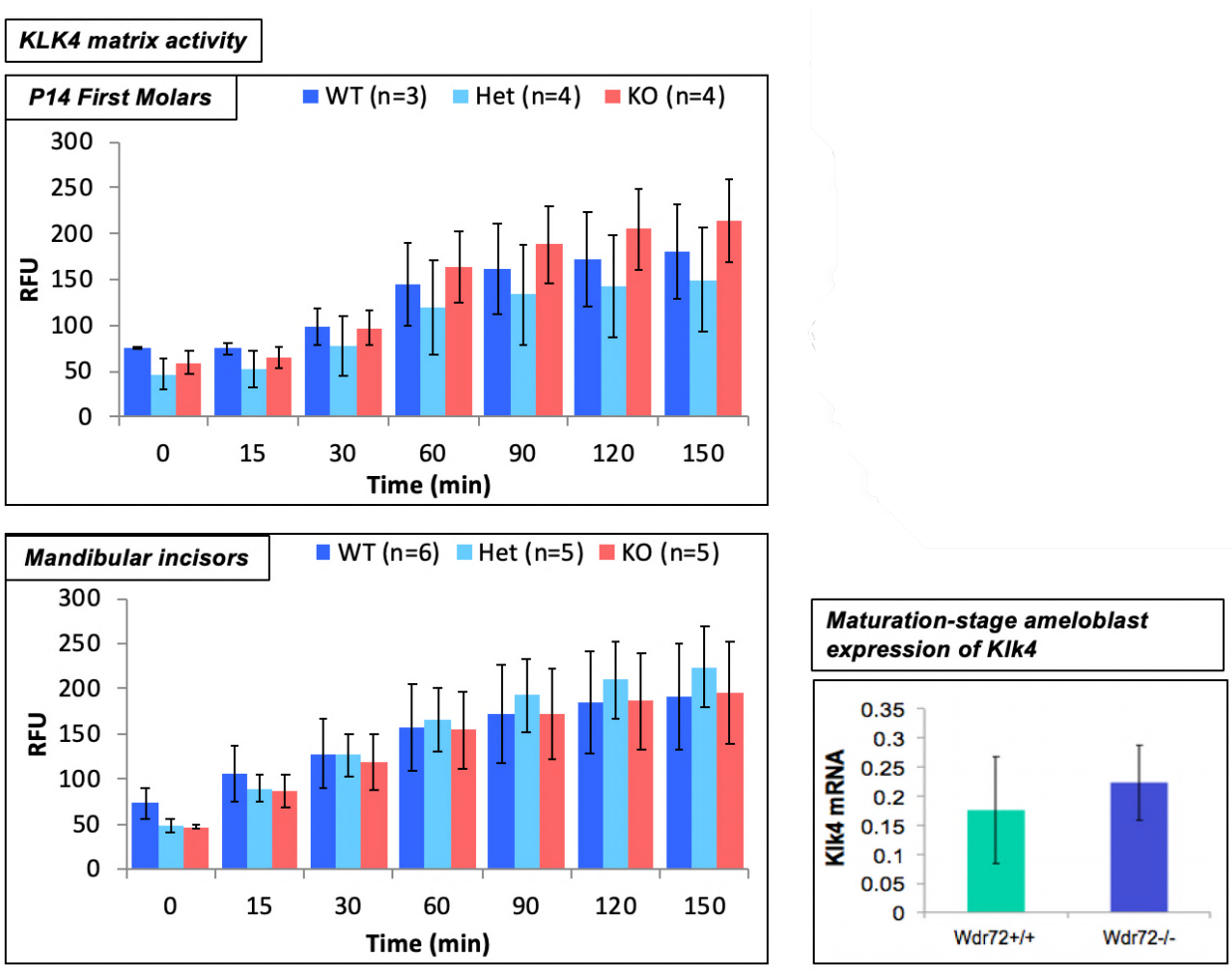

Figure 2.1. KLK4 activity in the enamel matrix and Klk4 mRNA expression do not differ in $Wdr72^{+/+}$, $Wdr72^{+/-}$ *and* $Wdr72^{-/-}$ *mice.*
Left panels measure relative fluorescence units (RFU) of KLK4 proteolytic activity from 0 to 150 minutes in isolated enamel matrices of $Wdr72^{+/+}$, $Wdr72^{+/-}$, and $Wdr72^{-/-}$ first molars at postnatal day 14 (P14) (top panel) or mandibular incisors (bottom panel). KLK4 proteolytic activity shows no significant difference between $Wdr72^{+/+}$, $Wdr72^{+/-}$, and $Wdr72^{-/-}$ ameloblasts. Error bars represent ± SD of the mean. The right panel represents the relative quantitative real-time PCR (qPCR) of micro-dissected maturation-stage ameloblasts from first molars. *Klk4* transcript shows no significant difference between $Wdr72^{+/+}$ and $Wdr72^{-/-}$ (n = 3, $P > 0.10$). Error bars represent ± SD of the mean.

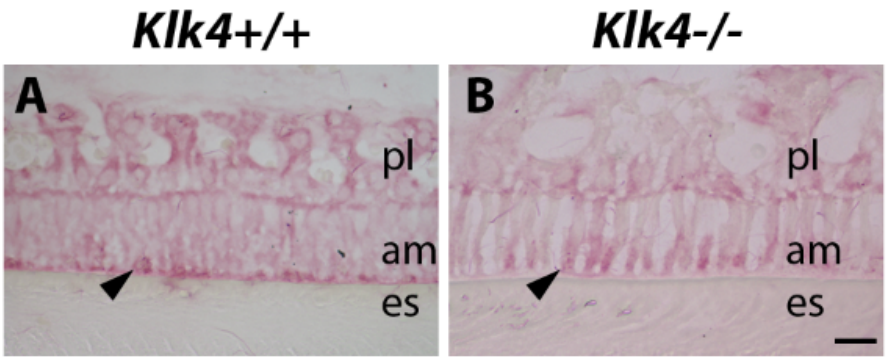

Figure 2.2. Klk4$^{-/-}$ mice show no difference in WDR72 presence or localization.
Representative images of ameloblasts from adult *Klk4*$^{+/+}$ and *Klk4*$^{-/-}$ mice immunostained with WDR72 antibody (red). WDR72 is immunoreactive in maturation-stage ameloblasts at the apical border in both *Klk4*$^{+/+}$ and *Klk4*$^{-/-}$ mice (A, B). ameloblasts. am, ameloblast; es, enamel space; pl, papillary layer. Scale bar, 10 μm.

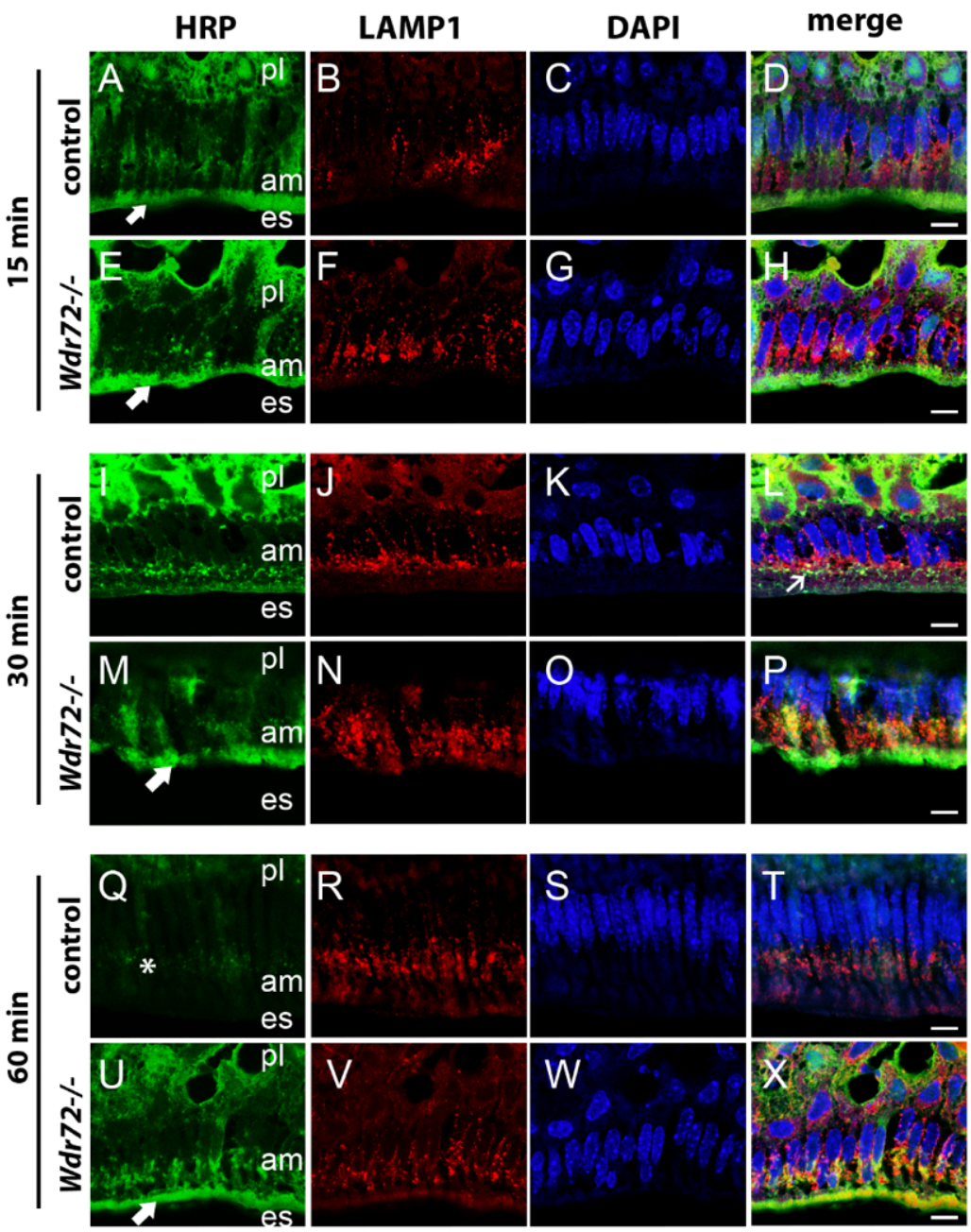

Figure 2.3. Tracer experiment of injected horseradish peroxidase (HRP) and immunolocalization of LAMP1 in control and Wdr72$^{-/-}$ ameloblasts.
Fifteen minutes following HRP injection, HRP localizes to *Wdr72*$^{+/+}$ and *Wdr72*$^{-/-}$ ameloblasts at the apical border during maturation stage. After 30 minutes, control mice show HRP co-localizing with LAMP1 positive vesicles, whereas *Wdr72*$^{-/-}$ ameloblasts retain HRP at the apical border. Sixty minutes following, controls show lack of HRP presence, whereas *Wdr72*$^{-/-}$ ameloblasts show delayed movement towards LAMP1 positive vesicles as well as retention at the apical border.

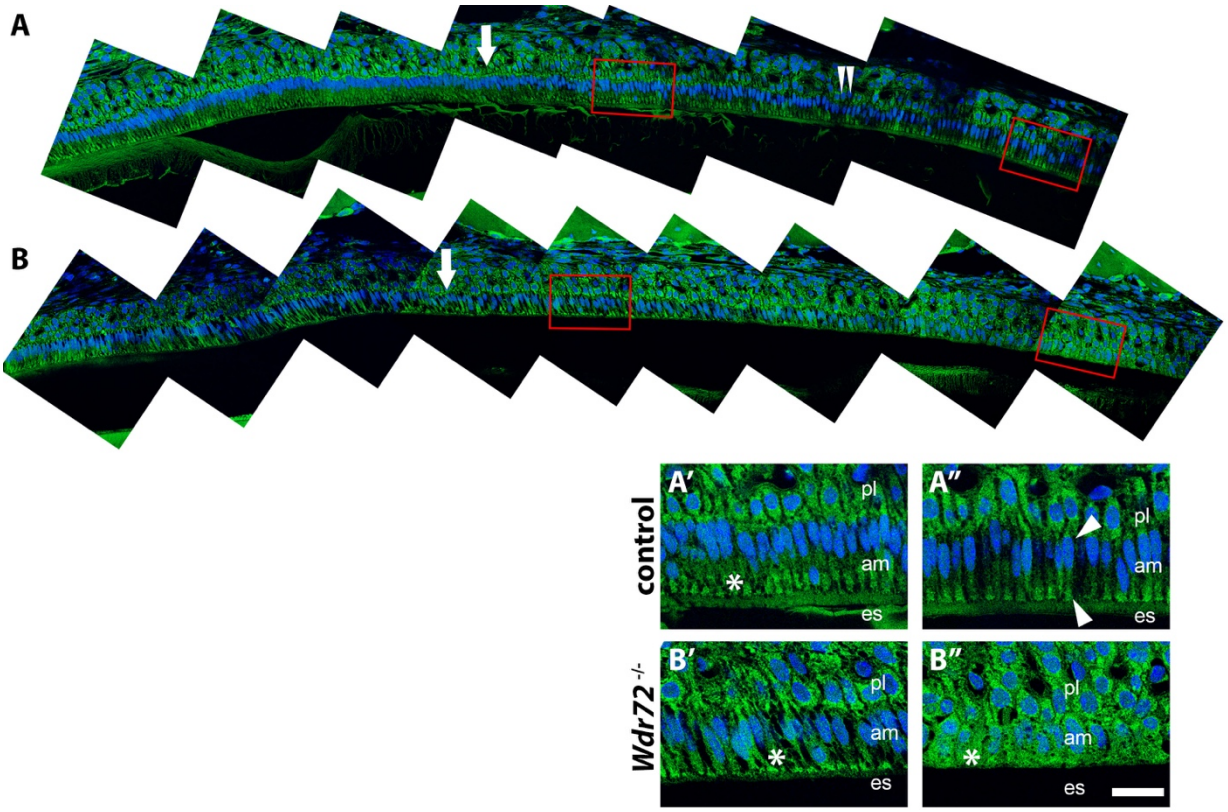

Figure 2.3. Immunolocalization of clathrin heavy chain shows disruption during the maturation stage in Wdr72$^{-/-}$ ameloblasts.
Representative sagittal sections of control (*Wdr72*$^{+/+}$ or *Wdr72*$^{+/-}$) and *Wdr72*$^{-/-}$ mandibles immunostained with a polyclonal rabbit antibody to clathrin heavy chain. Red boxes are the enlarged in the panels below. Arrow denotes onset of maturation stage; double arrowhead marks RA1. (A', A") In control mice, immunoreactivity (green) was diffusely present throughout the cell with a strong apical presence at the onset of maturation stage (asterisk). During periods of ruffle-ended ameloblasts, immunolocalization of clathrin occurs in vesicle-like structures at the basal and apical ends during (arrowheads). (B', B") In the *Wdr72*$^{-/-}$ mice, immunoreactivity initially began with similar vesicle-like structures after the onset of maturation, however, diffuse immunoreactivity (asterisk) was present in *Wdr72*$^{-/-}$ ameloblasts. am, ameloblast; es, enamel space; pl, papillary layer. Scale bar, 10 μm.

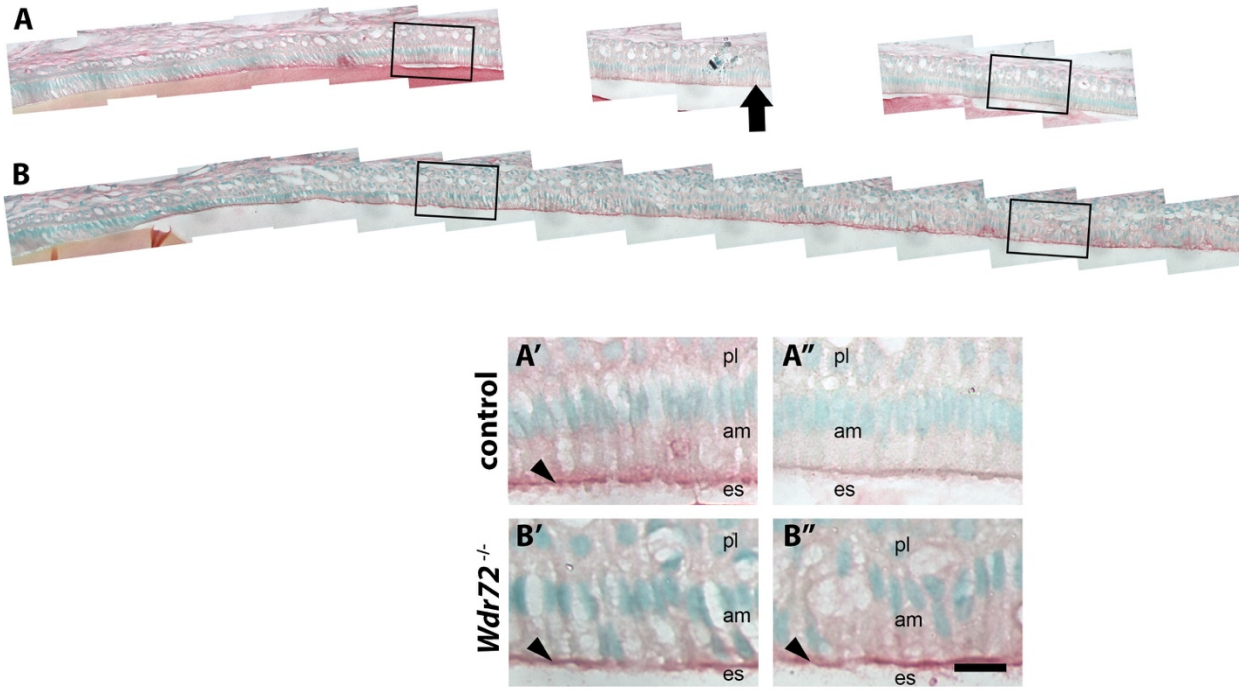

Figure 2.4. Immunolocalization of dynamin II in control and Wdr72$^{-/-}$ ameloblasts. Representative sagittal sections of adult *Wdr72*$^{+/+}$, *Wdr72*$^{+/-}$, and *Wdr72*$^{-/-}$ mandibles were immunostained with a polyclonal antibody to Dynamin II. Black boxes are the enlarged in the panels below; black arrow denotes onset of maturation stage. (A', A") In control (*Wdr72*$^{+/+}$ and *Wdr72*$^{+/-}$) mice, immunoreactivity (red) was initially localized to the apical border of maturation-stage ameloblasts that became absent and then increased later into the maturation stage. (B', B") *Wdr72*$^{-/-}$ mice, however, showed apical staining (arrowheads) throughout the maturation stage without any cycling pattern. am, ameloblast; es, enamel space; pl, papillary layer. Scale bar, 10 μm.

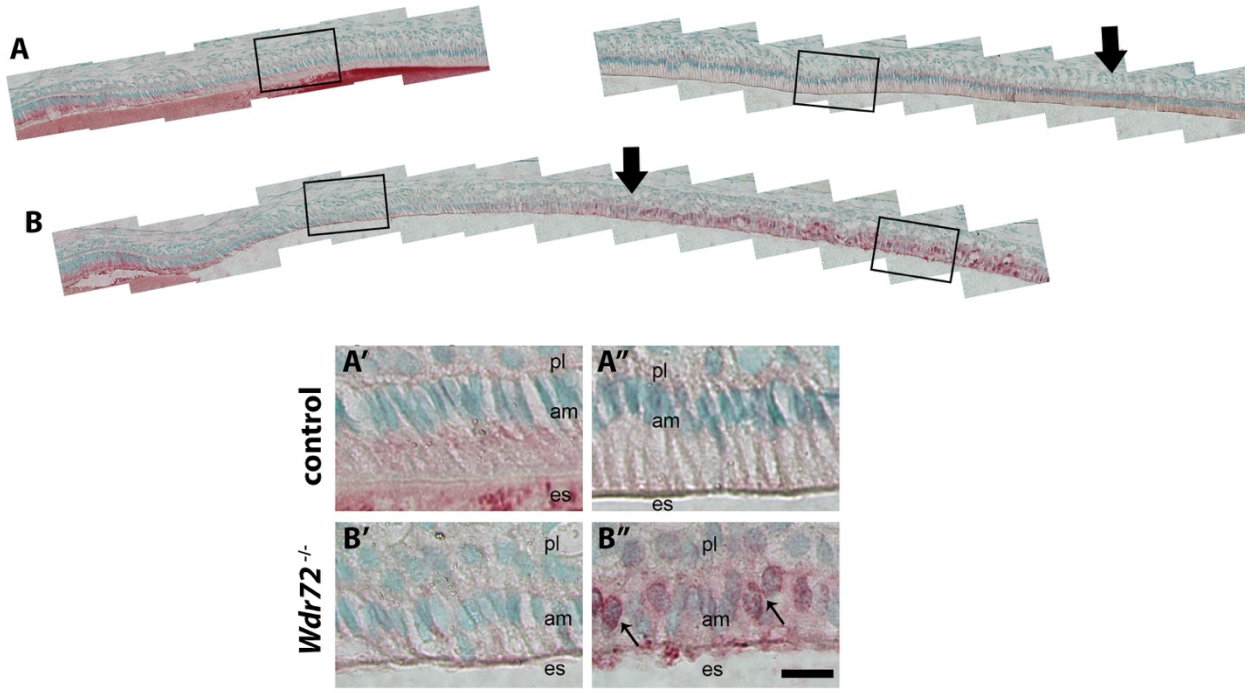

Figure 2.7. Immunolocalization of ANXA8 in control and Wdr72$^{-/-}$ ameloblasts. Representative sagittal sections of control (*Wdr72*$^{+/+}$ and *Wdr72*$^{+/-}$) and *Wdr72*$^{-/-}$ mandibles were immunostained with a polyclonal rabbit antibody to annexin A8 (ANXA8). Black boxes are the enlarged in the panels below; black arrows show the differing onsets of ANXA8 expression in (A) control and (B) *Wdr72*$^{-/-}$ maturation-stage ameloblasts. (A', A") In control (*Wdr72*$^{+/+}$ and *Wdr72*$^{+/-}$) mice, immunoreactivity (red) was initially localized to the subnuclear region of transition ameloblasts and does not increase at the apical border until later in the maturation stage. (B', B") *Wdr72*$^{-/-}$ mice, however, showed diffuse staining shortly after the onset of maturation stage and localizes around the nucleus (arrows). am, ameloblast; es, enamel space; pl, papillary layer. Scale bar, 10 μm.

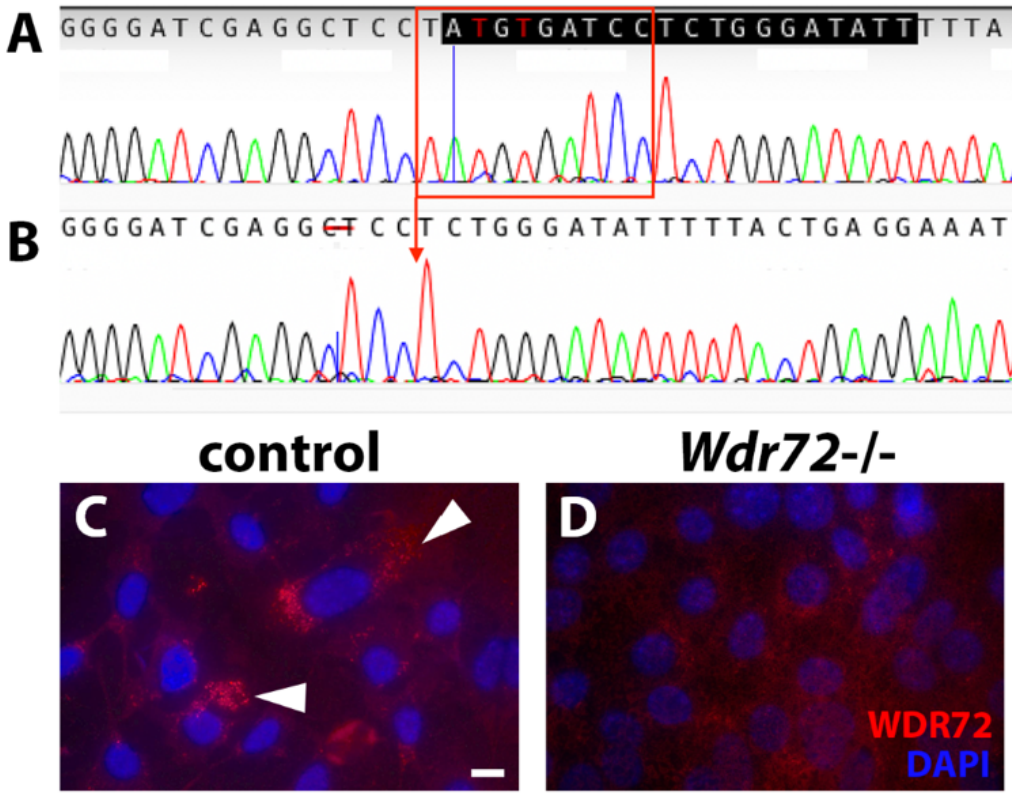

Figure 3.1. CRISPR/Cas9 deletion of Wdr72 gene in ameloblast-like cells (ALCs). Chromatograms of (A) control and (B) *Wdr72*$^{-/-}$ clones (E8 & G4) demonstrate a 10-bp deletion (red box) that leads to a frame shift. Immunostaining with a polyclonal WDR72 antibody (red) counterstained with DAPI (blue) illustrate presence of WDR72 in (C) control cells as punctae present in the cytoplasm (arrowheads), whereas immunostaining is absent in (D) *Wdr72*$^{-/-}$ clones. Scale bar, 5μm.

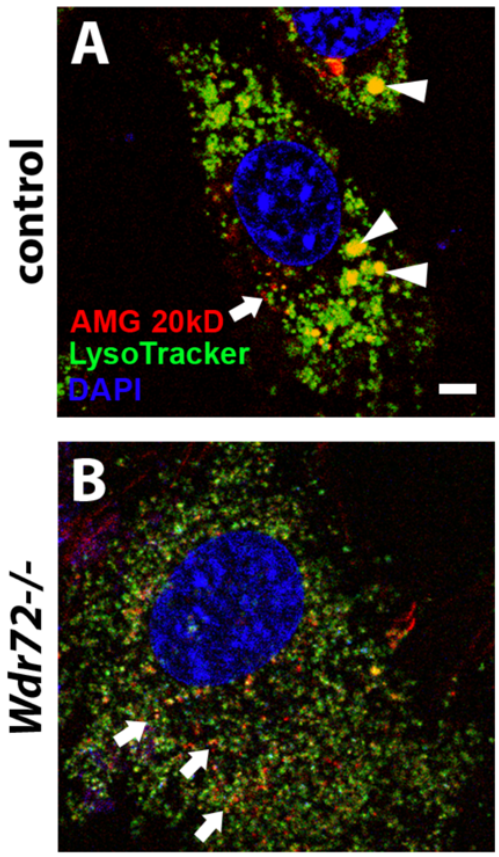

Figure 3.2. Wdr72-deficient ameloblast-like cells (ALCs) are unable to internalize recombinant amelogenin size 20kD (rAMG20) with a distinct LysoTracker pattern.
(A) In control cells, rAMG20 is taken up into the cell and co-localizes with large vesicles stained positive with LysoTracker (arrowheads). (B) *Wdr72*$^{-/-}$ cells show rAMG20 internalized into cells (arrows) that do not co-localize with large LysoTracker-positive vesicles and show numerous small vesicles. Scale bar, 2 μm.

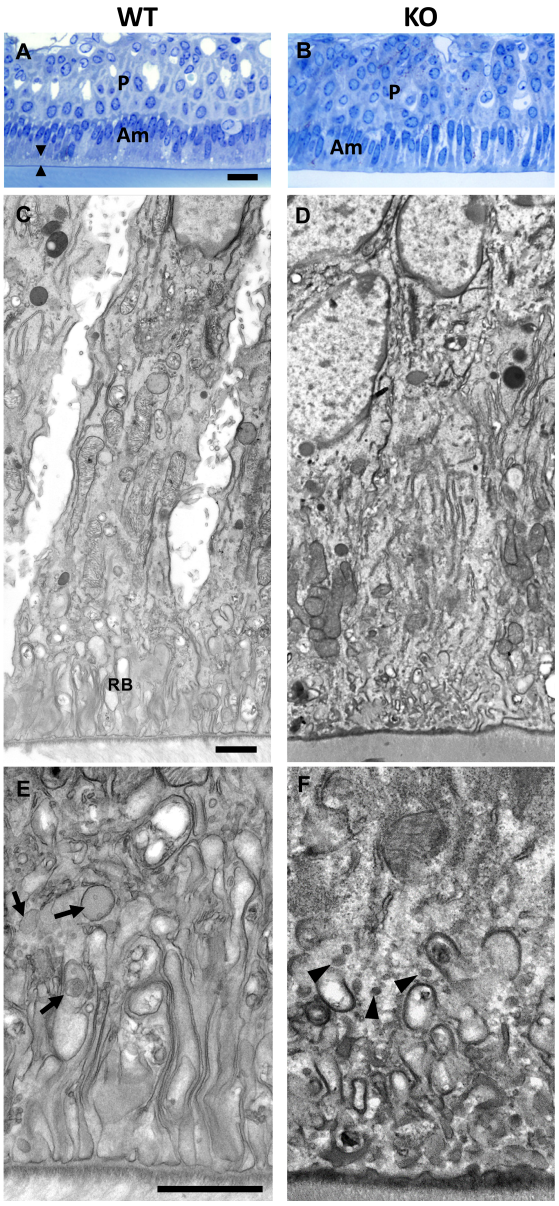

Figure 3.3. Ultrastructure of maturation-stage ameloblasts.
(A & B) Light microscopic observation of the semi-thin sections of maturation ameloblasts immediately after the transition stage confirms the presence of the ruffled border (A, arrowheads) in *Wdr72*$^{+/+}$. In the *Wdr72*$^{-/-}$ section, alignment of the ameloblasts layers is disorganized compared to the *Wdr72*$^{+/+}$, and the ruffled border is not evident (B). P: papillary layer, Am: ameloblasts, Bar: 20 um (C and D) Transmission electron micrographs show highly developed ruffled border (RB) in the *Wdr72*$^{+/+}$ ameloblasts (C). In the *Wdr72*$^{-/-}$ ameloblasts, only some irregular membrane invagination is observed at the distal end of the cells, and the distribution of the cytoplasmic organelles is disorganized (D). Bar: 1µm (E & F) In the distal part of the *Wdr72*$^{+/+}$ ameloblasts, small endocytic vesicles are fused and form larger early endosomes (E, arrows). In the *Wdr72*$^{-/-}$ ameloblasts, small endocytic vesicles do not appear to fuse and do not show formation of larger early endosomes (F, arrowheads). Bar: 1µm.

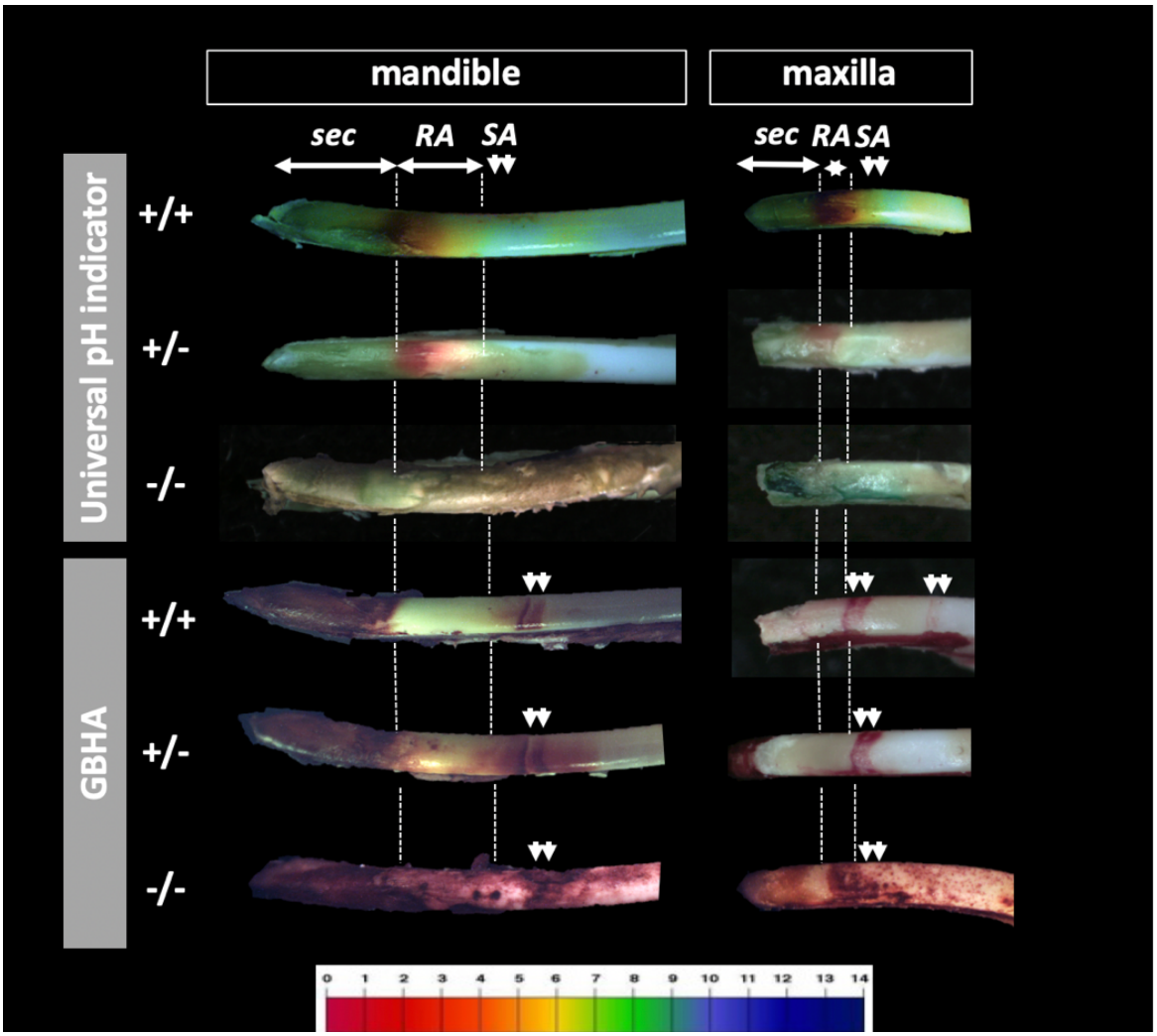

Figure 3.4. Wdr72$^{-/-}$ enamel matrices show defects in matrix acidification and modulation during the maturation stage.
Dissected adult mandibular and maxillary incisors of *Wdr72*$^{+/+}$, *Wdr72*$^{+/-}$, and *Wdr72*$^{-/-}$ mice were incubated in either Universal pH indicator (above) or glyoxal bis (2-hydroxyanil) (GBHA) (below). Dotted lines demarcate the different stages of ameloblast differentiation in enamel formation. Sec, secretory; RA, ruffle-ended ameloblasts; SA, smooth-ended ameloblasts. Double arrows indicate typical banding pattern observed in SA. pH chart at the bottom is provided for reference.

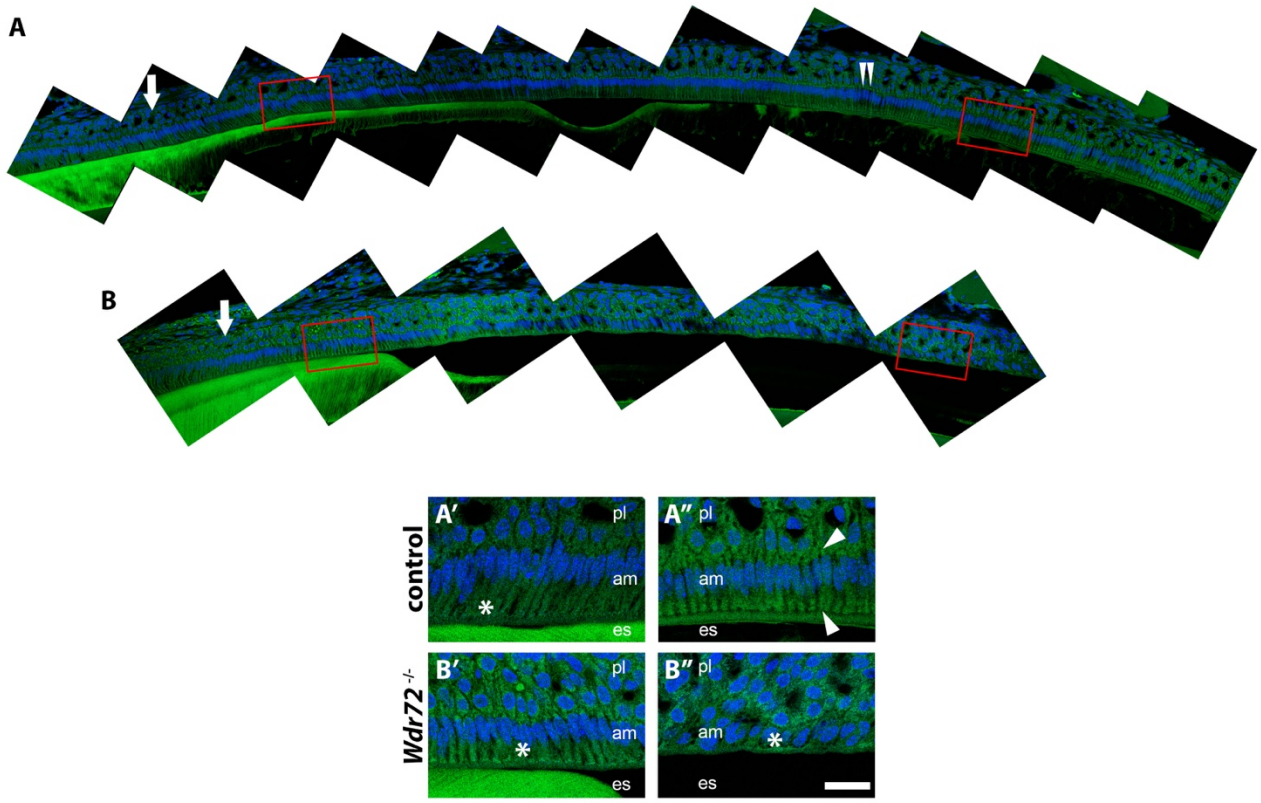

Figure 3.5. Immunohistochemistry of vacuolar-type H^+-ATPase (v-ATPase) in Wdr72$^{-/-}$ mice. *Wdr72*$^{+/+}$ and *Wdr72*$^{+/-}$ mice (controls) demonstrated immuno-positive reactions in a diffuse pattern during smooth-ended ameloblasts (A') and a localized pattern to the apical border during the ruffle-ended ameloblasts (A", arrowheads). Red boxes outline the enlarged images in the panels below; white arrows denote onset of maturation stage; double arrowhead marks RA1. (B' & B") *Wdr72*$^{-/-}$ mice, however, show a trend of diffuse immunoreactivity (asterisk) throughout maturation stage.

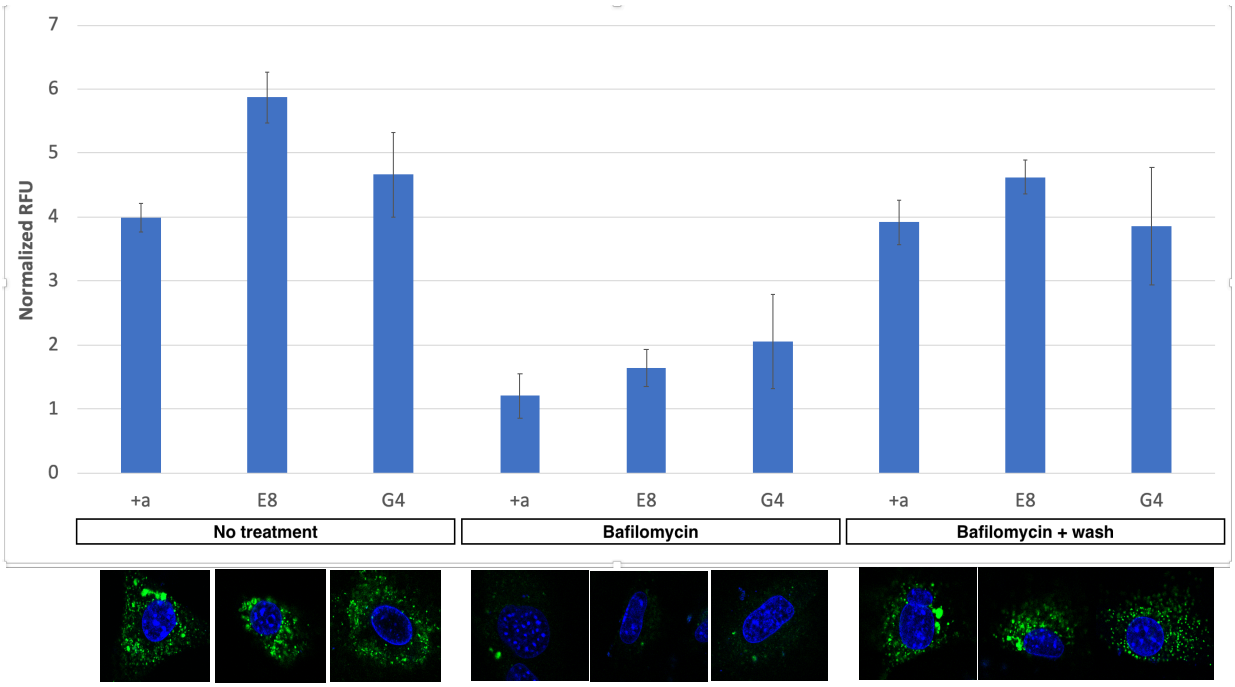

Figure 3.6. Wdr72$^{-/-}$ ameloblast-like cells do not significantly affect v-ATPase-dependent re-acidification of intracellular vesicles during recovery from bafilomycin A1 treatment.
Under steady-state conditions ALCs are readily labeled with lysosomotropic green-fluorescent dye LysoTracker Green as quantified by fluorimetry and visualized by confocal microscopy. After pretreatment with 100nM bafilomycin for 1hr, the number of acidic vesicles and total fluorescent intensity were dramatically reduced in all cases, and all slowly recovered following a 3hr bafilomycin washout. All data are presented as mean values and error bars indicate the standard deviation. n=3, $P > 0.10$.

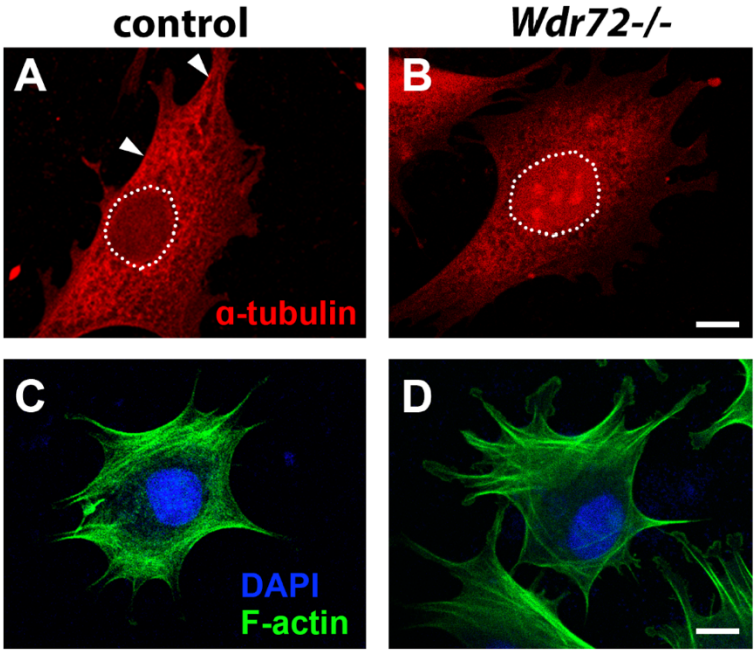

Figure 3.7. Alpha-tubulin is mislocalized in Wdr72$^{-/-}$ ameloblast-like cells (ALCs), whereas F-actin shows no difference.
Confocal microscopy images of control mice show alpha-tubulin (red) localizing intracellulary in an organized, web-like pattern in the cytoplasm of control cells (A), showing organized focal points at the border of cells (arrowheads). (B) *Wdr72*$^{-/-}$ cells, however, exhibit diffuse intracellular staining and localization to the nucleus (white dotted outline) without organized aggregates at the cell border. In contrast, F-actin (green) shows typical web-like striations throughout the cell that organize around the nucleus (blue) in both (C) control and (D) *Wdr72*$^{-/-}$ cells.

TABLES

Table 1. Primers used to target candidate genes in family with amelogenesis imperfecta. Forward (F) and reverse (R) primer pair sequences, annealing temperatures (T_a), and amplicon sizes (bp) that were used for standard PCR and DNA sequencing to identify mutations in candidate genes.

Exon	Gene	Primer Sequence (5'□3')	T_a (ºC)	Size (bp)
1	*Ambn*	F: ATTGCAGGAGCAGAGATTCC	56	395
1	*Ambn*	R: TGGGTGTTAGGCATGTCATC		
2	*Ambn*	F: CCTTTATCCCGGTGGTTTTT	53	365
2	*Ambn*	R: CGCTTTTGGATTGCAAGACT		
3	*Ambn*	F: CTTCTTCATTCTGCCCAAGC	56	385
3	*Ambn*	R: TGCAGTAGAATTATAAGACAAAGCTC		
4	*Ambn*	F: TCCACCTTTCAGTGATGATTTG	52	376
4	*Ambn*	R: TTGTTTTTGTTTTTCCCTGTCA		
5	*Ambn*	F: CTGGCGACAGAGCAAGATTC	54	370
5	*Ambn*	R: TCGATTTATTTGGCACGAGA		
6	*Ambn*	F: TCCTAGCCTCCCTTCCAGAT	56	452
6	*Ambn*	R: TTATGCCTGAAGGCTACGATT		
7-9	*Ambn*	F: TTGGGTCATACCTCCCAAAA	53	670
7-9	*Ambn*	R: TCATGGATAAATGGGACAATGA		
10-12	*Ambn*	F: TGGGTTCCTTTGTTCTCTTAAA	53	898
10-12	*Ambn*	R: TTGGCTACATTCATGGCAGA		
13	*Ambn*	F: CAGCCAACTTCCTATTCTCCA	54	842
13	*Ambn*	R: AAAGCAAGAAGGGGACCTACA		
2	*Amelx*	F: TGGAGCATTCATTACATCCAT	55	216
2	*Amelx*	R: CCCTAATTTCACCAACTATGAGC		
3	*Amelx*	F: TCCTTTAATGTGAACAATTGCAT	55	199
3	*Amelx*	R: AACGCAAACAATGGTCAAAA		
4-5	*Amelx*	F: CCCAACAAATTTTTACCTTCTTC	53	299
4-5	*Amelx*	R: TGTGGAGTAGACATGATATTTCACTTA		
6	*Amelx*	F: TCACCTGAGCCAATGGTAAA	55	499
6	*Amelx*	R: TGCATTGTAGTGGCTTCAAAA		
7	*Amelx*	F: AAGCAGTCCTCATGGACACC	55	372
7	*Amelx*	R: TTAAGTTTCATTCAACACAAAGACA		
1	*Amtn*	F: CTGCAGCTAATAACCCACCTAATGA	55	636
1	*Amtn*	R: AATTGACCTTTTACCACGATGGA		
2	*Amtn*	F: GGGCTGGCATTTTTCCACTCTACAT	56	437
2	*Amtn*	R: TTTTCCCCACTCCCAAACGA		
3	*Amtn*	F: CGAGGCTTCATCTTTATTTACCTTC	58	306
3	*Amtn*	R: CATTTGTGGATATACGCACCC		
4	*Amtn*	F: GCAATAGCCCTTGTAGTCGTAC	58	496
4	*Amtn*	R: GCATGGTCAGTTCTCTGGGTATGTT		
5	*Amtn*	F: GGCATAGTAGCAGGCAACTGT	58	358
5	*Amtn*	R: ACAAAGTACATTGGAAACCTCACAA		
6	*Amtn*	F: ATAGATCATAAGGCAGTTTAACATATT	54	373
6	*Amtn*	R: TAGAAAAGTAGCTGGAGAAGTATAATG		
7	*Amtn*	F: CTCCATCTTTCCATTCCTACCCA	56	572
7	*Amtn*	R: GAGTAAAAATATTCCCTCATGTTGCT		
8	*Amtn*	F: CTAAAGAATGATATGGATGCTCCTAAT	56	567

Exon	Gene	Primer Sequence (5'□3')	T_a (ºC)	Size (bp)
8	*Amtn*	R: GAGACCAGAATTTGTCTTCACATTGC		
3	*Enam*	F: TGTCAACATCGCCCTAGAA	55	595
3	*Enam*	R: GGATGACTGAGATCCCTTCC		
4-5	*Enam*	F: TCCATACTCTCCTTGACAGACA	54	400
4-5	*Enam*	R: TTCTCCTTTTTAGTAAATGTGTAGGAT		
6	*Enam*	F; TCAAGCATAAGTAGGAAAAGGTGA	55	377
6	*Enam*	R: TGTGAGAGGATAGGGGCAAT		
7	*Enam*	F: GAGACAGCCTGAATCACAGC	58	361
7	*Enam*	R: CGAGGCCATTTACAGATATGG		
8	*Enam*	F: GATTGGAATCCTGGCTTCAG	61	552
8	*Enam*	R: TGCACTGGTTTTGTTTCATACC		
9	*Enam*	F: AATGGCGGCATCGAACGTGG	56	155
9	*Enam*	R: TGGATTGTAATTTCTAGTGGAG		
10a	*Enam*	F: AACACCATGGTGGGAAACAAAG	58	573
10a	*Enam*	R: TTACGTTCCCAAGCAAAGAAGTTC		
10b	*Enam*	F: ACAGAATAGGCCTTTTTACAGA	60	787
10b	*Enam*	R: ATATGGGTTATATTCAGGGTAGAA		
10c	*Enam*	F: CAAGAAGAACATTTACCCCATCCT	60	753
10c	*Enam*	R: CATGCCATAGTTCAAATTCTCACC		
10d	*Enam*	F: AGCTGGGCTTCAGAAAAATCCAAT	60	709
10d	*Enam*	R: AGATGGTCTTTGCTGTTGCCTCTC		
10e	*Enam*	F: CTCCAATCCAGAAGGCATCCAA	60	510
10e	*Enam*	R: CTCCACCTGGGTCGCTACTCCTAT		
1	*Klk4*	F: TAACGTCCCAGAGGGAAGAA	57	310
1	*Klk4*	R: GCCATGGGGGACGGATAACA		
2	*Klk4*	F: GGAGCCCTAGGCCTATATCC	55	395
2	*Klk4*	R: CTGAGTCCTTCCGAAGCAAG		
3-4	*Klk4*	F: GTTGCCACAAAACTGACCTG	55	582
3-4	*Klk4*	R: GGCCCTGTGTGTCTCTGTCT		
5	*Klk4*	F: CTTTCTGAGCCCACATCCAT	57	369
5	*Klk4*	R: GGGGATCTGTACCCTTGGTT		
1	*Mmp20*	F: TACCCCATCATCAGGGAGAG	55	468
1	*Mmp20*	R: CCAGACACCAATCTAGGTGGA		
2	*Mmp20*	F: CCCAAAACCAATCATCGTTA	55	594
2	*Mmp20*	R: GCCTGACGGATGGATGTAAA		
3	*Mmp20*	F: TGTTGTTTCATATGCAGAAATTTAAC	52	399
3	*Mmp20*	R: CGAATTAAAGATGTAGAAGGAACAGTA		
4	*Mmp20*	F: TTTTTCAATGGGCTGTTACTCA	53	485
4	*Mmp20*	R: CAACACAATTTGGGGTGGAT		
5	*Mmp20*	F: CACCAAAGCTAAGTGCCAGA	55	468
5	*Mmp20*	R: CAGCTCTTCACAAGAAGGCATAG		
6	*Mmp20*	F: GAAGCTGAGGCTTGCAAAGT	55	490
6	*Mmp20*	R: ACCACCCTTCTGCTGCATAG		
7	*Mmp20*	F: AGGCAAGGCAAGAGCAAAG	55	414
7	*Mmp20*	R: TAGGGTGGCATTTCATACCC		
8	*Mmp20*	F: ACTTTTGCCTCCAGGGAAGT	55	493
8	*Mmp20*	R: TCTGTAAATCGCACCCCAGT		
9	*Mmp20*	F: TGGCACCACTACACTTCAGC	64.5	570
9	*Mmp20*	R: CAAACAAACAAACAAAAACTTTCC		

Exon	Gene	Primer Sequence (5'□3')	T_a (ºC)	Size (bp)
10	*Mmp20*	F: GACAAGCTAACTGCCACCTGA	55	831
10	*Mmp20*	R: AAGTGCCCATCTCTTGCCTA		
2	*Wdr72*	F: TGCTTGTAATATTATCGGTTTCCTC	57	298
2	*Wdr72*	R: GCAAGTTGTCCGTATTTTGTGA		
3	*Wdr72*	F: CAAAAACAACAGAATTTCCTAATCA	54	300
3	*Wdr72*	R: TCCTTCAGCCCTAAAATTGTATTC		
4	*Wdr72*	F: AAAGAAAAACTTGGTGGCACA	51	226
4	*Wdr72*	R: TTTGCAAATGCCCTAAACAA		
5	*Wdr72*	F: GAGAAATCTTCAATGTAGCCAAA	51	345
5	*Wdr72*	R: TTTCTGAATTTCTGCCCAAT		
6	*Wdr72*	F: ACACAGCCCTGCGTAATTCT	51	277
6	*Wdr72*	R: TTTGAACTTTTGACAATAAACATGTAA		
7	*Wdr72*	F: GGAAGCAGGTCTTCTCATGG	57	328
7	*Wdr72*	R: GACACATCATTCCATGTTCTGG		
8	*Wdr72*	F: TGTATCCCCTGAAACCTACCC	58	495
8	*Wdr72*	R: AAGCCTACCAAGCCCAGAGT		
9	*Wdr72*	F: TACAAAACAGCAGGGGATGG	53	483
9	*Wdr72*	R: TTTCTCTTTGGTAGCCATTGAT		
10	*Wdr72*	F: AAAACAGTGGCCATCTCTCTCTA	57	298
10	*Wdr72*	R: TCCCATGCTGCTCAACTTAG		
11	*Wdr72*	F: GGGAGGGTGCCTTGATATTT	56	400
11	*Wdr72*	R: TCTTGTTTAGTGCAGTCTGTTGAA		
12	*Wdr72*	F: GAAGAGAATCTTGGGACGATTT	54	392
12	*Wdr72*	R: TTTTCTTTGGAAATATGGGTCA		
13	*Wdr72*	F: AAATGGGGCTTTAACAAAACTT	52	398
13	*Wdr72*	R: CATCACCGTGTCTTCTCTGAA		
14	*Wdr72*	F: TTGCAAGATACTAAGGCACGA	57	385
14	*Wdr72*	R: TGCATATAACTTCTTATTCGGTTGA		
15a	*Wdr72*	F: CCTTTAGCTGCTCTGCAATG	51	500
15a	*Wdr72*	R: TTGATGGCTTAGGCTGCAT		
15b	*Wdr72*	F: CCTCTTTCAGCAGAGGCACT	59	682
15b	*Wdr72*	R: CCCACTGGAAAGAAGGAAGG		
16	*Wdr72*	F: TGGTCATGTACCCATATCTTTGA	54	267
16	*Wdr72*	R: TGACACTGCTAACCAGTTATAGAAAGA		
17	*Wdr72*	F: ACAAAGCTTCCCAGGTGATT	54	300
17	*Wdr72*	R: TTCAAAGGCCATTTTATGAGG		
18	*Wdr72*	F: ATTTAAATTCCGGGCTTTGG	51	380
18	*Wdr72*	R: AATCGAAAATCGTTCAGTTGC		
19	*Wdr72*	F: TGGAACTGAAAGGAAATGTTTTA	51	300
19	*Wdr72*	R: GAAAACAGCATTACAATGTCCTC		
20	*Wdr72*	F: CTCCCCTCCTCTTGGTCTTT	49	199
20	*Wdr72*	R: AAACAAATGGCATCTTTTGGA		

Table 2. SNPs associated with candidate genes

Reference SNP data of sequenced candidate genes from a family with autosomal recessive amelogenesis imperfecta with the identified exon 8 mutation in *Wdr72* (c.806_810delGGCAG). IV5 & IV6, carriers; V1& V2, unaffected; V3-V5, affected. Plus sign (+), major allele; Minus sign (-), minor allele.

Gene	Chr. Loc.	Ref. SNP	RefSeqGene	IV5	IV6	V1	V2	V3	V4	V5
Ambn	4q21	rs3924573	NC_000004.11	+/-	+/+	+/-	+/+	+/+	+/-	+/-
Ambn	4q21	rs71599963		+/-	+/+	+/-	+/+	+/+	+/-	+/-
Ambn	4q21	rs35266919		+/-	+/+	+/-	+/+	+/+	+/-	+/-
Amtn	4q13.3	rs35692424	NC_000004.11	+/+	+/-	+/-	+/+	+/+	+/-	+/-
Amtn	4q13.3	rs7660807		+/-	+/-	+/+	-/-	-/-	+/+	+/+
Amtn	4q13.3	rs3912755		+/-	+/+	+/-	+/+	+/+	+/-	+/-
Amtn	4q13.3	rs17733287		+/+	+/-	+/-	+/+	+/+	+/-	+/-
Amtn	4q13.3	rs201205218		+/-	+/+	+/+	+/-	+/-	+/+	+/+
Amtn	4q13.3	rs17676820		+/+	+/-	+/-	+/+	+/+	+/-	+/-
Enam	4q13.3	rs3796703	NG_013024.1	+/+	+/-	+/+	+/-	+/-	+/+	+/+
Klk4	19q13.41	rs2978642	NG_012154.1	+/-	+/-	+/+	-/-	+/+	+/-	+/-
Klk4	19q13.41	rs73042387		+/+	+/-	+/+	+/-	+/+	+/-	+/-
Mmp20	11q22.3	rs2245803	NG_012151.1	-/-	-/-	-/-	-/-	-/-	-/-	-/-
Mmp20	11q22.3	rs1784423		-/-	-/-	-/-	-/-	-/-	-/-	-/-
Mmp20	11q22.3	rs1784424		-/-	-/-	-/-	-/-	-/-	-/-	-/-
Mmp20	11q22.3	rs1940054		+/-	+/+	+/-	+/+	+/-	+/-	+/-
Mmp20	11q22.3	rs7934921		+/-	+/+	+/-	+/+	+/-	+/-	+/-
Wdr72	15q21.3	rs690337	NG_017034.1	+/-	-/-	+/-	+/-	-/-	-/-	-/-
Wdr72	15q21.3	rs551225		+/+	+/-	+/-	+/-	+/+	+/+	+/+
Wdr72	15q21.3	rs552960		+/-	+/+	+/-	+/-	+/+	+/+	+/+
Wdr72	15q21.3	rs6416452		-/-	+/-	+/-	+/-	-/-	-/-	-/-
Wdr72	15q21.3	rs74018741		+/-	+/-	+/+	+/+	-/-	-/-	-/-
Wdr72	15q21.3	rs78493456		+/-	+/-	+/+	+/+	-/-	-/-	-/-

MATERIALS AND METHODS

Mutation screening

A consanguineous family exhibiting hypomature phenotypes of autosomal recessive inheritance Amelogenesis Imperfecta (AI) was examined at the UCSF pediatric dental clinic and screened for mutations using a candidate gene approach. DNA samples of the probands and all immediate family members were obtained using Oragene®DNA sample collection kit (DNA Genotek, Inc., Ontario, Canada) with approval by the UCSF Committee on Human Research. Forward and reverse primers were designed within introns to flank coding regions and potential splice sites in ameloblastin (*Ambn*), amelogenin (*AmelX*), amelotin (*Amtn*), enamelin (*Enam*), kallekrein-related peptidase 4 (*Klk4*), matrix metalloproteinase-20 (*Mmp20*), and WD repeat-containing protein 72 (*Wdr72*) (**Table 1**). Polymerase chain-reaction (PCR) amplifications of these candidate genes were performed using taq polymerase (Invitrogen, Carlsbad, CA), and sequencing was conducted at Elim Biopharmaceuticals (Hayward, CA). DNA sequence assemblies and SNP analyses (**Table 2**) were performed and documented with CodonCode Aligner software (Centerville, MA).

Protein structure modeling

The WDR72 sequence was downloaded with accession identifier Q3MJ13 from the UniProt knowledgebase. To generate atomic models for WDR72 wild type and mutant structures, we applied the iterative threading assembler (I-TASSER) [43] and the restraint-based comparative modeling program MODELLER-v9.10 [129] with alignments generated by the profile alignment homology alignment algorithm HHpred [45]. Models were generated with the automated modeling pipelines accessible through the I-TASSER webserver (http://zhanglab.ccmb.med.umich.edu/I-TASSER/) [43,44] and the bioinformatics toolkit (http://toolkit.tuebingen.mpg.de/hhpred) [45]; respectively. These two pipelines model diverse crystallized proteins with an average structural

alignment GDT-TS measure (range 0–100) [130] of 70 in blinded assessments, outperforming all other automated protein structure prediction tools [131]. To verify double seven-bladed β propeller fold topology for WDR72, we applied the β-propeller blade structural motif algorithm SMURF [48].

WDR72 oligomer models were generated with the multi-scale modeling and structural comparison tools in Chimera [132] by comparison of monomer models to crystallographic structures of structurally homologous protein oligomers found by HHpred.

Knockout mouse generation

The *Wdr72* knockout mouse strain used in this study was created from an ES cell clone (EPD0085_5_D06) generated by the Welcome Trust Sanger Institute and injected into a pregnant female mouse blastocyst by the KOMP Repository and the Mouse Biology Program at the University of California, Davis. The *Wdr72* mutant allele (*Wdr72*$^{-}$) was created using a 'knockout first conditional ready' approach using previously published methods [41], generating a functional knockout through splicing in *LacZ* gene reporter and Neomycin (*Neo*) selection cassettes (**Fig. 1.2A**). The targeting vector incorporated an En2 splice acceptor (SA) and internal ribosome entry site (IRES) upstream of *LacZ,* followed by a polyadenylation (pA) signal. A *loxP* site separated the *LacZ* cassette from the subsequent *Neo* resistance cassette, which was driven by an autonomous promoter (hBactP) and pA signal. Flippase recognition target (*FRT*) sites flanked both *LacZ* and *Neo* cassettes, all of which was inserted between exons 2 and 3. Two additional *loxP* sites were introduced on either side of exon 3. *Wdr72*$^{+/-}$ heterozygous mice (*Wdr72*$^{+/-}$) on a C57BL/6 genetic background were purchased and subsequently bred to generate the knockout (*Wdr72*$^{-/-}$) and wild-type (*Wdr72*$^{+/+}$) mice used in these experiments. Genotypes of mice were determined by standard and quantitative PCR (Transnetyx, Cordova, TN) using genomic DNA obtained from tail biopsies with forward

primers: *NeoF*-GGGATCTCATGCTGGAGTTCTTCG, *F*-TCTTTCACCTAAGCAACACATGCGG, and reverse primer *R*-GAAACCCGGAGATGAAGGAATGTGC. Amplicon sizes of *Wdr72*$^{+}$ and *Wdr72*$^{-}$ alleles were 520 and 633 bp, respectively.

Animal use, husbandry, and genotyping

Mice were bred and housed in accordance with UCSF Institutional Animal Care Committee (IACUC) guidelines. 2–5 mice were housed together on a 12-hr light/dark schedule with constant access to food and water. *Wdr72*$^{-/-}$ mice were generated as described in the previous section. *Wdr72*$^{+/-}$ male and female mice were used to generate breeding pairs, which produced litters of a mixture of *Wdr72*$^{+/+}$, *Wdr72*$^{+/-}$, and *Wdr72*$^{-/-}$ genotypes to be used for experiments. Only mice from the same litter were compared to one another when evaluating similarities and differences.

Micro-computed tomography (microCT)

Mineral density levels of 6-week-old undecalcified *Wdr72*$^{+/+}$ (n = 3) and *Wdr72*$^{-/-}$ (n = 3) murine hemimandibles were scanned and compared by microCT (SkyScan1076; Bruker-microCT, Kontich, Belgium). X-ray source operating settings were set to 50 kV and 160 μA and image reconstitution was carried out with NRecon software (Bruker-microCT). Using Amira software (ver 1.4.1 SkyScan), coronal sections perpendicular to the curve of the incisor and in line with the midsagittal plane of the incisor were selected from 3D reconstructions for quantitative densitometry (g/cm^2) analyses. We compared *Wdr72*$^{+/+}$ and *Wdr72*$^{-/-}$ coronal sections landmarked at either the mesial root of the first molar (maturation stage) or the distal root of the third molar (secretory stage) with indexed and normalized gray scale levels (range 0–255). A region of interest (ie. enamel, dentin or alveolar bone) was selected from each coronal section and quantified for mineral density by measuring the average of relative gray values at each pixel

within the selected region (ImageJ, ver 1.46r). These gray value outputs were then averaged across samples and compared by paired Students' *t*-tests with a statistical significance threshold of $P < 0.05$.

Histology

Dissected *Wdr72*$^{+/+}$, *Wdr72*$^{+/-}$, *Wdr72*$^{-/-}$, *Klk4*$^{+/-}$, and *Klk4*$^{-/-}$ maxillae and mandibles at P10 and adult ages were immediately immerse-fixed in 4% paraformaldehyde (PFA)/0.06 M cacodylate buffer (pH 7.3) overnight and decalcified in 8% EDTA (pH 7.2) for two weeks at 4 °C. Samples were then dehydrated and paraffin-processed for routine embedding and sectioning. Sagittal incisor sections at 5 μm were utilized for standard hematoxylin and eosin (H&E) staining or for immunohistochemistry.

Immunostained tissue sections were deparaffinized and rehydrated, followed by incubation with 10% swine serum for blocking. Primary antibodies targeting WDR72, amelogenin, CLC5, RAB4A, LAMP1, clathrin, Dynamin II, ANXA8, or v-ATPase subunit v0a1 were incubated at 25 °C overnight, followed by a biotinylated secondary antibody (Dako, Carpinteria, CA) at 25 °C for 1 hr. Alkaline phosphatase conjugated to streptavidin (Vector Laboratories Inc., Burlingame, CA) was used to visualize the colorimetric reaction. Sections were then counterstained using methyl green (Dako, Carpinteria, CA).

The polyclonal rabbit anti-WDR72 antibody was synthesized by Genscript (Piscataway, NJ) from a synthetic peptide (CETGTLERHETGERA) as previously described [22], and was used at a 2.7 μg/mL concentration. The rabbit anti-amelogenin antibody (1:500 dilution) was developed in our laboratory as previously described [65,133]. Purchased antibodies and their concentrations used in this study included the following: polyclonal rabbit anti-CLC5 (Novus Biologicals, Littleton, CO) (NBP1-70374) at a 1:800 dilution; polyclonal rabbit anti-RAB4A (Santa Cruz

Biotechnology, Santa Cruz, CA) (sc-312) at 1 µg/mL concentration; polyclonal rabbit anti-v0a1 (Aviva Systems Biology, San Diego, CA) (ARP46581-P050) [117] at 2.5 µg/mL concentration. The monoclonal rat anti-LAMP1 antibody (1D4B; 1 µg/mL concentration) developed by J. Thomas August was obtained from the Developmental Studies Hybridoma Bank under the auspices of the NICHD and maintained by the University of Iowa, Department of Biology (Iowa Cita, IA 52242). Dynamin II (Santa Cruz Biotechnology, CA) (5E4C2F3, sc-81150) mouse monoclonal antibody was used with Vector mouse on mouse (M.O.M.) kit (Vector Laboratories, Inc, Burlingame, CA) (BMK-2202) and visualized using the alkaline phosphatase substrate kit (Vector Laboratories) (SK-5100). Goat polyclonal antibody to clathrin heavy chain (Santa Cruz Biotechnology, CA) (C-20, sc-6579) was used at a concentration of 1µg/mL. Rabbit polyclonal antibody to annexin-A8 (Thermo Fisher Scientific) (PA5-31479) was used at 1:500 dilution. V-ATPase was used at a concentration of 1µg/mL (Aviva) (ARP46581-P050), targeting v_0a_1 subunit, as previously done [112]. For immunofluorescent sections, conjugated primary antibody Qdot 525 FITC streptavidin conjugate (Life Technologies) (Q10143MP) was used and were subsequently counterstained with Hoescht DAPI stain (Invitrogen, H3570) at 1:10,000 dilution.

Negative controls were performed with normal rabbit IgG (Vector Laboratories Inc., Burlingame, CA) (I-1000) at matching concentrations to the experimental diluted primary antibodies. Histological images were taken with a Nikon Eclipse E3800 microscope (Melville, NY) using a digital camera (QImaging Inc., Surrey, Canada) and SimplePCI imaging software version 5.3.1.

KLK4 protease assay

Dissected mandibular and maxillary first molars and incisors containing endogenous KLK4. Proteolytic activity of KLK4 protein from each mouse was analyzed by digestion of a fluorogenic peptide substrate, Boc-V-P-R-AMC (R&D Systems). The SpectraMax iD3 fluorescence plate reader (Molecular Devices) with excitation at 380 nm and emission at 460 nm was used for the

measurement of the enzymatic activity. Fluorescent readouts measuring KLK4 activity were recorded every minute for 150 minutes.

Horseradish peroxidase tracer experiment

Wdr72$^{+/+}$, *Wdr72*$^{+/-}$, and *Wdr72*$^{-/-}$ mice were anesthetized subcutaneously with tribromoethanol to surgically expose the deltopectoral muscle and jugular vein. Seven units (0.7mL) of 5% HRP (Sigma-Aldrich, MO) (P9250-25KU) in 0.9% saline were injected into the jugular vein through the deltopectoral groove at the intersection of the jugular and axillary veins via a 31 gauge needle at a rate of 7 units per minute. 0.9% saline solution was injected into control mice serving as a negative control. Mice were kept under general anesthesia for 15, 30 or 60 minutes, prior to collecting tissue samples. Dissected *Wdr72*$^{+/+}$, *Wdr72*$^{+/-}$, and *Wdr72*$^{-/-}$ maxillae and mandibles were immediately immerse-fixed in 4% paraformaldehyde (PFA)/0.06 M cacodylate buffer (pH 7.3) overnight and decalcified in 8% EDTA (pH 7.2) for two weeks at 4 °C. Samples were then incubated twice in 30% sucrose at 25ºC for 15 minutes, acclimated in optimum cutting temperature (O.C.T.) compound (Tissue-Tek) (Sakura Americas) for 5 minutes, and flash-frozen in hexane and dry ice. Tissue blocks were cryosectioned using a Leica cryostat machine (CM3050 S) at 7µm (CT = -17ºC, OT = -25ºC) and placed on UV CryoJane slides (Leica Microsystems Inc, IL) (39475209). Slides were then exposed to the CryoJane Tape-Transfer system (Leica Microsystems Inc, IL), and stained with TSA Plus fluorescein (Sigma, D5879) stain at 1:100 dilution, LAMP1 antibody (described above) with donkey anti-Rat Alexa 555 (abcam, ab150154) at 1:400 dilution, and counterstained with Hoescht DAPI stain (Invitrogen, H3570) at 1:10,000 dilution. Histological images were taken with an inverted confocal microscope (Leica Microsystems, DMi8) using Leica Application Suite X imaging software under the following settings: 63X, 1024x1024, speed 400, 1.4% DAPI [410-502], 0.2%

488 green [512-541], 1.9% 522 red [587-755]; 900V gain, 0.0% smart offset, 1.00 AV pinhole. All images and z-stacks were then processed using Fiji plug-ins and ImageJ [134–136].

RNA isolation and quantitative real-time PCR from whole tissues

Total RNA was isolated from dissected flash-frozen kidneys and from micro-dissected secretory and maturation-stage ameloblasts of *Wdr72*$^{+/+}$ and *Wdr72*$^{-/-}$ mice at postnatal day 24 using RNeasy Mini kit (QIAGEN, Germantown, MD). Aliquot containing 20 µg of total RNA was reverse transcribed to cDNA using SuperScript® III Reverse Transcriptase and oligo dT primers (Invitrogen, Carlsbad, CA). For kidney samples, polymerase chain reaction amplification for standard PCR was performed with the Hot Start Taq kit (Qiagen) by first incubating the reaction mixture at 95° for 5 min, followed by 94 °C, 57 °C, and 72 °C for 1 min each for 35 cycles and then 72 °C for 10 min. The primers used flanked the exon–exon boundaries surrounding exon 14 of the *Wdr72* transcript (ENST00000360509), targeting the epitope region to where our WDR72 antibody would recognize. Primers were designed using Frodo (http://frodo.wi.mit.edu/primer3/) [137,138]. The products were visualized on a 1.6% agarose gel with SYBR GREEN staining (Invitrogen, Carlsbad, CA). Real-time PCR gene expression was characterized by quantitative PCR using the ABI 7500 system (Applied Biosystems, Carlsbad, CA). cDNA was amplified with the Fast Start SYBR Green master mix (Roche, Indianapolis, IN). Relative expression levels of target genes were analyzed by the delta-Ct method as published previously [139] using GAPDH or 18S as endogenous controls.

For measuring *Klk4* expression, adult mice were euthanized by CO_2 asphyxiation, and dissected whole mandibular incisors or first molars from maxillae and mandibles and placed into Qiazol lysis buffer (Qiagen) (79306) on ice until processed. Samples were then vortexed every 30 seconds over a 5 minute time period at 25ºC. Chloroform was added and samples were again vortexed for 15 seconds and allowed to rest for 2-3 minutes. After centrifugation at 4ºC at

12,000xg for 15 minutes, the clear extract was placed into a new tube containing equal volume of 70% ethanol. Samples were then vortexed immediately for 5 seconds and spun down and the clear extract/ethanol mixture was added to a Qiagen RNA mini column for spin down at 12,000xg. Subsequent steps involved following the Qiagen RNA mini handbook to purify the RNA. Total RNA concentrations were measured using a Nanodrop spectrophotometer (Nanodrop Technologies, ND-1000 C253), and samples were stored in RNAse-free water at -80ºC.

Aliquot containing 20 µg of total RNA was reverse transcribed to cDNA using SuperScript® III Reverse Transcriptase and oligo dT primers (Invitrogen, Carlsbad, CA). Polymerase chain reaction amplification for standard PCR was performed with the Hot Start Taq kit (Qiagen) by first incubating the reaction mixture at 95° for 5 min, followed by 94 °C, 57 °C, and 72 °C for 1 min each for 35 cycles and then 72 °C for 10 min. The primers targeted *Klk4*. Primers were designed using Frodo (http://frodo.wi.mit.edu/primer3/) [137,138]. The products were visualized on a 1.6% agarose gel with SYBR GREEN staining (Invitrogen, Carlsbad, CA). Real-time PCR gene expression was characterized by quantitative PCR using the ABI 7500 system (Applied Biosystems, Carlsbad, CA). cDNA was amplified with the Fast Start SYBR Green master mix (Roche, Indianapolis, IN). Relative expression levels of target genes were analyzed by the delta-Ct method as published previously [139] using GAPDH or 18S as endogenous controls.

Western Blotting

Dissected tissues or cells were rinsed with PBS, trypsinized, spun down, and lysed in RIPA buffer and protease inhibitor cocktail. Supernatant was collected total protein concentrations were measured using the BCA protein assay kit (Thermo Scientific) (23225). Samples were mixed with 6X SDS and ran in a mini protean TGX 4-20% gel (Bio-Rad, CA) for 2 hrs at 120V at

25ºC in electrophoresis buffer. iBlot was used for gel transfer, using setting P3 at 7 minutes. The membranes were blocked using Odyssey Blocking buffer (LI-COR, NE) at 25ºC for 1 hr on a shaker and incubated with anti-beta-actin mouse monoclonal antibody at 1:2500 dilution or anti-WDR72 polyclonal antibody at 1:1000 dilution. Membranes were washed and incubated in Odyssey goat anti-rabbit IRDye 800 Green (926-32211) and goat anti-mouse IRDye 680Red (C21024-02) secondary antibodies (LI-COR, NE).

Transmission electron microscopy

Young-adult mice were anesthetized in tribromoethanol in 0.9% NaCl and perfused with fresh 3% PFA and 2.5% glutaraldehyde in 0.06M Cacodylate buffer (pH 7.3). Mandibles and maxillae were dissected and further immerse-fixed in the same fixatives at 4ºC overnight. Following rinse in 0.06M cacodylate buffer, the mandibles and maxillae were decalcified in 8% EDTA (pH 7.3) supplemented with 1% glutaraldehyde at 4ºC under constant agitation for two weeks.

Samples were then post-fixed with 1% osmium tetroxide in 0.06 M cacodylate buffer (pH 7.3) for 2h at 4°C and dehydrated through graded ethanols and embedded in LR white acrylic resin (London Resin Company, Reading, UK). One-micrometer-thick semi-thin sections were obtained for Toluidine Blue staining and light microscopic observation. An area where ameloblasts were immediately after the transition stage was chosen for ultrathin sectioning (80–100 nm). The ultrathin sections were placed on FormvarTM- and carbon-coated nickel grids, double stained with UAR-EMS Uranyl Acetate Replacement Stain (Electron Microscopy Sciences, Hatfield, PA) and 3% lead citrate, and examined under the FEI Tecnai G2 transmission electron microscope (Thermo Fisher Scientific Electron Microscopy, Hillsboro, OR) at an acceleration voltage of 80kV.

Cell culture protocols for ameloblast-like cells

ALCs of passage 22 were generously provided as a kind gift from Dr. Toshihiro Sugiyama, Akita University, Japan, and Dr. John Bartlett, The Ohio State University. Cells that had been stored in -80ºC in cell culture freezing medium (Gibco, 12648-010) were thawed at 37ºC and placed in new DMEM (DME H-16) supplemented with 1g/L glucose, 0.11g/L Na Pyruvate, 0.4g/L L-glutamine, and 3.7g/L $NaHCO_3$ (UCSF Cell Culture Facility CCFAA001-166L01) and 10% fetal bovine serum (FBS) (Gemini Gemcell, 100-500) and 1% penicillin and 1% streptomycin. Cells were then spun down at 1.2 rcf for 5 minutes and resuspended in fresh media to be plated in T-25 flasks (Thermo Fisher Scientific, MA). Media was changed daily or every other day for 1 week, after which they were approximately 60% confluent and were re-passaged and expanded to generate the cell culture line. Re-passaging included the following steps: removal of media, trypsinization for 3 minutes at 37ºC, resuspended in media, measurement of cell concentration to approximately 70,000 cells/mL using Trypsin Blue and cell counter, and replating onto new T-75 flasks (Thermo Fisher Scientific, MA).

Cells used for storage were grown to 80-90%. Once media was removed, cells were rinsed with PBS and trypsinized for 3 minutes at 37ºC. New media was recombined with 0.05% trypsin and placed into 15mL Falcon tubes to be spun down at 1.2 rcf for 5 minutes. After decanting trypsin/media mixture, cells were resuspended in 1 mL of freezing media (Gibco, 12648-010) for 3 minutes at 37ºC and placed in cryobox containing isopropanol at -80ºC.

Wdr72-deficient ameloblast-like cell generation using CRISPR/Cas9

Ameloblast-like cells were grown to 70% confluence to be transfected. Cells were then incubated at 37ºC for 72 hours with serum-free media, 2.5μM sgRNA transfection complex, 100ng/μL Edit-R EGFP fluorescent Cas9Nuclease mRNA (Dharmacon, CAS11860), and

transfection reagent. sgRNA transfection complexes (crRNA : tracrRNA in 10mM Tris Buffer, pH 7.4) were formed using either Edit-R crRNA Non-targeting Control #1 (U-007501-01-05) as a negative control, Edit-R-Ppib synthetic crRNA Control (U-007100-01-05) as a positive control targeting GTATACTTTGATTTACAAAT sequence, or Edit-R Mouse *Wdr72* (546144) crRNA (CM-068518-01-002) targeting AATATCCCAGAGGATCACAT at mm10|-chr9:74155036-74155058 AGG, Accession NM_001033500.3 (exon 12), combined with Edit-R CRISPR-Cas9 Synthetic tracrRNA (U-002005-20). crRNAs targeting *Wdr72* at exons 8 & 14 were also performed, however, analysis of those knockout cells were not analyzed in this dissertation.

Following treatment with CRISPR/Cas9, cells were grown to 80% confluence in DMEM supplemented with FBS and penicillin and streptomycin, as previously described (see above). Following rinsing, trypsinization, and re-suspension, cells were single-cell sorted at the PFCC flow cytometry core facility at Parnassus, UCSF (DRC Center Grant NIH P30 DK063720), using the Aria Fusion machine (NIH S10 1S10OD021822-01). Cells were gated for green fluorescence protein (GFP) and viability and subsequently plated as single-cells in 96-well plates. For the following two weeks, cells were monitored for single-colony growth in culture media and expanded for DNA sequencing verification. DNA was first purified using QIAquick PCR Purification Kit (Qiagen Sciences, Louisville, KY) (28104), and verification of cell knockout lines were performed using Sanger Sequencing.

Live cell imaging of amelogenin endocytosis

Control and knockout cell clones were grown to 70% confluence at equivalent cell densities on 35mm glass bottom dishes No. 0 (MatTek) (P35GC-0-14-C/H), then starved in serum-free media for 24 hours to facilitate endocytosis. Following starvation, 1µL of 1mg/mL rAMG 20kD labeled with Alexa Fluor 594 Microscale Protein Labeling Kit (Thermo Fisher Scientific, MA) (A30008) was added to media for 30 minutes. Synthesis and purification of recombinant

amelogenin 20kD purification (rAMG 20kD) was performed as previously published [140]. A solution of Hoescht DAPI stain (Invitrogen, H3570) and LysoTracker Green DND-26 (Life Technologies, CA, L7526) in 1X PBS/FBS were incubated with cells for 5 minutes. All cell groups were rinsed 3 times, and imaged under confocal microscopy for 45, 60, 90, and 135 minutes after rAMG 20kD was added.

Enamel matrix staining for modulation and pH changes

Adult mice were anesthetized with avertin in 0.9% NaCl, and maxillary and mandibular incisors were dissected on ice. Dissected incisors were either incubated in Universal pH indicator (Fisher Chemical, M21137) or in glyoxal-bis (2-hydroxyanil) (Santa Cruz Biotechnologies, CA) (SC-250064) in a solution of 3.4% NaOH in 75% ethanol. Once immersed in solution, the enamel organ was gently removed using a microbrush. All incisors were incubated for 3-5 minutes and rinsed in 100% ethanol until excess dye was removed, dried, and imaged.

Quantitative fluorescence-based vesicle acidification assay and imaging

Control and knockout cell clones were grown on either 96-well plates or 35mm glass bottom dishes No. 0 (MatTek) (P35GC-0-14-C/H) to undergo one of the following groups: no treatment (media only), 50 nM bafilomycin, or 50 nM bafilomycin plus a 3-hour washout. Cells in 96-well plates were used for quantification of fluorescence, while those in dishes were imaged under confocal microscopy for qualitative assessment.

Control and knockout cells used for quantification were incubated with either media only, 50 nM bafilomycin A1 (Sigma-Aldrich, MO) (SML1661) for 1 hour, or 50 nM bafilomycin A1 for 1 hour that was then washed out for 3 hours. All cell groups were labeled with a mixture of DAPI and LysoTracker for 10 minutes, then rinsed three times in PBS and lysed in 200 µL of RIPA lysis

buffer (50mM Tris-HCL, pH 7.4; 150mM NaCl, 1% NP-40, 0.5% sodium deoxycholate, 0.1% SDS). The lysate was then transferred into a black 96-well plate (Corning, Corning, NY), and fluorescence released into the medium was immediately read using a SpectraMax iD3 fluorescence plate reader (Molecular Devices) with 0.4-s integration time, at 500/565 nm for LysoTracker and 350/461 nm for DAPI. Total green fluorescence values (number of vesicles) were normalized to total blue values (cell number), and then to the untreated control (media only). Statistical significance was determined by one-way analysis of variance (ANOVA). *P*-values < 0.05 were considered significant.

Control and knockout cells used for confocal imaging were performed in quadruplicate biological replicates incubated under the same conditions as quantitative studies performed and imaged using an inverted confocal microscope (Leica Microsystems, DMi8) with Leica Application Suite X imaging software and processed using Fiji plug-ins and ImageJ [134–136].

Immunocytochemistry of alpha-tubulin and F-actin

Control and knockout cell clones were grown to 70% confluence and rinsed with microtubule stabilizing buffer (MSTB) with 0.5% glutaraldehyde for 30 minutes. Cells were then permeabilized with MSTB / 0.5% Triton X at 25ºC for 60 minutes, rinsed 3 times with PBS, and labeled with primary mouse anti-chick tubulin antibody (Thermo Fisher Scientific, MS-581, DM1A). M.O.M. biotinylated anti-mouse IgG / M.O.M. diluent was used as the secondary antibody for 10 minutes, followed by streptavidin 594 (DYlight, SA5594) at 1:100 dilution in the dark for 30 minutes. Phalloidin AF 488 green was used to label F-actin and was incubated with cells for 20 minutes in the dark. Cells were then counterstained with Hoescht DAPI stain (Invitrogen, H3570) at 1:10,000 dilution for 15 minutes and imaged under confocal microscopy.

REFERENCES

1. Nanci, A. *Ten Cate's Oral Histology: Development, Structure, and Function*. (2012).
2. Warshawsky, H. & Smith, C. E. Morphological classification of rat incisor ameloblasts. *Anat. Rec.* **179**, 423–446 (1974).
3. Bartlett, J. D. Dental Enamel Development: Proteinases and Their Enamel Matrix Substrates. *ISRN Dent.* **2013**, 684607 (2013).
4. Smith, C. E., Pompura, J. R., Borenstein, S., Fazel, A. & Nanci, A. Degradation and loss of matrix proteins from developing enamel. *Anat. Rec.* **224**, 292–316 (1989).
5. E J Reith, A. B. The arrangement of ameloblasts on the surface of maturing enamel of the rat incisor tooth. *J. Anat.* **133**, 381 (1981).
6. Lu, T. *et al.* Whole exome sequencing identifies an AMBN missense mutation causing severe autosomal-dominant amelogenesis imperfecta and dentin disorders. *Int. J. Oral Sci.* **10**, 26 (2018).
7. Poulter, J. A. *et al.* Deletion of ameloblastin exon 6 is associated with amelogenesis imperfecta. *Hum. Mol. Genet.* **23**, 5317–5324 (2014).
8. Hu, J. C. C., Chun, Y.-H. P., Al Hazzazzi, T. & Simmer, J. P. Enamel formation and amelogenesis imperfecta. *Cells. Tissues. Organs* **186**, 78–85 (2007).
9. Wright, J. T. *et al.* Amelogenesis Imperfecta: Genotype-Phenotype Studies in 71 Families. *Cells Tissues Organs* **194**, 279–283 (2011).
10. Parry, D. A. *et al.* Identification of mutations in SLC24A4, encoding a potassium-dependent sodium/calcium exchanger, as a cause of amelogenesis imperfecta. *Am. J. Hum. Genet.* **92**, 307–312 (2013).
11. Ding, Y. *et al.* Fam83h is associated with intracellular vesicles and ADHCAI. *J. Dent. Res.* **88**, 991–996 (2009).
12. Wright, J. T. *et al.* Phenotypic variation in FAM83H-associated amelogenesis imperfecta. *J. Dent. Res.* **88**, 356–360 (2009).

13. Wang, S.-K. *et al.* ITGB6 loss-of-function mutations cause autosomal recessive amelogenesis imperfecta. *Hum. Mol. Genet.* (2013). doi:10.1093/hmg/ddt611

14. Mohazab, L. *et al.* Critical role for αvβ6 integrin in enamel biomineralization. *J. Cell Sci.* **126**, 732–44 (2013).

15. Poulter, J. A. *et al.* A missense mutation in ITGB6 causes pitted hypomineralized amelogenesis imperfecta. *Hum. Mol. Genet.* **23**, 2189–2197 (2014).

16. Lee, K.-E. *et al.* Novel LAMB3 mutations cause non-syndromic amelogenesis imperfecta with variable expressivity. *Clin. Genet.* (2014). doi:10.1111/cge.12340

17. Kim, J.-W. *et al.* LAMB3 mutations causing autosomal-dominant amelogenesis imperfecta. *J. Dent. Res.* **92**, 899–904 (2013).

18. Poulter, J. A. *et al.* Whole-exome sequencing, without prior linkage, identifies a mutation in LAMB3 as a cause of dominant hypoplastic amelogenesis imperfecta. *Eur. J. Hum. Genet.* **22**, 132–135 (2014).

19. Kantaputra, P. N. *et al.* Enamel-renal-gingival syndrome and FAM20A mutations. *Am. J. Med. Genet. A* **164**, 1–9 (2014).

20. Wang, S.-K. *et al.* FAM20A Mutations Associated with Enamel Renal Syndrome. *J. Dent. Res.* **93**, 42–48 (2014).

21. Parry, D. A. *et al.* Mutations in C4orf26, encoding a peptide with in vitro hydroxyapatite crystal nucleation and growth activity, cause amelogenesis imperfecta. *Am. J. Hum. Genet.* **91**, 565–571 (2012).

22. El-Sayed, W. *et al.* Mutations in the beta propeller WDR72 cause autosomal-recessive hypomaturation amelogenesis imperfecta. *Am. J. Hum. Genet.* **85**, 699–705 (2009).

23. Lee, S.-K. *et al.* Novel WDR72 mutation and cytoplasmic localization. *J. Dent. Res.* **89**, 1378–1382 (2010).

24. Parry, D. A. *et al.* Mutations in the pH-Sensing G-protein-Coupled Receptor GPR68 Cause Amelogenesis Imperfecta. *Am. J. Hum. Genet.* (2016).

doi:10.1016/j.ajhg.2016.08.020

25. Kantaputra, P. N., Matangkasombut, O. & Sripathomsawat, W. Split hand-split foot-ectodermal dysplasia and amelogenesis imperfecta with a TP63 mutation. *Am. J. Med. Genet. A* **158A**, 188–192 (2012).

26. Schossig, A. *et al.* SLC13A5 is the second gene associated with Kohlschütter-Tönz syndrome. *J. Med. Genet.* jmedgenet-2016-103988 (2016). doi:10.1136/jmedgenet-2016-103988

27. Yuen, W. Y., Pasmooij, A. M. G., Stellingsma, C. & Jonkman, M. F. Enamel defects in carriers of a novel LAMA3 mutation underlying epidermolysis bullosa. *Acta Derm. Venereol.* **92**, 695–696 (2012).

28. Kuechler, A. *et al.* A Novel Homozygous WDR72 Mutation in Two Siblings with Amelogenesis Imperfecta and Mild Short Stature. *Mol. Syndromol.* **3**, 223–229 (2012).

29. Rungroj, N. *et al.* Distal renal tubular acidosis caused by tryptophan-aspartate repeat domain 72 (WDR72) mutations. *Clin. Genet.* **94**, 409–418 (2018).

30. Wright, J. T., Carrion, I. A. & Morris, C. The molecular basis of hereditary enamel defects in humans. *J. Dent. Res.* **94**, 52–61 (2015).

31. Thierry-Mieg, D. & Thierry-Mieg, J. (No Title). *Genome Biol.* **7**, S12 (2006).

32. El-Sayed, W., Shore, R. C., Parry, D. A., Inglehearn, C. F. & Mighell, A. J. Hypomaturation amelogenesis imperfecta due to WDR72 mutations: a novel mutation and ultrastructural analyses of deciduous teeth. *Cells. Tissues. Organs* **194**, 60–66 (2011).

33. Vasan, R. S. *et al.* Genome-wide association of echocardiographic dimensions, brachial artery endothelial function and treadmill exercise responses in the Framingham Heart Study. *BMC Med. Genet.* **8 Suppl 1**, S2--S2 (2007).

34. Köttgen, A. Genome-wide association studies in nephrology research. *Am. J. Kidney Dis.* **56**, 743–758 (2010).

35. Paterson, A. D. *et al.* A genome-wide association study identifies a novel major locus for glycemic control in type 1 diabetes, as measured by both A1C and glucose. *Diabetes* **59**, 539–549 (2010).

36. Hertel, J. K. *et al.* Evaluation of four novel genetic variants affecting hemoglobin A1c levels in a population-based type 2 diabetes cohort (the HUNT2 study). *BMC Med. Genet.* **12**, 20 (2011).

37. Leblanc, M. *et al.* Genome-wide study identifiesPTPROandWDR72andFOXQ1-SUMO1P1interaction associated with neurocognitive function. *J. Psychiatr. Res.* **46**, 271–278 (2012).

38. Franceschini, N. *et al.* Generalization of associations of kidney-related genetic loci to American Indians. *Clin. J. Am. Soc. Nephrol.* **9**, 150–158 (2014).

39. Katsura, K. A. *et al.* WDR72 models of structure and function: A stage-specific regulator of enamel mineralization. *Matrix Biol.* **38**, 48–58 (2014).

40. Hentschel, J. *et al.* Identification of the first multi-exonic WDR72 deletion in isolated amelogenesis imperfecta, and generation of a WDR72-specific copy number screening tool. *Gene* **590**, 1–4 (2016).

41. Skarnes, W. C. *et al.* A conditional knockout resource for the genome-wide study of mouse gene function. *Nature* **474**, 337–344 (2011).

42. Galy, B., Ferring, D., Benesova, M., Benes, V. & Hentze, M. W. Targeted mutagenesis of the murine IRP1 and IRP2 genes reveals context-dependent RNA processing differences in vivo. *RNA* **10**, 1019–1025 (2004).

43. Zhang, Y. Template-based modeling and free modeling by I-TASSER in CASP7. *Proteins* **69 Suppl 8**, 108–117 (2007).

44. Roy, A., Kucukural, A. & Zhang, Y. I-TASSER: a unified platform for automated protein structure and function prediction. *Nat. Protoc.* **5**, 725–738 (2010).

45. Söding, J., Biegert, A. & Lupas, A. N. The HHpred interactive server for protein homology

detection and structure prediction. *Nucleic Acids Res.* **33**, W244--8 (2005).

46. Lee, C. & Goldberg, J. Structure of Coatomer Cage Proteins and the Relationship among COPI, COPII, and Clathrin Vesicle Coats. *Cell* **142**, 123–132 (2010).

47. Field, M. C., Sali, A. & Rout, M. P. Evolution: On a bender--BARs, ESCRTs, COPs, and finally getting your coat. *J. Cell Biol.* **193**, 963–972 (2011).

48. Menke, M., Berger, B. & Cowen, L. Markov random fields reveal an N-terminal double beta-propeller motif as part of a bacterial hybrid two-component sensor system. *Proc. Natl. Acad. Sci. U. S. A.* **107**, 4069–4074 (2010).

49. Leblond, C. P. & Warshawsky, H. *Chapter VIII Dynamics of Enamel Formation in the Rat Incisor Tooth*. (1979).

50. Hart, P. S. *et al.* Mutation in kallikrein 4 causes autosomal recessive hypomaturation amelogenesis imperfecta. *J. Med. Genet.* **41**, 545–549 (2004).

51. Kim, J.-W. *et al.* MMP-20 mutation in autosomal recessive pigmented hypomaturation amelogenesis imperfecta. *J. Med. Genet.* **42**, 271–275 (2005).

52. Barron, M. J. *et al.* A mutation in the mouse Amelx tri-tyrosyl domain results in impaired secretion of amelogenin and phenocopies human X-linked amelogenesis imperfecta. *Hum. Mol. Genet.* **19**, 1230–1247 (2010).

53. Smith, C. E. Ameloblasts: secretory and resorptive functions. *J. Dent. Res.* **58**, 695–707 (1979).

54. Gibson, C. W. The Amelogenin Proteins and Enamel Development in Humans and Mice. *J Oral Biosci.* **53**, 248–256 (2011).

55. Nanci, A. *et al.* Comparative Immunochemical Analyses of the Developmental Expression and Distribution of Ameloblastin and Amelogenin in Rat Incisors. *J. Histochem. Cytochem.* **46**, 911–934 (1998).

56. Hubbard, M. J. Calcium transport across the dental enamel epithelium. *Crit. Rev. Oral Biol. {&} Med.* **11**, 437–466 (2000).

57. Sasaki, T. Tracer, cytochemical, and freeze-fracture study on the mechanisms whereby secretory ameloblasts absorb exogeneous proteins. *Cells. Tissues. Organs* **118**, 23–33 (1984).

58. Nanci, a., Fortin, M. & Ghitescu, L. Endocytotic functions of ameloblasts and odontoblasts: immunocytochemical and tracer studies on the uptake of plasma proteins. *Anat. Rec.* **245**, 219–234 (1996).

59. Lacruz, R. S. *et al.* Adaptor protein complex 2-mediated, clathrin-dependent endocytosis, and related gene activities, are a prominent feature during maturation stage amelogenesis. *J. Bone Miner. Res.* **28**, 672–687 (2013).

60. Devuyst, O. Intra-renal and subcellular distribution of the human chloride channel, CLC-5, reveals a pathophysiological basis for Dent's disease. *Hum. Mol. Genet.* **8**, 247–257 (1999).

61. Lin, Z. *et al.* Chloride channel (Clc)-5 is necessary for exocytic trafficking of Na+/H+ exchanger 3 (NHE3). *J. Biol. Chem.* **286**, 22833–22845 (2011).

62. Luyckx, V. A. *et al.* Intrarenal and subcellular localization of rat CLC5. *Am. J. Physiol. - Ren. Physiol.* **275**, (1998).

63. Hara-Chikuma, M., Wang, Y., Guggino, S. E., Guggino, W. B. & Verkman, A. S. Impaired acidification in early endosomes of ClC-5 deficient proximal tubule. *Biochem. Biophys. Res. Commun.* **329**, 941–946 (2005).

64. Duan, X. Ion channels, channelopathies, and tooth formation. *J. Dent. Res.* **93**, 117–125 (2014).

65. Le, T. Q., Zhang, Y., Li, W. & DenBesten, P. K. The effect of LRAP on enamel organ epithelial cell differentiation. *J. Dent. Res.* **86**, 1095–1099 (2007).

66. Shapiro, J. L. *et al.* Cellular uptake of amelogenin, and its localization to CD63, and Lamp1-positive vesicles. *Cell. Mol. Life Sci.* **64**, 244–256 (2007).

67. Devos, D. *et al.* Components of Coated Vesicles and Nuclear Pore Complexes Share a

Common Molecular Architecture. *PLOS Biol.* **2**, e380 (2004).

68. Stirnimann, C. U., Petsalaki, E., Russell, R. B. & Müller, C. W. WD40 proteins propel cellular networks. *Trends Biochem. Sci.* **35**, 565–574 (2010).

69. Good, M. C., Zalatan, J. G. & Lim, W. a. Scaffold proteins: hubs for controlling the flow of cellular information. *Science* **332**, 680–686 (2011).

70. Xu, C. & Min, J. Structure and function of WD40 domain proteins. *Protein {&} cell* **2**, 202–214 (2011).

71. Nagano, F. F. *et al.* Rabconnectin-3, a novel protein that binds both GDP/GTP exchange protein and GTPase-activating protein for Rab3 small G protein family. *J. Biol. Chem.* **277**, 9629–9632 (2002).

72. Kawabe, H. *et al.* A novel rabconnectin-3-binding protein that directly binds a GDP/GTP exchange protein for Rab3A small G protein implicated in Ca(2+)-dependent exocytosis of neurotransmitter. *Genes to Cells* **8**, 537–546 (2003).

73. Yan, Y., Denef, N., Schüpbach, T. & Schupbach, T. The Vacuolar Proton Pump, V-ATPase, Is Required for Notch Signaling and Endosomal Trafficking inDrosophila. *Dev. Cell* **17**, 387–402 (2009).

74. Sethi, N., Yan, Y., Quek, D., Schupbach, T. & Kang, Y. Rabconnectin-3 is a functional regulator of mammalian Notch signaling. *J. Biol. Chem.* **285**, 34757–34764 (2010).

75. Smith, C. E. *et al.* Effect of kallikrein 4 loss on enamel mineralization: comparison with mice lacking matrix metalloproteinase 20. *J. Biol. Chem.* **286**, 18149–60 (2011).

76. Hu, Y., Hu, J. C. C., Smith, C. E., Bartlett, J. D. & Simmer, J. P. Kallikrein-related peptidase 4, matrix metalloproteinase 20, and the maturation of murine and porcine enamel. *Eur. J. Oral Sci.* **119 Suppl**, 217–225 (2011).

77. Simmer, J. P., Hu, Y., Lertlam, R., Yamakoshi, Y. & Hu, J. C. C. Hypomaturation enamel defects in Klk4 knockout/LacZ knockin mice. *J. Biol. Chem.* **284**, 19110–19121 (2009).

78. Zhu, L. *et al.* Preferential and selective degradation and removal of amelogenin adsorbed

on hydroxyapatites by MMP20 and KLK4 in vitro. *Front. Physiol.* **5**, 268 (2014).

79. Kallenbach, E. Fine structure of rat incisor ameloblasts during enamel maturation. *J. Ultrastruct. Res.* **22**, 90–119 (1968).

80. Sasaki, T., Tadokoro, K., Yanagisawa, T., Higashi, S. & Garant, P. R. H+-K+-ATPase activity in the rat incisor enamel organ during enamel formation. *Anat. Rec.* **221**, 823–833 (1988).

81. Salama, A. H. A. H., Zaki, A. E. A. E. & Eisenmann, D. R. D. R. Fine structural changes and lysosomal phosphatase cytochemistry of ameloblasts associated with the transitional stage of enamel formation in the rat incisor. *Dev. Dyn.* **190**, 279–290 (1991).

82. Sasaki, T. T. Endocytotic pathways at the ruffled borders of rat maturation ameloblasts. *Histochemie.* **80**, 263–268 (1984).

83. Takano, Y. & Ozawa, H. Ultrastructural and cytochemical observations on the alternating morphologic changes of the ameloblasts at the stage of enamel maturation. *Arch. Histol. Jpn.* **43**, 385–399 (1980).

84. Bonifacino, J. S. & Glick, B. S. The Mechanisms of Vesicle Budding and Fusion. *Cell* **116**, 153–166 (2004).

85. Zhang, Y. *et al.* SATB1 establishes ameloblast cell polarity and regulates directional amelogenin secretion for enamel formation. 1–16 (2019).

86. Goebeler, V., Poeter, M., Zeuschner, D., Gerke, V. & Rescher, U. Annexin A8 Regulates Late Endosome Organization and Function. *Mol. Biol. Cell* **19**, 5267–5278 (2008).

87. Goebeler, V., Ruhe, D., Gerke, V. & Rescher, U. Annexin A8 displays unique phospholipid and F-actin binding properties. *FEBS Lett.* **580**, 2430–2434 (2006).

88. Grewal, T. & Enrich, C. Annexins — Modulators of EGF receptor signalling and trafficking. **21**, 847–858 (2009).

89. Huotari, J. & Helenius, A. Endosome maturation. *EMBO J.* **30**, 3481–3500 (2011).

90. Samann, A. C., Wang, S.-K., Hu, J. C. C. & Simmer, J. P. Interactome Analysis of

WDR72 Reveals its Potential Function on Endocytosis. in *IADR* 1 (2013).

91. Loerke, D. *et al.* Cargo and Dynamin Regulate Clathrin-Coated Pit Maturation. **7**, (2009).
92. Robinson, S. The role of clathrin, adaptors and dynamin in endocytosis. *Curr. Opin. Cell Biol.* **6**, 538–544 (1994).
93. Shupliakov, O. *et al.* Synaptic Vesicle Endocytosis Impaired by Disruption of Dynamin – SH3 Domain Interactions. **276**, 259–264 (1997).
94. Zhang, C. *et al.* Endocytosis in Dorsal Root Ganglion Neurons. **42**, 225–236 (2004).
95. Rink, J., Ghigo, E., Kalaidzidis, Y. & Zerial, M. Rab conversion as a mechanism of progression from early to late endosomes. *Cell* **122**, 735–749 (2005).
96. Poteryaev, D., Datta, S., Ackema, K., Zerial, M. & Spang, A. Identification of the switch in early-to-late endosome transition. *Cell* **141**, 497–508 (2010).
97. Maxfield, F. R. & Yamashiro, D. J. Endosome acidification and the pathways of receptor-mediated endocytosis. *Advances in experimental medicine and biology* **225**, 189–198 (1987).
98. Huynh, K. K. & Grinstein, S. Regulation of Vacuolar pH and Its Modulation by Some Microbial Species. *Microbiol. Mol. Biol. Rev.* **71**, 452–462 (2007).
99. Jentsch, T. J. T. J. Chloride and the endosomal-lysosomal pathway: emerging roles of CLC chloride transporters. in *Journal of Physiology* 633–640 (2007). doi:10.1113/jphysiol.2006.124719
100. Marshansky, V. & Futai, M. The V-type H+-ATPase in vesicular trafficking: targeting, regulation and function. *Curr. Opin. Cell Biol.* **20**, 415–426 (2008).
101. Vaccari, T., Duchi, S., Cortese, K., Tacchetti, C. & Bilder, D. The vacuolar ATPase is required for physiological as well as pathological activation of the Notch receptor. *Development* **137**, 1825–1832 (2010).
102. Hunziker, W., Whitney, J. A. & Mellman, I. Brefeldin A and the endocytic pathway Possible implications for membrane traffic and sorting. *FEBS Lett.* **307**, 93–96 (1992).

103. Luzio, J. P., Pryor, P. R. & Bright, N. A. Lysosomes: fusion and function. *Nat. Rev. Mol. Cell Biol.* **8**, 622–632 (2007).

104. Gurkan, C. *et al.* Large-scale profiling of Rab GTPase trafficking networks: the membrome. *Mol. Biol. Cell* **16**, 3847–3864 (2005).

105. Nakata, A. *et al.* Establishment and characterization of a spontaneously immortalized mouse ameloblast-lineage cell line. *Biochem. Biophys. Res. Commun.* **308**, 834–839 (2003).

106. Sarkar, J. *et al.* Comparison of two mouse ameloblast-like cell lines for enamel-specific gene expression. *Front. Physiol.* **5**, 1–6 (2014).

107. Wang, S.-K. *et al.* Critical roles for WDR72 in calcium transport and matrix protein removal during enamel maturation. *Mol. Genet. Genomic Med.* **3**, 302–319 (2015).

108. Bampton, E. T. W., Goemans, C. G., Niranjan, D., Mizushima, N. & Tolkovsky, A. M. The dynamics of autophagy visualized in live cells: from autophagosome formation to fusion with endo/lysosomes. *Autophagy* **1**, 23–36 (2005).

109. Razi, M. & Futter, C. E. Distinct roles for Tsg101 and Hrs in multivesicular body formation and inward vesiculation. *Mol. Biol. Cell* **17**, 3469–3483 (2006).

110. Steinman, R. M., Mellman, I. S., Muller, W. A. & Cohn, Z. A. Endocytosis and the recycling of plasma membrane. *J. Cell Biol.* **96**, 1–27 (1983).

111. Platt, F. M., Boland, B. & van der Spoel, A. C. Lysosomal storage disorders: The cellular impact of lysosomal dysfunction. *J. Cell Biol.* **199**, 723–734 (2012).

112. Damkier, H. H. *et al.* Fluctuations in surface pH of maturing rat incisor enamel are a result of cycles of H(+)-secretion by ameloblasts and variations in enamel buffer characteristics. *Bone* **60**, 227–234 (2014).

113. Takano, Y. *et al.* A histochemical demonstration of calcium in the maturation stage enamel organ of rat incisors. *Arch. Histol. Cytol.* **51**, 241–248 (1988).

114. Bronckers, A. L. J. J., Lyaruu, D. M., Jalali, R. & DenBesten, P. K. Buffering of protons

released by mineral formation during amelogenesis in mice. *Eur. J. Oral Sci.* **124**, 415–425 (2016).

115. Jalali, R. *et al.* NBCe1 (SLC4A4) a potential pH regulator in enamel organ cells during enamel development in the mouse. *Cell Tissue Res.* (2014). doi:10.1007/s00441-014-1935-4

116. Smith, C. E. C. E. Cellular and chemical events during enamel maturation. *Crit. Rev. Oral Biol. {&} Med.* **9**, 128–161 (1998).

117. Josephsen, K. *et al.* Ion transporters in secretory and cyclically modulating ameloblasts: a new hypothesis for cellular control of preeruptive enamel maturation. *Am. J. Physiol. Cell Physiol.* **299**, C1299--307 (2010).

118. Johnson, L. *et al.* V-ATPases Containing *a* 3 Subunit Play a Direct Role in Enamel Development in Mice. *J. Cell. Biochem.* (2017). doi:10.1002/jcb.25986

119. Merkulova, M. *et al.* Mapping the H^+ (V)-ATPase interactome: Identification of proteins involved in trafficking, folding, assembly and phosphorylation. *Sci. Rep.* **5**, 1–15 (2015).

120. Bayer, N. *et al. Effect of Bafilomycin A1 and Nocodazole on Endocytic Transport in HeLa Cells: Implications for Viral Uncoating and Infection*. *JOURNAL OF VIROLOGY* **72**, (1998).

121. Schoumacher, M., Goldman, R. D., Louvard, D. & Vignjevic, D. M. Actin, microtubules, and vimentin intermediate filaments cooperate for elongation of invadopodia. *J. Cell Biol.* **189**, 541–556 (2010).

122. Gruenberg, J. & Stenmark, H. The biogenesis of multivesicular endosomes. *Nat. Rev. Mol. Cell Biol.* **5**, 317–323 (2004).

123. Gruenberg, J., Griffiths, G. & Howell, K. E. Characterization of the early endosome and putative endocytic carrier vesicles in vivo and with an assay of vesicle fusion in vitro. *J. Cell Biol.* **108**, 1301–1316 (1989).

124. Kannan, M. *et al.* WD40-repeat 47, a microtubule-associated protein, is essential for brain

development and autophagy. *Proc. Natl. Acad. Sci.* **114**, E9308–E9317 (2017).

125. Chen, J.-F. *et al.* Microcephaly disease gene Wdr62 regulates mitotic progression of embryonic neural stem cells and brain size. (2014). doi:10.1038/ncomms4885

126. Akita, H. & Kagayama, M. Ultrastructure of mouse incisor ameloblasts after vascular perfusion with colchicine. *Cell Tissue Res.* **239**, 567–574 (1985).

127. Schwarz, D. S. & Blower, M. D. The endoplasmic reticulum: Structure, function and response to cellular signaling. *Cell. Mol. Life Sci.* **73**, 79–94 (2016).

128. Collinet, C. *et al.* Systems survey of endocytosis by multiparametric image analysis. *Nature* **464**, 243–249 (2010).

129. Sali, A. & Blundell, T. L. Comparative protein modelling by satisfaction of spatial restraints. *J. Mol. Biol.* **234**, 779–815 (1993).

130. Zemla, A., Venclovas, Moult, J. & Fidelis, K. Processing and evaluation of predictions in CASP4. *Proteins* **Suppl 5**, 13–21 (2001).

131. Mariani, V., Kiefer, F., Schmidt, T., Haas, J. & Schwede, T. Assessment of template based protein structure predictions in CASP9. *Proteins* **79 Suppl 1**, 37–58 (2011).

132. Yang, Z. *et al.* UCSF Chimera, MODELLER, and IMP: an integrated modeling system. *J. Struct. Biol.* **179**, 269–278 (2012).

133. Li, W., Mathews, C., Gao, C. & DenBesten, P. K. Identification of two additional exons at the 3’ end of the amelogenin gene. *Arch. Oral Biol.* **43**, 497–504 (1998).

134. Abràmoff, M. D., Magalhães, P. J. & Ram, S. J. Image processing with imageJ. *Biophotonics Int.* **11**, 36–41 (2004).

135. Rasband, W. S. ImageJ. *U.S. National Institutes of Health, Bethesda, Maryland, USA* Available at: https://imagej.nih.gov/ij/.

136. Schneider, C. A., Rasband, W. S. & Eliceiri, K. W. NIH Image to ImageJ: 25 years of image analysis. *Nature Methods* **9**, 671–675 (2012).

137. Koressaar, T. & Remm, M. Enhancements and modifications of primer design program

Primer3. *Bioinformatics* **23**, 1289–1291 (2007).

138. Untergasser, A. *et al.* Primer3--new capabilities and interfaces. *Nucleic Acids Res.* **40**, e115--e115 (2012).

139. Thomsen, R. R., Sølvsten, C. A. E. C. A., Linnet, T. E. T. E., Blechingberg, J. J. & Nielsen, A. L. A. L. Analysis of qPCR data by converting exponentially related Ct values into linearly related X0 values. *J. Bioinform. Comput. Biol.* **8**, 885–900 (2010).

140. Svensson Bonde, J. & Bulow, L. One-step purification of recombinant human amelogenin and use of amelogenin as a fusion partner. *PLoS One* **7**, (2012).

LIBRARY RELEASE PAGE

Publishing Agreement

It is the policy of the University to encourage the distribution of all theses, dissertations, and manuscripts. Copies of all UCSF theses, dissertations, and manuscripts will be routed to the library via the Graduate Division. The library will make all theses, dissertations, and manuscripts accessible to the public and will preserve these to the best of their abilities, in perpetuity.

Please sign the following statement:

I hereby grant permission to the Graduate Division of the University of California, San Francisco to release copies of my thesis, dissertation, or manuscript to the Campus Library to provide access and preservation, in whole or in part, in perpetuity.

DocuSigned by:
Katilin Katsura
76E4CC1E78714AB...

Author Signature

12/8/2019

Date